UNIVERSITÀ DEGLI STUDI DI CATANIA
DIPARTIMENTO DI FISICA E ASTRONOMIA
XXXII Ciclo di Dottorato in Fisica

Leonard Giuseppe Re

CHARACTERIZATION OF THE GEM CHAMBERS FOR THE SBS/BB FRONT TRACKER AT JLAB HALL A

PhD THESIS

Supervisor:
Prof. V. Bellini

Scientific Tutor:
Dott. E. Cisbani

Accademic Year 2018/2019

Contents

Introduction

The nucleon electromagnetic Form Factors (FFs) are quantities of great theoretical and experimental importance. The ground-state electromagnetic FFs are among the most fundamental quantities that describe the non-perturbative structure of the nucleons. Their study provides a great medium for the understanding of non-perturbative quantum chromodynamics (QCD) and confinement. The issue of their determination has been revisited within the last 15 years, thanks to the results of several experiments carried on mainly at the most important research laboratories in the world, and especially, in the Thomas Jefferson National Accelerator Facility (called also JLab) [1], which questioned previous results founded on Rosenbluth method and urged the necessity for a new detailed studies of the form factors themselves [2]. In fact, one of the most striking results to come out from JLab on FFs (between 1999 and 2002), by "new" polarization transfer technique, is the discovery that the ratio of the electric and magnetic form factors of the proton, G_E^p/G_M^p, decreases almost linearly for Q^2 values above approximately 1 GeV^2. The previously disseminated expectation with the Rosenbluth technique was that this ratio would be roughly constant and about equal to one [3]. The proton form factors determined from the measurements of polarization transfer in ep scattering were in relevant disagreement with those obtained from scattering data via the classical Rosenbluth separation method. This result has stimulated enormous interest [4].

Many theories and models have tried to explain this result but the main suggestion for solving this inconsistency was to account for Two-Photon Exchange (TPE), which should affect the cross-section to a greater extent than the polarization data. In this approach, the TPE contributions have been estimated at the partonic level in terms of generalized parton distributions: the Rosenbluth cross sections results smaller, bringing the FFs derived from them, closer to the polarization results [5]. Therefore, the best way to expanding the understanding of the underlying quark structure of the nucleon is to make measurements in a regime where the best theoretical predictions strongly diverge from one another, and where simplifications occur that aid in the interpretation of the data [6].

Doing this will require measurements at significantly higher values of Q^2 (where the cross sections are very small), and as much as possible, obtaining measurements on nucleons with high precision. For these reasons, an experimental program at large luminosity that incorporates five related measurements of the ground-state nucleon electromagnetic form factors have been proposed and successfully approved at JLab. Each of the measurements will use the electron beam from the recently upgraded 12-GeV CEBAF (Continuous Electron Beam Accelerator Facility) accelerator [1].

The five planned measurements ([7], [8], [9], [10], and [11]) require similar but properly arranged experimental components. A common effort, the "*Super Bigbite Project"*, has been carried on to develop the the optimal experimental equipment to push forward a new level of precision for all the above experiments [3].

The Super Bigbite Project adopt consolidated concept but with state-of-the-art technologies. A very important component is a large-acceptance spectrometer using an open-geometry spectrometer based on a single dipole magnet. To push this approach further, however, it is necessary to have tracking systems capable of handling significantly and challenging particles rates due to the required large luminosity. Therefore, in the Super Bigbite Project, a set of GEM (Gas Electron Multiplier) detectors with the remarkable rate-handling capability, a dipole magnet with a wide cutout-path for the electron beam (for the detection at forward angles), a double polarimeter analyzer for analyzing the polarization of the nucleon scattered and a segmented hadron calorimeter to provide a trigger system are integrated together to form the "*Super Bigbite Spectrometer*" (*SBS*) [12].

These measurements will challenge the existing theory of non-perturbative structure at unprecedented levels, and will cleanly discriminate between some of the best current predictions. The proposed experiments that utilizing the SBS will provide many important answers about the nuclear structure by incorporating innovative and state of the art technology. The development of GEM technology, together with other components, make the SBS the future for the study of form factors.

The development and set-up of the Super Bigbite Spectrometer is carried out by a collaboration involving seven Universities in the USA, the University of Glasgow and the various Italian INFN [1] groups, including Catania, Genoa, Bari and Rome. The JLab12 Italian collaboration took charge of the construction of the SBS GEM front tracker.

The present document discusses the main aspects and results of the ongoing SBS-GEM development, production and test, according to the following structure:

- In chapter 1 the theoretical and experimental importance of nucleon electromagnetic form factors is described. Furthermore, the discrepancy of *ep* scattering data obtained about the FFs ratio between the Rosenbluth separation method and the polarization transfer method is highlighted and, therefore, the Super Bigbite Program at JLab is introduced.

- In chapter 2 the experimental apparatus of the SBS project is described, focusing on the main components of the spectrometers involved; the Super Bigbite Spectrometer for the hadron arm and the BigBite spectrometer for the electron arm.

- Chapter 3 describes the SBS/BB front tracker and the motivation on the GEM technology choice. In addition, the main features and advantages of the technology used are also described.

[1] Istituto Nazionale di Fisica Nucleare

- Chapter 4 describes the commissioning of the GEM trackers at JLab. The whole iter of the GEM modules is presented, from the assembly in clean-room to the characterization tests with cosmic rays performed at JLab.
- In chapter 5 a new method of analyzing the signals extracted from the strips of GEM modules is introduced. This study goal is the real-time suppression of noisy data by mean of innovative A.I. techniques.

Chapter 1

The physics case of the nucleon form factors

The nucleon electromagnetic Form Factors (FFs) describe the spatial distributions of electric charge and current inside the nucleon and thus they contain information concerning its internal structure; the FFs have long provided information about the composition of most basic elements of nuclear physics, and therefore they are a measurable and physical manifestation of the nature of the nucleons' constituents and the dynamics that binds them together [2]. The ground-state electromagnetic nucleon form factors are among the most fundamental quantities that describe the non-perturbative structure of the proton and neutron, therefore, their study, by electron scattering experiments, provides a powerful test of understanding of non-perturbative QCD and confinement [3]. They also contain important information on nucleon radii and vector meson coupling constants and they are an important ingredient in a wide range of experiments such as Lamb shift measurements [13] and measurements of the strangeness content of the nucleon [14].

1.1 The Nucleon Electromagnetic Form Factors

The nucleon electromagnetic form factors are fundamental quantities regarding the charge and magnetization distributions within the protons and neutrons. Understanding the nucleon electromagnetic structure, in the context of Quantum Chromodynamics, is a very hard and demanding task. A brief discussion about the nucleon form factors is given below.

From quantum electrodynamics, the lowest-order amplitude for electron-nucleon elastic scattering, as shown in Figure 1.1, is given by

$$T_{fi} = \int -ij_{\mu}\left(\frac{-1}{q^2}\right)J^{\mu}d^4x, \tag{1.1}$$

where $q = p' - p$ and the electron transition current is

$$j^{\mu} = -e\bar{u}\left(k^{'}\right)\gamma^{\mu}u\left(k\right)e^{i(k'-k)x}. \tag{1.2}$$

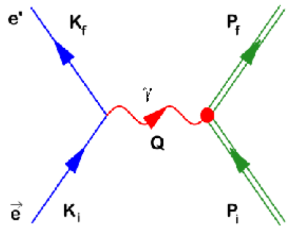

Figure 1.1: The one-photon-exchange for electron-nucleon elastic scattering.

The nucleon is an extended half-integer spin object, thus the nucleon transition current is more complicated than that of the electron [15]. According to the requirements of covariance under the Lorentz transformations, current conservation, and parity conservation, the nucleon transition current is written as

$$J^{\mu} = e\bar{N}\left(p^{'}\right)\left[F_1(Q^2)\gamma^{\mu} + \frac{i\sigma^{\mu\nu}q_{\nu}}{2M}F_2(Q^2)\right]N(p), \tag{1.3}$$

where $Q^2 = -q^2$, is the negative of the square of the invariant mass of the virtual photon in the one-photon exchange approximation in ep scattering, γ^{μ} are Dirac matrices, F_1 and F_2 are two independent form factors, also called the Dirac and Pauli form factors, respectively, M is the nucleon mass, and N is the nucleon spinor [4]. The so-called Sachs form factors derive from a linear combination of FFs of Dirac and Pauli, and they are:

$$G_E^{p,n}\left(q^2\right) = F_1^{p,n}(q^2) - \frac{q^2}{4M^2}\,kF_2^{p,n}(q^2) \tag{1.4}$$

$$G_M^{p,n}\left(q^2\right) = F_1^{p,n}(q^2) + \,kF_2^{p,n}(q^2), \tag{1.5}$$

where k is the Bohr magneton. It follows that in the static limit, $Q^2 = 0$, $G_E^p(0) = 1$, $G_E^n(0) = 0$, $G_M^p(0) = 2.79$, and $G_M^n(0) = -1.91$. They correspond to the charge and the magnetic moment of the nucleon. Sachs demonstrated that G_E and G_M can be interpreted as Fourier transforms of the nucleon charge and magnetization densities in the so-called Breit frame [16]. For elastic electron-nucleon scattering, the Breit frame coincides with the center-of-mass frame of the electron-nucleon system. Thus, the Breit frame is a special Lorentz frame in which no energy transfer is involved in this particular reference frame. One can therefore perform a three-dimensional Fourier transformation once the form factor information is available:

$$\rho\left(\mathbf{r}\right) = \int \frac{d^3q}{2\pi^3}e^{-i\mathbf{q}\,\cdot\,\mathbf{r}}\frac{M}{E\left(\mathbf{q}\right)}G_E\left(\mathbf{q}\right) \tag{1.6}$$

it is analogous to the classical charge density distribution. Finally, it is best pratice to describe the low q^2 behavior of a form factor in terms of a transition radius obtained from integral moments of the underlying density, but care must be taken with the relativistic relationship between a Sachs form factor and its intrinsic density ($\rho_{chg}(r)$ and $\rho_{mag}(r)$) [15].

1.1.1 Rosenbluth form factor separation method

The *Rosenbluth method* has been the only way to obtain values for G_E^2 and G_M^2 for nucleons until the 1990s. The Rosenbluth technique requires measuring the cross section for e-N scattering at fixed values of Q^2, for various scattering angles θ (i. e., at different beam energies) [4]. The cross section for *ep* scattering, in terms of the electric and magnetic FFs, is written as follow 1.7:

$$\left(\frac{d\sigma}{d\Omega}\right) = \left(\frac{d\sigma}{d\Omega}\right)_{Mott} \cdot \left[\frac{G_E^2\left(Q^2\right) + \tau G_M^2\left(Q^2\right)}{1+\tau} + 2\tau G_M^2\left(Q^2\right)\ tan^2\frac{\theta_e}{2}\right] \tag{1.7}$$

with $\left(\frac{d\sigma}{d\Omega}\right)_{Mott} = \frac{Z^2(\frac{e^2}{4\pi})^2\, cos^2\,\frac{\theta_e}{2}}{4p_0^2 sin^4\,\frac{\theta_e}{2}(1+\frac{2p_0}{M}sin^2\,\frac{\theta_e}{2})}$ and $\tau = \frac{Q^2}{4M^2c^2}$.

The Rosenbluth's formula 1.7 can be re-written, according to the preferred notation today, as follows 1.8:

$$\left(\frac{d\sigma}{d\Omega}\right) = \left(\frac{d\sigma}{d\Omega}\right)_{Mott} \cdot \left[G_E^2\left(Q^2\right) + \frac{\tau}{\epsilon}G_M^2\left(Q^2\right)\right]/(1+\tau) \tag{1.8}$$

where $\epsilon = \left[1 + 2(1+\tau)tan^2\frac{\theta_2}{2}\right]^{-1}$ is the virtual photon polarization [2].

The modern version of the Rosenbluth separation technique uses the linear dependence in ϵ of the FFs in the reduced cross section 1.8 and it can be written in this way 1.9:

$$\left(\frac{d\sigma}{d\Omega}\right)_{reduced} = \frac{\epsilon(1+\tau)}{\tau}\left(\frac{d\sigma}{d\Omega}\right)_{exp} / \left(\frac{d\sigma}{d\Omega}\right)_{Mott} = \left[G_M^2\left(Q^2\right) + \frac{\epsilon}{\tau}G_E^2\left(Q^2\right)\right] \tag{1.9}$$

where $\left(\frac{d\sigma}{d\Omega}\right)_{exp}$ is a measured cross section. Fitting several measurements of reduced cross section at the same Q^2 over a range of ϵ obtained changing the beam energy, E_e and electron scattering angle, θ_e, we can obtain independently $\frac{\epsilon}{\tau}G_E^2 p$ as slope and $G_M^2 p$ as the intercept, as shown in Figure 1.2 [4].

1.1.2 Proton form factor measurements

The Rosenbluth method shows (Figure 1.3) as the measurements of G_{Ep} and G_{Mp}, performed as the ratio over the dipole Form Factor G_D[1], appear to remain close to value

[1] $G_D = (1 + Q^2/0.71GeV^2)^{-2}$ with $G_{Ep} = G_D, G_{Mp} = \mu_p G_D$, and $G_{Mn} = \mu_n G_D$

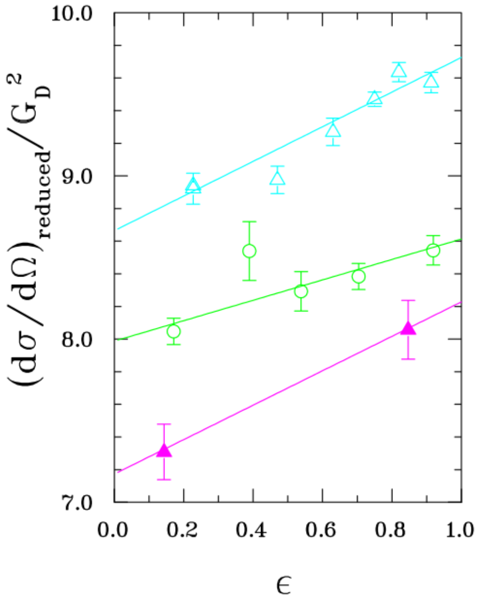

Figure 1.2: Slop of the Rosenbluth separation method .The Q^2 values shown are 2.5 (open triangle), 5.0 (circle) and 7.0 (filled triangles) GeV^2 [4]. The reduced cross section has been divided by the dipole form factor $G_D = (1 + \frac{Q^2}{0.71})^{-2}$.

1; This behavior suggested that G_{Ep}, and G_{Mp} have very similar spatial distributions to each other. However it is true that these results also strongly suggest a decrease of the ratio with increasing Q^2 [4].

It is clear enough from Figure 1.3 left that the cross section data have lost track of G_{Ep} above $Q^2 \sim 1$ GeV^2. It is very difficult to obtain G_E^2 for large Q^2 values by Rosenbluth method from *ep* cross section data for two main reasons; first, the factor $1/\tau$ multiplying G_E^2 in Eq. 1.9 reduces the contribution of this term to the cross section as Q^2 increases; and second, even at small Q^2, $G_M^2 \sim \mu_p^2 G_E^2$, therefore the contribution of G_E^2 to the cross section is reduced by a factor 7.80 [4].

1.1.3 Neutron form factor measurements

The neutrality of the neutron requires the electric FF to be zero at $Q^2 = 0$, and small at non-zero Q^2 ; historically, the fact that the electric FF is non-zero has been explained in terms of a negatively charged pion cloud in the neutron, which surrounds a small positive charge. Early attempts to determine the neutron FF were based on measurements of the elastic *ed* cross section. Recent cross section results for G_n^E are in Figure 1.4.

In an early experiment *Hughes et al.* [17] performed a Rosenbluth separation of quasi elastic $d(e,e')$ cross sections in the range $Q^2 = 0.04$ to 1.17 GeV^2 ; they observed non-zero values of G_n^E only below 0.2 GeV^2 but measured G_n^M up to 1.17 GeV^2; the technique consisted in comparing quasi-elastic *ed*, with elastic *ep* cross sections. The

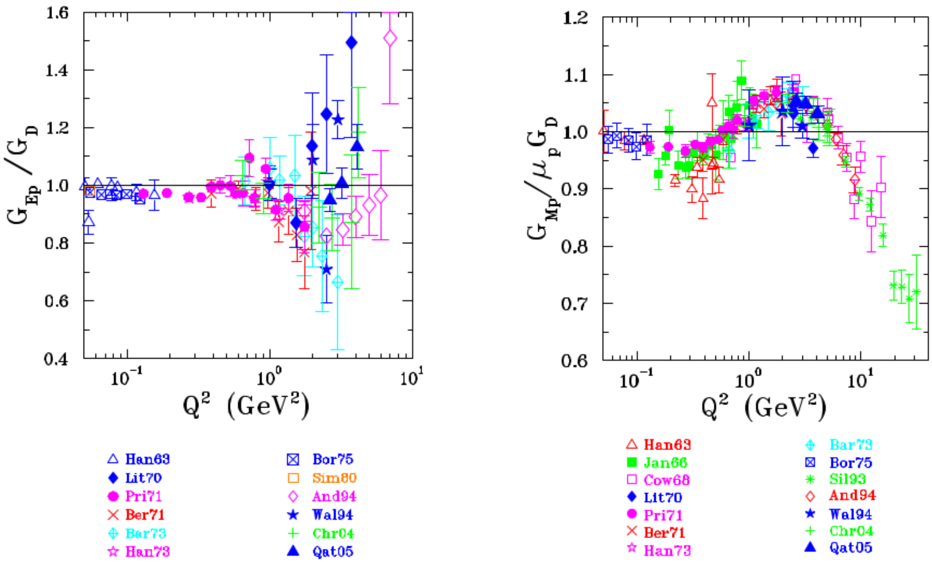

Figure 1.3: World data base for G_{Ep} (left) and G_{Mp} (right) obtained by the Rosenbluth method [4].

several experiments following Hughes can be subdivided into 3 groups: cross section measurements in quasi-elastic *ed* scattering; elastic *ed* cross section measurements; and cross section measurements in $d(e, e'p)n$. All recent cross section results for G_n^M are in Figure 1.4 [4].

1.1.4 Nucleon form factors from double polarization

The concept of double polarization to measure FF was highlighted for the first time in 1968 by *Akhiezer* and *Rekalo*. They explained as for large momentum transfers the separation of the charge FF of the proton is very difficult using the elastic *ep* reaction with an unpolarized electron beam, for several reasons (more info in [18]). The authors also shown that the best way to obtain the proton charge FF is with polarization experiments, especially by measuring the polarization of the recoil proton.

Further, in 1974 Akhiezer and Rekalo [19] discussed the interest of measuring an interference term of the form $G_E G_M$ by measuring the transverse component of the recoiling proton polarization in the $\vec{e}p \to e\vec{p}$ reaction at large Q^2, to obtain G_E in the presence of a dominating G_M.

Furthermore in 1982 *Arnold*, *Carlson* and *Gross* [20] underlined as the best way to measure the electric FF of the neutron would be to use the $^2H(\vec{e}, e'\vec{n})p$ reaction. Both a polarized target, and a focal plane polarimeter (to measure recoil polarization), have been used to obtain nucleon FFs.

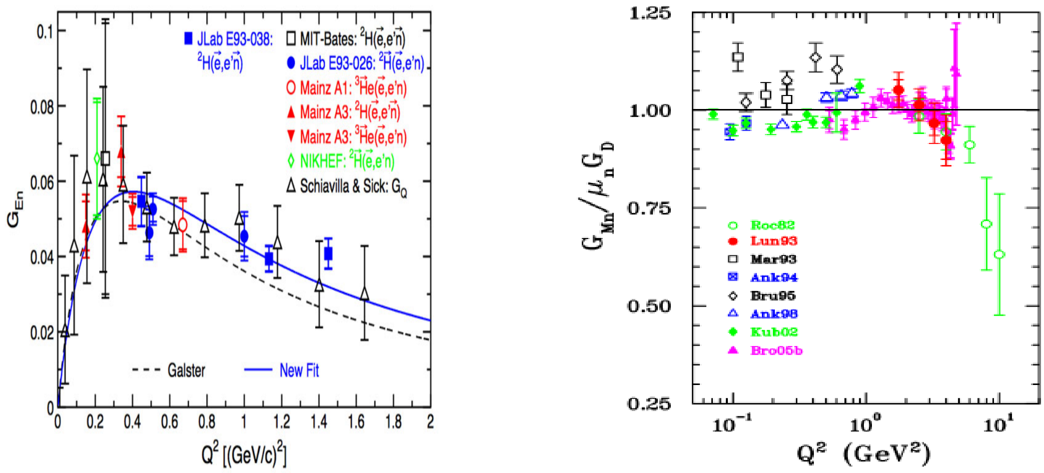

Figure 1.4: (left) G_{En} trend versus Q^2; (right) G_{Mn} data divided by μG_D from cross section data only [4].

1.1.5 Recoil Polarization Method (the *new* technique)

The relationship between the Sachs electromagnetic FF and the polarization transfer to the recoil proton in $H(\vec{e}, e'\vec{p})$ scattering was developed by Akhiezer and Rekalo, and later discussed in more detail by Arnold, Carlson, and Gross, as mentioned in the previous section. For single photon exchange, the three components of the transferred polarization are:

$$P_n = 0, \tag{1.10}$$

$$hP_eP_l = hP_e\left(\frac{E_e + E_e'}{m_p}\right)\frac{\sqrt{\tau(1+\tau)}G_{Mp}^2(Q^2)\tan^2\frac{\theta_e}{2}}{G_{Ep}^2(Q^2) + \frac{\tau}{\epsilon}G_{Mp}^2(Q^2)}, \tag{1.11}$$

$$hP_eP_t = hP_e\frac{2\sqrt{\tau(1+\tau)}G_{Ep}G_{Mp}\tan\frac{\theta_e}{2}}{G_{Ep}^2(Q^2) + \frac{\tau}{\epsilon}G_{Mp}^2(Q^2)}. \tag{1.12}$$

for the normal, longitudinal and transverse polarization components P_n, P_l and P_t, respectively; the $h = \pm$ stands for the electron beam helicity, and P_e for the electron beam polarization [2].

For each Q^2, a single measurement of the azimuthal angular distribution of the proton scattered in a secondary target gives both the longitudinal and transverse polarizations. Combining Eqs. 1.11 and 1.12 directly provides:

$$\frac{G_{Ep}}{G_{Mp}} = -\frac{P_t}{P_l}\frac{(E_e + E_e')}{2m_p}\tan\frac{\theta_e}{2}; \tag{1.13}$$

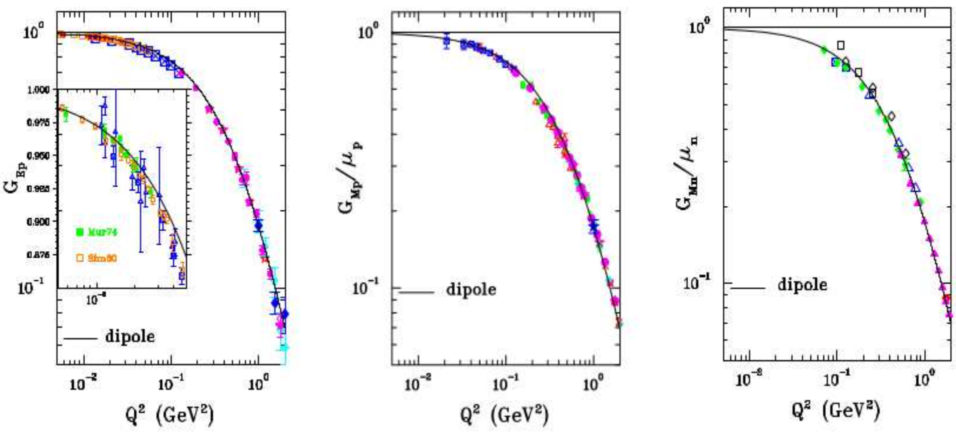

Figure 1.5: The Rosenbluth method results for G_{Ep}, G_{Mp} and G_{Mn} are shown in logarithmic plots, to emphasize the agreement with the dipole trend. As you may notice, there is a decrease of G_{Mp} and G_{Mn} for Q^2 data higher than 0.02 GeV^2, a consequence of the dominance of the electric FF at small Q^2 for the proton, as seen in Eq. 1.9 [4].

Measuring the polarization of the recoil proton, would be a more sensitive way to measure G_{Ep}, which is multiplied by G_{Mp} in the transverse component of the polarization, P_t, rather than the cross section, which is increasingly dominated by G_M^2 at large Q^2. Furthermore, another major advantage is that the radiative corrections are very low because polarization observables are ratios of cross-sections [4]. The results of the polarization data with the Rosenbluth method are illustrated in Figure 1.6.

Therefore, the study of nucleon form factors has seen an great revival thanks to discovery by *Jones et al.* [23], where they show G_E^p/G_M^p drop almost linearly with Q^2 above a four-momentum transfer of something like 1 GeV^2, in contrast to Rosenbluth. The plots (Fig. 1.6) show an important results: the apparent consolidated situation with the Rosenbluth separation method has been mined by a new class of measurements of FF ratio performed at JLab in the past decade by means of the polarization transfer method at relatively high $1 < Q^2 < 8\ GeV^2$.

As soon as the form factor discrepancy was verified, focus then turned to find the cause of this difference and the methods to reconcile the results. Many of the most important theoretical approaches make predictions about FFs, involving QCD and hadron structure. In fact, one possibility to explaining the data involves refined perturbative QCD calculations that include several variations in the quark light cone wave function. Also notable are relativistic constituent-quark calculations. Perhaps the most realistic model is a calculation out of Argonne by *Cloet, Roberts et al.* that uses an approach founded on the Dyson Schwinger Equations (DSEs) together with the Poincaré -covariant Faddeev equations. Finally, truly calculations of form factors using lattice QCD have been performed, some of which are extrapolated to a realistic pion-mass value using chiral perturbation theory [3].

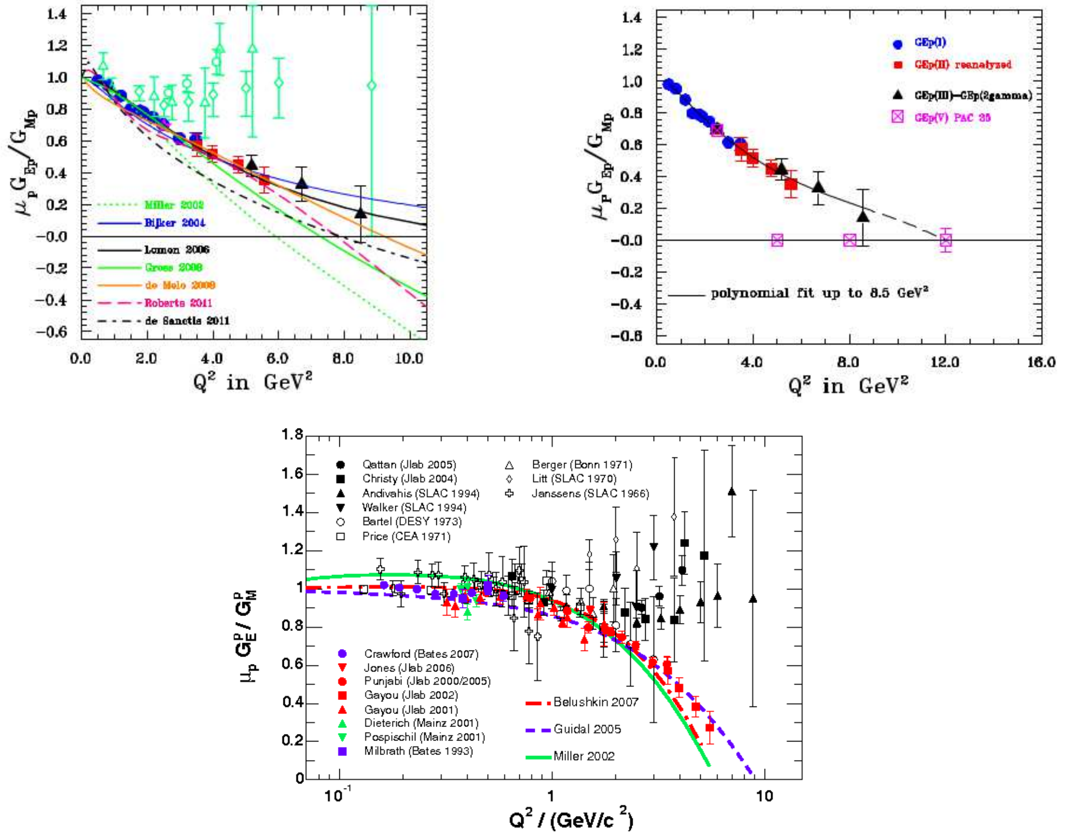

Figure 1.6: Top left: The ratio $\mu_p G_{Ep}/G_{Mp}$ obtained with the polarization transfer is shown as filled symbols, while the Rosenbluth results are shown as empty symbols. Top right: The three data points to be obtained in the GEp(5) experiment at JLab [7] [21]. Bottom: Existing data for measurements of the ratios of the electric and magnetic form factors of the proton from unpolarized measurements (black) using the Rosenbluth method and from double polarization experiments (colored). Also shown are three theoretical curves [22].

After a global analysis of the previous cross section data did not find any inconsistencies in the datasets, the higher order effects beyond the Born approximation were considered as a possible explanation. The Two-Photon Exchange (TPE) effects usually ignored in the standard treatment of radiative corrections were suggested as the likeliest explanation for the discrepancy. Therefore, the form-factor discrepancy has been interpreted as the failure of the one photon exchange approximation. The TPE effects are generally neglected in these corrections because the calculation of these effects require the knowledge of overall response of the nucleon to the virtual photon[5].

Previous calculations of such higher order corrections were found to be very small, typically below 1% of the Born cross section. A number of theoretical calculations were performed in order to estimate the size of the corrections necessary to resolve the discrepancy. In particular, contributions from elastic and excited nucleon intermediate states have been found to have a strong angular dependence when the finite size of the nucleon is taken into account, largely reconciling the Rosenbluth and polarization transfer measurements. A complementary approach, in which the TPE contributions have been calculated at the partonic level in terms of generalized parton distributions, was also found to reduce the Rosenbluth cross sections, bringing them closer to the polarization results [5].

Thus, the current state of FF experimental and theoretical studies (in general on the structure of the nucleon) requires to refine our understanding toward regimes where fundamental models differ significantly, as well as to small Q^2.

The JLab has played and is going to play a leading role thanks to the update of the polarized electron accelerator combined with a high beam intensity and the new experimental equipment in able to operate at high rates, given the low impact of the investigated processes. In light of all this, the new JLab experiments will provide many answers to a large number of questions of fundamental importance for understanding the properties of the nucleon and the nature of QCD in the confinement regime. The most extensive program will be carried out in Hall A, thanks to the *"Super Bigbite Project"* [24].

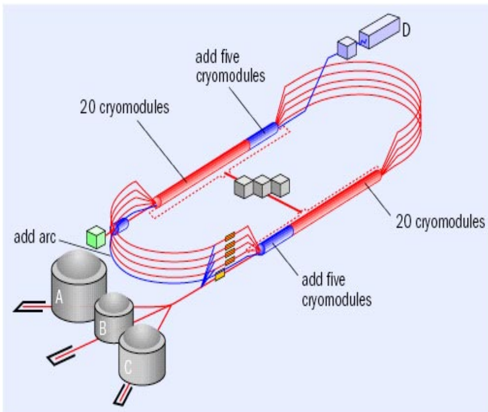

Figure 1.7: Left: Aerial view of Jefferson Laboratory. Right: CEBAF configuration.

1.2 The Super Bigbite Project Experimental Program on Form Factors

In this section, the experimental SBS program that incorporates five related measurements of the ground-state nucleon electromagnetic form factors (FFs) is presented. Doing this will require measurements at significantly higher values of Q^2, trying to obtain measurements on both the proton and the neutron with high precision. Until quite recently, this was very difficult. With the SBS program, however, a new level of precision can be achieved. The program will enable a discriminatory power that is quite unprecedented in the study of nucleon form factors [6].

Each of the experiments will use the electron beam from the upgraded 12 GeV CEBAF accelerator. Each measurement require a slightly different experimental setup, in fact they are designed so that they can be accomplished using largely common components that can be rearranged into the required configurations. This set of components has been developed within the *Super Bigbite Project* [24] and will form the *Super Bigbite Spectrometer (SBS)* and extended the detection capability of the existing (upgraded) *BigBite Spectrometer (BB)*.
SBS main requirements are: sustain large luminosity (beam current x target thickness) up to few $10^{38}/cm^2/s$, provide a moderately large acceptance with $\sim$ 1% momentum resolution at forward angles and polarimetry for recoil proton. The Super Bigbite Project bases on large-acceptance detection, makes use of an existing magnet, and will utilize a detector system with innovative GEM-based trackers.

In order to achieve this ambitious experimental program, it is necessary to have a tracking systems capable of managing significantly higher particles rates. Therefore, the Super Bigbite Project include a set of GEM (Gas Electron Multiplier) detectors (the main subject of this thesis) with the capability of sustain the high background rates and provide the required spatial resolution, and a 100-ton dipole magnet with a wide cutout-path for the electron beam, so that detection at forward angles is possible [3]. The Super Bigbite apparatus, however, based on the use of a larger magnet combined with GEM-based trackers, leads to a Figure-of-Merit that exceeds that of other competing efforts by a factor of 10 for G_E^p/G_M^p, around 30 for G_M^n, and 50 for G_E^n/G_M^n. The program not only will provides state-of-the-art capability, it is also enough economical, both in its use of new equipment, and in utilizing existing equipment (in particular, elements now associated with the original Bigbite Spectrometer) [3].

The Super Bigbite Project will make possible five ground-breaking measurements of the nucleon's elastic form factors, as shown in Table 1.1. These measurements will challenge existing theory of non-perturbative structure at unprecedented levels, and will discriminate between some of the best current predictions. The proposed measurements utilizing the SBS will provide many important answers by putting into play a technology that seemed impractical just a short while ago.

1.2.1 Proton Form-Factor Ratio Measurements up to 14.5 GeV^2 using Recoil Polarization

GEp(5) was the experiment that provided the original motivation for the Super Bigbite project. It will measure the ratio G_E^p/G_M^p using the polarization transfer method through the reaction $p(\vec{e}, e'\vec{p})$. In measuring of the nucleon FF ratio, this method mitigates the difficulties of the Rosenbluth separation method at high momentum transfer and is almost insensitive to the two-photon effects [7].

The polarization of the recoil proton will be measured using SBS. The scattered electron will be detected in the electron arm, in coincidence with the proton arm, by a large existing electromagnetic calorimeter called *BigCal* (originally constructed for GEp(3) [25]), having two GEM chambers installed in front. The target will be the standard Hall A LH_2 cryotarget [7]. A schematic representation of the experiment is

Reference	Label	Full Title	Apparatus
E12-07-109 [7]	GEp(5)	Large acceptance proton form factor ratio measurements up to 14.5 GeV^2 using recoil polarization method	SBS(*) and BB
E12-09-016 [8]	GEn2	Measurement of the neutron electromagnetic form factor ratio G_E^n/G_M^n at high Q^2	SBS and BB(*)
E12-09-019 [9]	GMN	Precision measurement of the neutron magnetic form factor up to $Q^2 = 18\ (GeV/c)^2$ by the ratio method	SBS and BB(*)
E12-09-018 [10]	SIDIS	Target Single-Spin Asymmetries in Semi-Inclusive Pion and Kaon Electroproduction on a Transversely Polarized ^3He Target using Super BigBite and BigBite in Hall A	SBS(*) and BB
E12-17-004 [11]	GEN-RP	Measurement of the Ratio G_E^n/G_M^n by the Double-polarized $^2H(\vec{e}, e'\vec{n})$ Reaction	BB(*) and NP

Table 1.1: Approved experiments for the *Super Bigbite Project*, which will use the GEM detector being developed and built by the Italy INFN collaboration. NP means Neutron Polarimeter and (*) indicates in which spectrometer INFN GEM tracker will be included.

shown in Figure 1.8.
GEp(5) will have excellent statistical power, with a Figure-of-Merit that is fully a factor of 10 greater than GEp(4) [3].

The spectrometer in the proton arm is based on a large open-geometry dipole magnet that is placed quite close to the target, and at a fairly small angle, a configuration that provides large solid angle at kinematics that have favorable statistics. The spectrometer will also be equipped with a double polarimeter that provides to improve the efficiency.

Super Bigbite uses a single dipole for magnetic analysis, has a relatively small field integral, and has an open geometry which means that the detector is in direct view of the target. While this approach has big advantages in terms of statistics, it has the drawback of high background rates [26] [12]. The Super Bigbite project, however, includes novel tracking detectors based on GEM technology, which have excellent rate-handling capacity. In fact the GEMs are able to handle an higher rate than we expect during the Super Bigbite measurements. These rates are based on experience of other past experiments together with GEANT and Monte Carlo studies 7.
The high particle rates are also mitigated using highly segmented detectors and an adequate number of tracking planes. In fact, the tracker system will consist in three side: The Front Tracker (INFN-Italy) and two Back Trackers (Second and Third associated with calorimeters, UVa-USA).

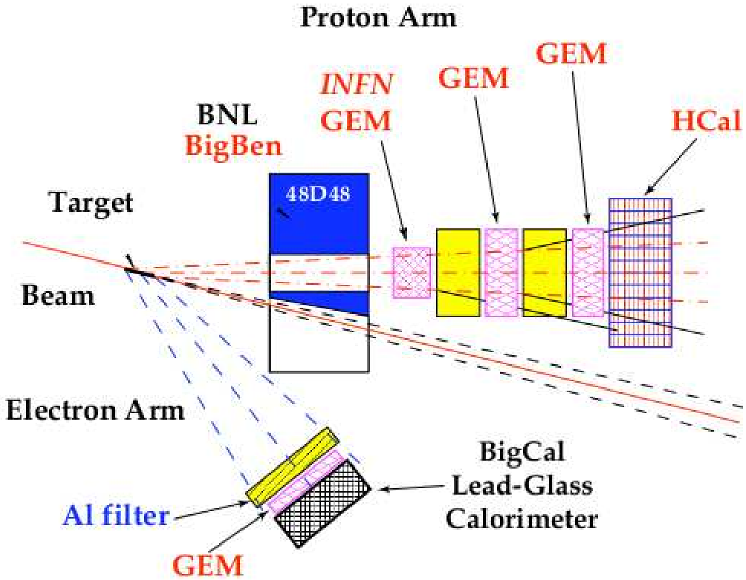

Figure 1.8: Shown is a schematic representation of the setup that will be used for GEp(5). The proton arm incorporates a GEM Front Tracker (INFN GEM), a double polarimeter instrumented with GEM trackers (GEM and yellow items) and a highly segmented hadron calorimeter (HCal). The electron arm uses the existing BigCal electromagnetic calorimeter based on lead glass [3].

1.2.2 Neutron Electromagnetic Form-Factor Ratio G_E^n/G_M^n up to $Q^2 =$ 10 GeV^2

GEn(2) experiment will measure a double-spin asymmetry in quasi-elastic scattering of polarized electrons from a very-high-luminosity polarized ^3He target using the reaction $^3\vec{H}e(\vec{e}, e'n)pp$. To study the quasi-elastic reaction, the electron will be detected in coincidence with the recoiling nucleon [27].

A schematic representation of the experimental setup is shown in Figure 1.9. The scattered electron will be detected using an upgraded version of the BigBite spectrometer. The BigBite detector package will include the above introduced GEM tracker system, divided into Front (INFN-Italy) and rear tracker (UVa-USA), that is being built as part of the Super Bigbite project. The recoil neutron will be detected using a large segmented hadron calorimeter (HCAL) and also in this case it will be used in the proton arm of GEp(5) [27]. The Super Bigbite magnet will be located between the target and the hadron calorimeter, in order to swipe out the charged particles.

GEn(2) is the only experiment that can provide precise measurements of G_E^n up to $Q^2 = 10\ GeV^2$, a regime that is critical to understanding G_E^n in terms of QCD degrees of freedom. The experiment builds on the success of GEn(1), but achieves more than an order of magnitude improvement in the Figure-of-Merit through the innovations mentioned above. GEn(2) will provide unprecedented insight into the ground-state structure of the neutron [3].

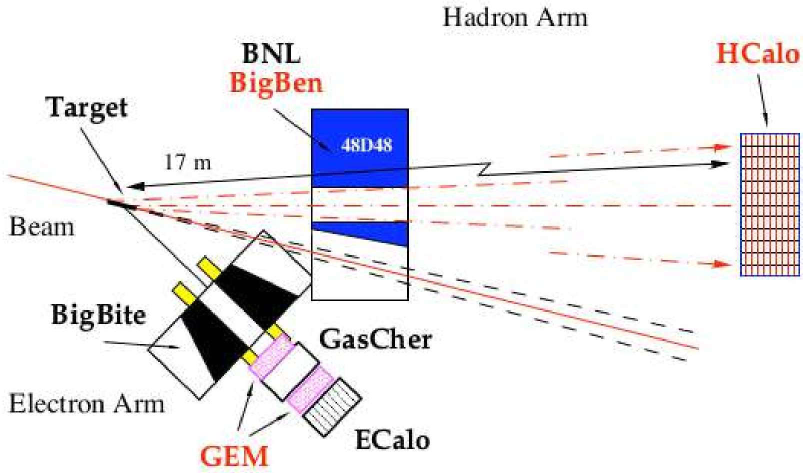

Figure 1.9: Schematic representation of the setup that will be used for the experiments GEn(2) (E12-09-016) and GMn (E12-09-019) [3]

1.2.3 Precision Measurement of the Neutron Magnetic Form Factor up to $Q^2 = 18$ GeV^2

GMn experiment will determine G_M^n by a detailed comparison of the unpolarized elastic cross sections of the two processes $d(e, e'p)n$ and $d(e, e'n)p$. It will use essentially the same apparatus as GEn(2), with the exception that the target will be the Hall A liquid deuterium cryotarget [9]. The schematic representation of the experimental setup was given above in Figure 1.9.

The GMn proposal include measurements up to 18.0 GeV^2 that, combined with the approved G_M^p measurement [28] (not part of the Super Bigbite project), would enable the reconstruction of the individual u and d quark distributions with a spatial resolution of 0.05 fm.

The Hall A GMn experiment will utilize the BigBite spectrometer and the Super Bigbite magnet will be placed in the hadron arm, in order to obtain an excellent separation between recoil protons and recoil neutrons. The magnet will also be turned on and off to study potential systematics [3]. The excellent statistical power of the Hall A GMn experiment is derived from many of the same factors that make the Super Bigbite experiments so powerful: very high luminosity, and an open-geometry spectrometer that is close to the target, and very good position resolution that permits strong suppression of accidental coincidences and inelastic events [9].

1.2.4 Measurement of the Ratio G_E^n/G_M^n by the Double-polarized Reaction

This experiment propose the measurement of double polarized $^2H(\vec{e}, e'\vec{n})]$ at a four-momentum transfer $Q^2 = 4.5\ (GeV/c)^2$. The ratio G_E^n/G_M^n will be extracted from the ratio of transverse and longitudinal components of the spin polarization P_x/P_z, which is transferred to the recoiling neutron from an incident, longitudinally polarized electron.

The experiment will be performed in Hall A of JLab, utilizing common components of the Super BigBite apparatus.
It will include apparatus to implement neutron polarimetry, using both $np \to pn$ and $np \to np$ scattering to analyze the neutron polarization. The electron arm will be the BigBite spectrometer. The hadron arm will be the neutron polarimeter consisting of a Cu block (the analyzer), GEM charged particle trackers, the CDet coordinate detector, the hadron calorimeter HCAL and a set of scintillation counters.
The polarimeter will be sensitive both to high-momentum forward-angle protons,to enable it to measure charge-exchange $np \to pn$ scattering, and to large-angle, low-momentum protons, to enable it to measure $np \to np$ scattering.

This experiment will yield G_E^n/G_M^n at the highest Q^2 kinematic point yet recorded. The information on the polarimetry will be used to optimize future measurements of G_E^n/G_M^n in Hall A and/or Hall C to reach Q^2 values as high as 9.3 $(GeV/c)^2$ using recoil polarimetry techniques [11]. A schematic representation of the experimental setup is shown in Figure 1.10.

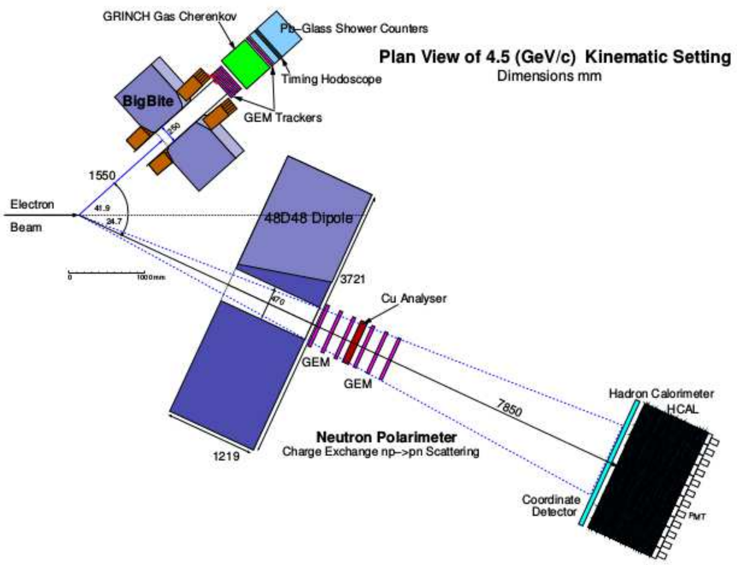

Figure 1.10: Schematic representation of the setup that will be used for the experiments GEN-RP [11].

1.2.5 Measurement of the Single Spin Asymmetries in Semi-Inclusive Pion and Kaon Electroproduction

Eperiment E12-09-018 [10] has been proposed and approved for the measurement of the the Single Spin Asymmetries of the Semi-Inclusive Deep Inelastic Scattering (*SIDIS*) process $\bar{n}(e, e'\pi^{\pm,0}(K^{\pm}))$, using the large-solid-angle Super Bigbite Spectrometer (SBS), the BigBite spectrometer, and a novel polarized ^3He target that includes innovative systems to achieve very high figure-of-merit. Both spectrometer arms will utilize GEM-based tracking to accommodate the high rates.

The azimuthal coverage is chosen to optimize the figure of merit of the measured asymmetries for the proposed apparatus, and is facilitated by collecting data at a series of ^3He (n) polarization directions. The SIDIS pions and kaons will be detected over a wide range of hadron momenta above 2 GeV, in a range of angles of the hadron momentum relative to the electron scattering plane and the momentum transfer.

The scattered electrons will be detected in the BigBite spectrometer and the SIDIS pions and kaons will be detected in the SBS where the refurbished RICH detector [10] will be used to discriminate pion-kaon and protons.

The BigBite detector package will be upgraded with the four GEM chambers (40 cm by 150 cm), a new segmented Gas Cherenkov Counter, a large 50 cm by 200 cm GEM chamber (from the package of the GEp(5) experiment), followed by an existing two-layer lead-glass calorimeter made of 243 blocks of 8.5 x 8.5 x 35 cm 3 dimensions. A new highly segmented scintillator hodoscope of 90 two-PMT counters between the two layers of the calorimeter will also be used [10]. The schematic setup is shown in Figure 1.11.

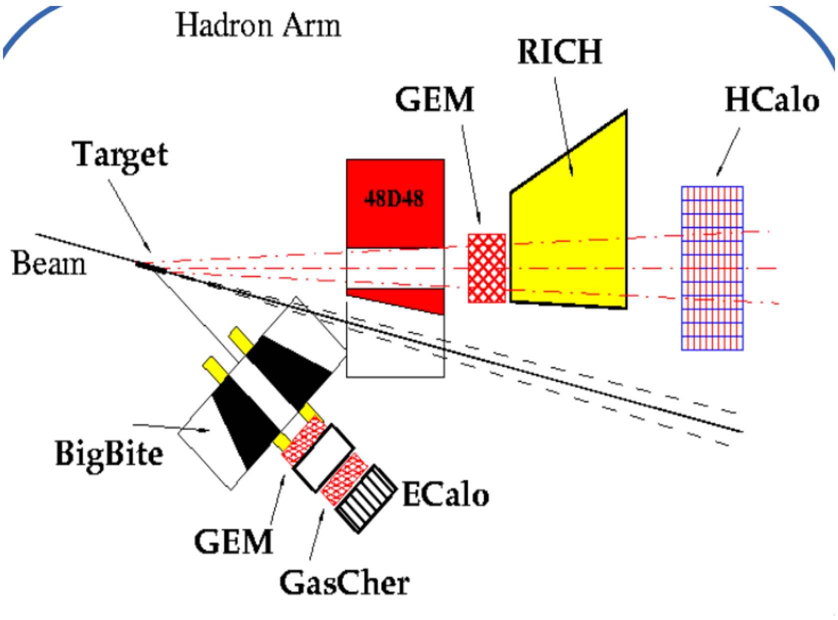

Figure 1.11: Shown is a schematic representation of the setup that will be used for experiment SIDIS [10].

Chapter 2

SBS project experimental apparatus

In all five experiments both the scattered electron and the recoil nucleon will be detected and this allows for the selection of the exclusive process (small cross section) at high momentum transfer. Below we will give a brief description of SBS project experimental apparatus, both for the hadron arm (SBS), and for the electronic arm (BB).

2.1 Super Bigbite Spectrometer - Hadron Arm

The instrumentation, the magnet and the detector package of SBS, includes a flexible kit that will be used in different configurations for each FF experiment.

The concept of the spectrometer proposed is based on advances in tracking detector technology, the GEM chambers, which allows tracking detectors to be used at a high luminosity in direct view of the target. This tracker, in addition to capability manage the high hit rate, also provides a very good spatial resolution. The good resolution, combined with the modest momentum resolution, allows the integration of a magnet with a relatively small field integral, several Tesla-meter, which will achieve a large solid angle (up to ~ 70 msr). These features combined will give SBS at least a factor of 10 advantage compared with any existing or proposed spectrometer at Jefferson Lab for nucleon form-factor measurements [12]. The Super Bigbite apparatus is shown in Figure 2.1 in the GEp(5) experiment configuration.

A short description about the main instrumentation is reported below.

2.1.1 The Magnet

The dipole magnet 48D48, operating in the SBS spectrometer, deflects charged particles vertically and will work with a field integral up to 3 $T \cdot m$. The relatively small bend angle is compensated for by the high spatial resolution (~ 70 μm) of the GEM front tracker resulting in a momentum resolution of 0.5% at 8 GeV/c in GEp(5) with the 40 cm long LH_2 target. The vertical bend will be achieved by rotating the magnet by 90°, directing the magnetic field in the horizontal plane. The possibility to istall of the magnet at small angles is obtained by a cut in the iron yoke. The cut make only a little distortion of the

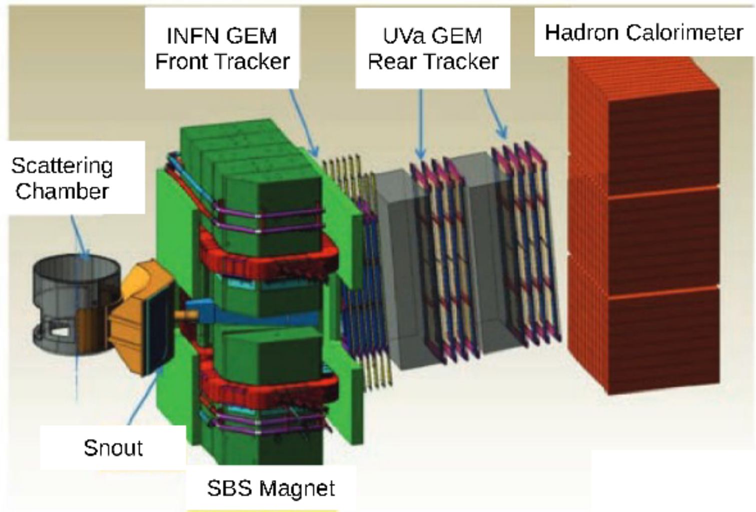

Figure 2.1: Shown is the SBS configuration, where it will consist of a dipole magnet with integral field up to 3 T, three charged particle trackers (one front and two rear trackers), two identical proton polarimeters (two CH_2 wall analyzers followed by the rear trackers), and an hadron calorimeter.

magnetic flux in the yoke and of the field distribution in the magnet gap. An additional 2D small plane of high resolution silicon detector (SiD), in front of the dipole, is located to improve the tracking accuracy, thanks to the longer effective length of the tracker, keeping the multiplicity per readout segment constant [29].

2.1.2 GEM Trackers

There will be three trackers in SBS for the GEp(5) experiment. The Front Tracker (FT) will be used to measure the proton momentum and its direction before interaction with the first CH_2 analyzer. The front tracker will be followed by a double polarimeter consisting of two trackers each one with a corresponding CH_2 analyzer. The second tracker (ST) will measure the proton track after the proton passes through the first CH_2 analyzer and the third tracker (TT) will measure the direction of the track after the proton passes through the second analyzer. ST and TT (form the Rear Tracker - RT) are only four chambers each (compared to six in the FT) because the same spatial resolution as the Front is not required and counting rates are lower.

The Italian group of the GEp(5) collaboration, composed of *Istituto Nazionale di Fisica Nucleare* (INFN) of Catania, Genova, Bari and Rome, have the responsibility for the development and construction of the front tracker. The FT will be subject to high background hit rates of about 400 kHz/cm^2 (based on GEANT and Monte Carlo simulations) due to the direct view of the target. The background is dominated by soft photons originating from the target. Low-momentum charged particles are swept away by the magnet. The rates on the second and third trackers are expected to be 130 kHz/cm^2 and 64 kHz/cm^2, respectively, dominated by soft electrons/positrons converted from photons in the analyzers [12].

2.1.3 Proton Polarimeter

The method of polarization transfer requires the measurement of the ratio of two components of the spin polarization, the longitudinal and sideways component. The first one component is parallel to the momentum of the proton after scattering, while the second component is transverse to the momentum of the proton in the electron scattering plane. The dipole magnet 48D48 provides the rotation of the proton spin around the direction of the magnetic field. In this way, the spin rotation angle is larger than the rotation of the proton momentum by 90°, so such rotation results in the proton polarization after the magnet being normal to the direction of the proton momentum. The transverse polarization of the recoil proton will be measured from the azimuthal asymmetry after re-scattering in a thick block of CH_2. The polar angle and the azimuthal angle of the re-scattered protons will be measured by the tracking detectors (ST and TT Tracker) located immediately after [12].

2.1.4 Hadron Calorimeter (HCAL-J)

The SB program experiments deal with very small cross sections, therefore for obtain relevant results the luminosity should be as high as possible. Arrangement of the trigger and the detector structure for the high luminosity should take maximum advantage of the high energy of the recoil nucleon. The energy of the nucleon in the these experiments ranges from 2 to almost 10 GeV.

HCAL-J is a sampling calorimeter with a modular structure where each module consists of 40 alternating layers of iron, in which the hadron shower forms, and 40 plastic scintillators sampling its energy. The active area (180 x 360 cm^2) consists of 288 modules, with a total weight of about 40 tons, arranged in a matrix with 24 modules in height and 12 in width. It has a good time resolution of $\sim$ 1 ns, high granularity (15 x 15 cm^2), a good coordinate resolution of 5 cm, and an high energy threshold. All these features make the HCal an attractive neutron detector for the two neutron experiments.

It will be positioned at the end of the SBS detector package and it will be used in the GEp(5) experiment to trigger the DAQ, in coincidence with the signals from the existing electromagnetic calorimeter, BigCal [30].

2.2 BigBite Spectrometer - Electron Arm

The existing BigBite spectrometer is being upgraded to handle expected increases in event rate and background rate due to the increased luminosity required for the experimental program and it will be used for electron detection. The BigBite configuration is shown in the Figure 2.2.

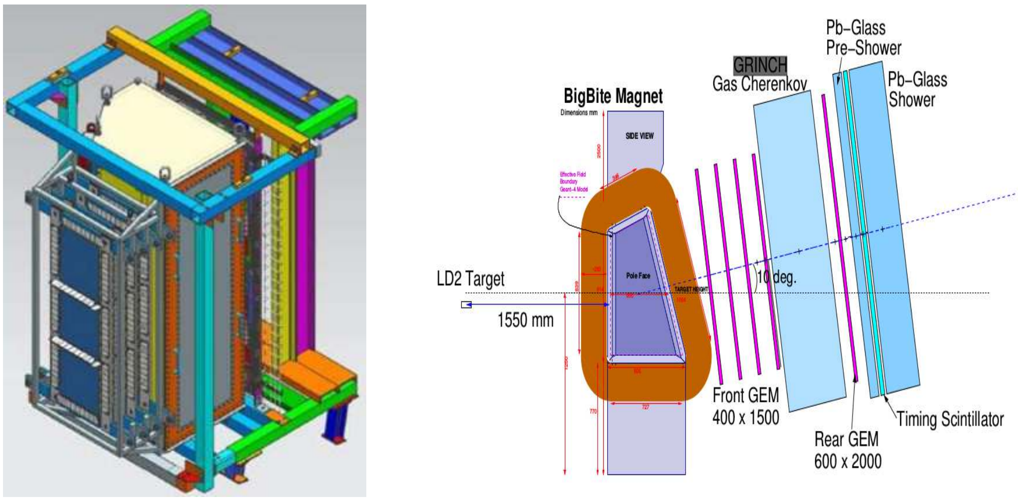

Figure 2.2: Left: shown is the BigBite configuration, where it will consist of Four GEM chambers (front) and one GEM chamber (rear) as tracker system, a Cherenkov counter and a large double-layer shower detector as trigger system and the BigCal calorimeter will be used for detection of the scattered electron. Right: the BigBite electron spectrometer scheme in GEN-RP configuration [11].

In its various configurations, it can consist of a dipole magnet, a tracker system based on GEM chambers, a Gas RINg CHerenkov (GRINCH) counter, a double-layer lead glass shower counter. In its most recent configuration, the 20 ton dipole has the entrance aperture at 155 cm from the target center, therefore the minimum central scattering angle that BigBite can reach is around 30°. The maximum integrated field is 1.2 Tm, so that for GeV electrons the bend angle is relatively small.

Four chambers of FT and one chamber of the RT of SBS will be used as tracker system and this reposition of the GEM chamber does not require any reconfiguration. Front and rear trackers will be separated by the GRINCH gas Cherenkov counter.

The GRINCH and the large double-layer shower detector will be used as BigBite trigger system; the detector will be used to separate good electron events from significant pion and electromagnetic contamination. Compared to the previous BigBite gas Cherenkov, which used 130 mm PMTs, this detector collect the light by four cylindrical mirrors and reflected on to a set of 510 9125 PMT's (diameter of 29 mm), that are more than 25x less sensitive to background. Cherenkov radiation clusters will be identified in this array using fast TDCs and a narrow timing window relative to typical ADC gates [31]. Timing from BigBite is provided by a plastic scintillator hodoscope.

BigBite is equipped with lead glass Cherenkov pre-shower and shower counters to provide a trigger which is insensitive to low energy background, but has a high efficiency for the electrons of interest. The pre-shower counter are oriented with their long axes perpendicular the electron direction and correlation of their signal amplitude with that from the shower counters provides an additional means for the discrimination of the electrons [11].

The calorimeter has 1744 lead-glass blocks coupled to PMTs. The blocks will be arranged in a matrix 20x75, a shape optimized for the largest acceptance at $Q^2 = 14.5$ GeV^2. The energy and coordinate resolutions of BigCal of about 5-7% and 7 mm, respectively, for 2.5 GeV electrons satisfy the trigger and tracking requirements. The distance between the calorimeter and the target will be 3 m at a central angle of 39° [12]. The angular correlation between the scattered electron and the recoil proton will be measured very accurately. This because of the small size of the electron beam, the angles of the electron and of the recoil proton can be determined with a very good accuracy of $\sim$ 0.5 mrad. In order to achieve this, a 1 mm coordinate accuracy is required for the scattered electron. Therefore, It will be provided by the Coordinate Detector, with a two-plane GEM-based chamber [12].

Chapter 3

SBS/BB GEM Front Tracker

3.1 GEM Technology

3.1.1 Choice of the technology

The main requirements for the SBS tracking system originate, as mentioned above, from the needs of the upcoming experiments to measure the nucleon form factors at high luminosity and high energy beams and they are [32]:

- to operate in high background particle rate ($< MHz/cm^2$)
- to provide good spatial resolution ($< 100\ \mu m$) for a single hit
- to provide a moderately high acceptance (40x100 cm^2 at least).

The tracking system requires the realization of relatively large detectors with minimum dead area in acceptance and minimum material budget. To fulfill these needs, we chose the GEM (Gas Electron Multiplier) technology.

When compared to other tracker systems, the GEM tech seems to be the best compromise for the requests of the SBS tracker system. Table 3.1 gives an overview of the order of magnitudes of the maximum achievable gain, hit rate and the spatial resolution for different trackers. In addition to performance, it is also high radiation hardness and low relatively inexpensive (for example if compared to silicon detector, with the same surface). GEM detectors have been preferred also because of their higher flexibility and re-usability [33].

Detector	Maximum gain	Maximum hit rate, [MHz/cm^2]	Spatial resolution, [μm]
Silicon microstrip	/	limited by the electronics	$\sim$ 1-10
Triple-GEM	$\sim 10^5$	$\sim$ 100	$\sim$ 70-80
MSGC	$\sim 10^4$	$\sim$ 10	$\sim$ 40-50
Drift chamber	$\sim 10^3$	$\sim$ 1	$\sim$ 50-150
MWPC	$\sim 10^3$	$\sim$ 1	$\sim$ 200

Table 3.1: Orders of magnitude of several tracker's properties compared for silicon microstrip detectors, triple-GEM, MSGC (MicroStrip Gas Chamber), drift chambers and MWPC (Multi-Wire Proportional Chamber) [33]

3.1.2 GEM chamber

The GEM technology was introduced by Fabio Sauli, in 1997 at CERN [34], as an electron amplifier in gas detectors. In the GEM chambers the primary ionization, multiplication and charge collection regions are physically independent, which provides greater flexibility in the readout geometry. Moreover, the possibility of dividing the multiplication of electrons in multiple steps, allows to reduce the problems of electrical discharge and aging processes [34].

The GEM chamber consists of one or more GEM foils immersed inside of a gas mixture. Each foil consists of a regular grid of bi-conical holes (Figure 3.1) in which an intense electrostatic field is present. The ionization electrons, produced by the particle passing through the chamber, are conveyed towards the holes by a suitable electrostatic field present between the foils; within the holes, the electrons are accelerated by the strong electrostatic field reaching enough energy to ionize the gas. The new ionization electrons undergo the same acceleration and finally produce a multiplication avalanche, which typically reaches a gain of 20 for single electron [34].

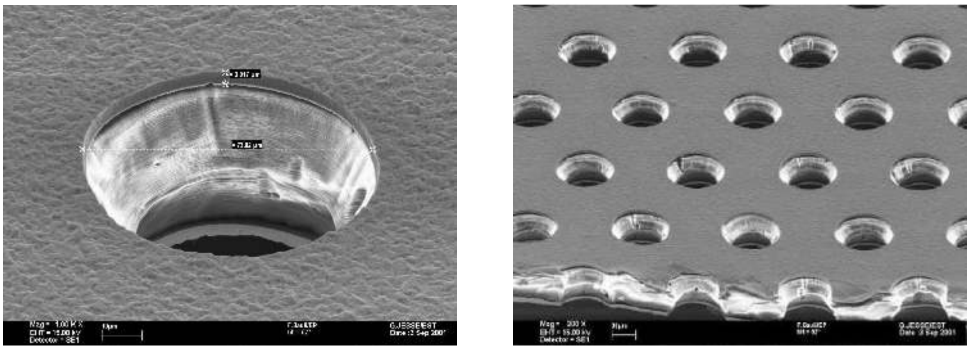

Figure 3.1: Electron microscope picture of a section of typical GEM electrode and of a its hole [33].

We can use various gases to fill a GEM detector. The choice depends on the specific needs, for example a high gain, high stability or low voltage. In principle, we can use all gases suitable for avalanche multiplication but the noble gases are normally preferred, because they have an high specific ionization. Specific ionization increases with the atomic number of the element; this makes Argon one of the preferred filling gases for a GEM detector [34]. The atomic numbers of Xenon and Krypton are still higher than Argon, but these gases are too expensive.

Together with the noble gases, the quencher has great importance, since it tends to absorb the photons x produced in the ionization: when an avalanche occurs, the gas atoms are ionized and excited, and they emit photons when they return to their ground-state. These photons could trigger new avalanches and create new trails of plasma, causing discharges. Its use is essential to avoid a permanent discharge mode when we seek the high gains. Methane, Ethane and Isobutene are examples of excellent inhibitors, but unfortunately these organic gases cause polymer deposits on the electrodes and can also cause discharges. For this reason, the carbon dioxide is the better choice of quencher. In fact, we use in a GEM detector a typical mixture of Argon and Carbon Dioxide (CO_2), with a ratio of 70/30 [33].

3.1.3 GEM foil

Typically a GEM foil consists of two thin copper films separated by a dielectric insulator in Kapton. The thickness of the copper is 5 μm, while the insulator is 50 μm. The diameters D (external) and d (internal) of the bi-conical hole are respectively 70 and 50 μm [34]; the distance P between the holes is 140 μm, as shown in figure 3.2.

In a GEM detector the hole acts as a multiplication channel for the electrons released by the ionizing radiation in the gas mixture. Applying a suitable potential difference ($\sim$ 300-500 V) between the two metal films, a relevant electric field is generated inside the holes ($\sim$ 100 kV/cm). This is the region where the electrons acquire enough energy to develop an avalanche that leads to a gain, which with a single GEM can be of the order of 10^3 [33] [34].

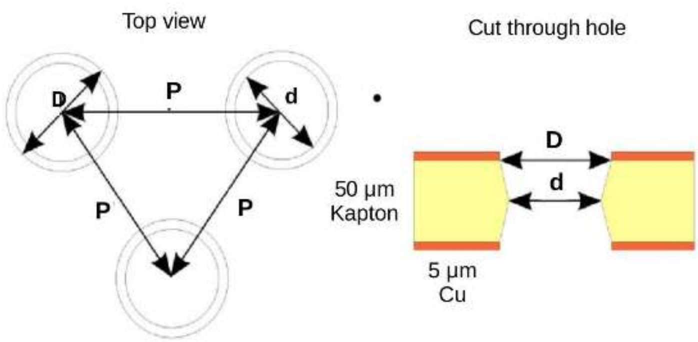

Figure 3.2: Typical geometry features of GEM foils with bi-conical holes [32].

In order to obtain a higher gain, the electrostatic field intensity shall be increased either by higher potential difference between the electrodes or by smaller hole diameter. Figure 3.3 shows the correlation between the gain and the diameter of the hole, measured under the same conditions (same mixture of gas and electric field) [35].

We observe a saturation effect in the gain for diameters below about 70 μm. This is due to the increasing losses of electrons in the avalanche (due to diffusion) towards the lower electrode [34]. The saturation effect has the positive aspect of reduce the dependence of the gain on precision in the GEM foil production. Part of the electrons and ions of the avalanche accumulate on the surface of the Kapton (*pile-up*), producing an alteration of the electric field inside the holes. The best geometry of the hole, which minimizes this effect, is the bi-conical one [35], as shown in figure 3.2

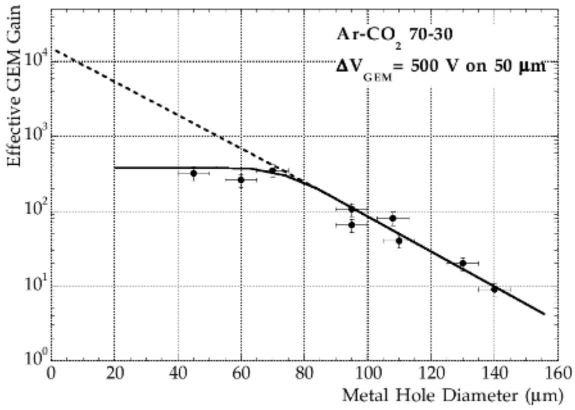

Figure 3.3: GEM effective gain as a function of the hole diameter [35].

3.1.4 Single GEM

The simplest gas detector based on GEM technology is the single-GEM chamber, where one GEM foil is inserted between two flat parallel electrodes. The top electrode plays the role of cathode while the bottom of anode. Figure 3.4 shows schematically a cross-section of a single GEM detector.

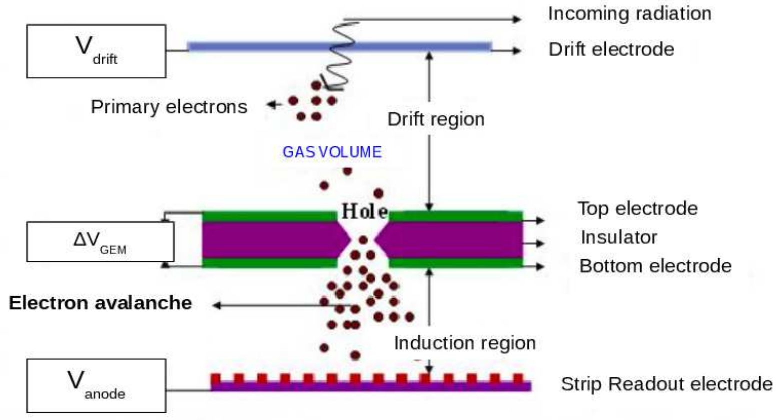

Figure 3.4: Schematic view of a single GEM, where the V GEM is the voltage difference applied between the copper layers of the GEM foil [32].

The drift field, E_d, is generated between the upper side of the GEM foil and the cathode, while the induction field, E_I, between the lower side of the foil and the anode composed of strips connected to the acquisition electronics, as shown in Figure 3.5 [34]. The ionization electrons, produced in the inter-space from the charged particle passing through the detector and following the drift lines, move towards the holes of the GEM, where they are multiplied. The induction field transfer the most of the multiplied electrons inside the holes to anode, giving rise to an current signal.

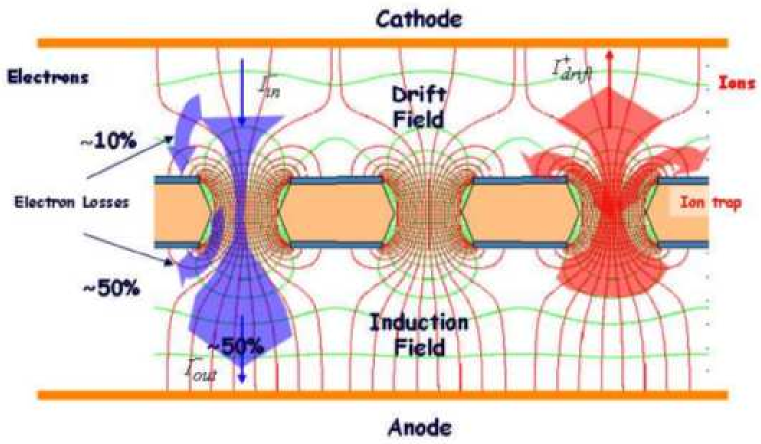

Figure 3.5: Qualitative operation scheme of a single-GEM detector [36].

The fraction of ionization electrons transferred through the GEM foil (*transparency*) depends on the drift field and it decrease at high values due to losses to the top GEM electrode (de-focusing of the field lines outside the holes), as shown in Figure 3.6 [34].

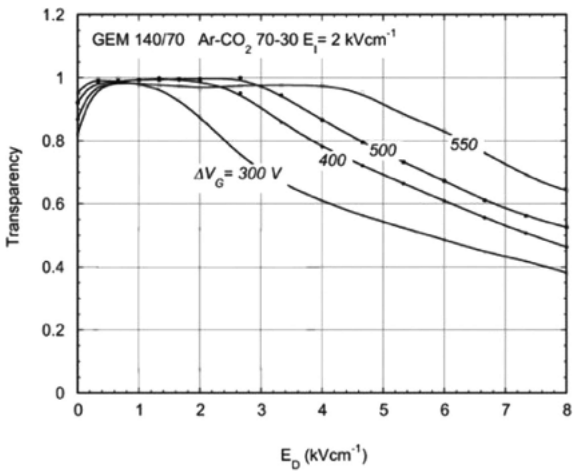

Figure 3.6: Electron transparency of a typical GEM electrode as a function of drift field for fixed induction field, for several values of GEM voltage [34].

The task of the induction field is to extract the electrons multiplied by the holes and transfer them towards the anode. At low values of the induction field, most secondary electrons are practically collected on the lower part of the GEM and the signal induced is reduced. Instead, increasing the induction field, the secondary electrons are collected on the readout electrode, increasing the output signal [35]. A very high induction values, greater than 8 kV/cm, can cause discharges on the anode due to the high electric field near the edges of the readout electrode [34]. In fact, the better configuration can be with low electric fields in the drift zone and high field in the induction zone. Induction field values around 5 kV/cm are a reasonable compromise to collect a large fraction (about 50%) of the charge on the PCB (Printed Circuit Board).

The intrinsic gain G_{int} of a foil is directly proportional to the voltage applied to the GEM (V_{GEM}), according to $G_{int} \propto e^{\alpha VGEM}$, where α is the first Townsend coefficient along the path of the electrons through the hole. Generally, the intrinsic gain of a detector of single-GEM is of the order of 5000 but can decrease up to 10^3 for dispersive causes. As a result, the resulting effective gain is smaller than the intrinsic.

For a GEM detector we can define two fundamental quantities, such as:

- Collection efficiency (ϵ^{coll})
- Extraction fraction (f^{extr})

The **collection efficiency** is given by the ratio between the number of electrons entering inside the holes and the number of primary electrons generated above the GEM foil. The former depends on the electric field above the GEM and the electric field inside the hole, as seen before [33].

In case of electronegative gas mixtures, additional primary electron losses can occur before the multiplication, due to the recombination effects. For this reason we use the noble gas; their external electronic shell being complete, they cannot capture extra electrons [36].

The **extraction fraction** represents the ratio between the number of electrons extracted from the holes and transferred to the PCB and the number of electrons multiplied inside the amplification channels. Also in this case, it depends on the electric field inside the hole and the electric field below the GEM.

Simulation studies (with $E_I = 5$ kV/cm) show that a negligible percentage of the inner electrons are trapped at the surface of holes, due to the diffusion, and about 10% of ions is captured in the proximity of the hole exits. The remaining exiting electrons are either collected at the bottom electrode of the GEM or transferred to the induction region. In this case, a fraction of approximately 50% of multiplication electrons are lost on the bottom electrode of the GEM foil and the other 50% go towards the readout (Figure 3.5) [36]. From the two factors, ϵ^{coll} and f^{extr}, we introduce the concept of the effective gain, G_{eff}, correlated with the intrinsic gain of a GEM foil, G_{intr} through the following relation:

$$G_{eff} = G_{intr} \cdot \epsilon^{coll} \cdot f^{extr} = G_{intr} \cdot T \tag{3.1}$$

where we have defined the electron transparency T of the single-GEM detector as the product of $\epsilon^{coll} \cdot f^{extr}$. The maximum effective gain reachable with a single-GEM detector is of the order of 10^3. Higher gain, up to 10^4 - 10^5, can be achieved by assembling more than one GEM foil in cascade at close distance one to each other, realizing the multi-GEM detector (double or triple GEM) [36].

3.1.5 Triple GEM

A triple-GEM detector consists of three GEM foils stacked and inserted between two electrodes, a cathode and an anode, as shown in the schematic Figure 3.7. The use of three GEM foils allows to achieve a higher gain, without requiring too much high voltage applied to each GEM foil. The potential differences applied between the various GEM films are named $V_{GEM\ 0}$, $V_{GEM\ 1}$, $V_{GEM\ 2}$, and their sum V_{GEM}^{tot}.

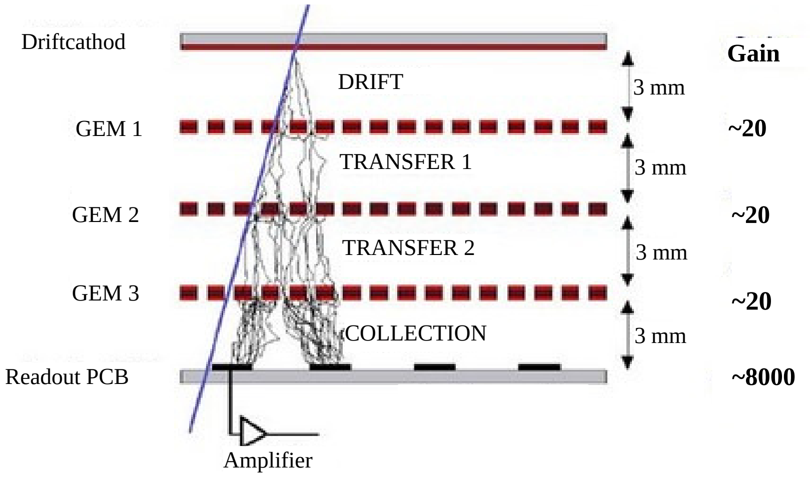

Figure 3.7: Schematic cross-section view of a triple-GEM detector [32].

The description of the single GEM chamber, discussed in the previous section, allows to understand the operation of a triple-GEM detector. The space between the cathode and the first GEM foil acts as a drift zone. The space between the last foil and the anode is the induction zone, where the charge induces the signal on the readout anode. As for the spaces between consecutive foils, these are called transfer regions. They act as an induction region, if they refer to the overhead GEM, while as a drift region, if they refer to the lower GEM. The purpose of the transfer field is to transport the secondary electrons produced in the holes from a top foil to the next one. This implies that the value of the transfer field must be chosen in order to simultaneously maximize the extraction fraction from a higher GEM and the collection efficiency of the lower GEM.

Figure 3.8 represents the induced current on the readout as function of the transfer field for a mixture of Ar/CO_2 gas (80/20), for a certain value of the drift and induction fields ($E_D = 2\ kV/cm$; $E_I = 5\ kV/cm$). We can see that for low values of the transfer field ($E_T < 3\ kV/cm$), the flow of electrons has a low extraction fraction. Actually, the electrons created are extracted from the upper holes but they are mainly collected on the lower electrode of the same foil. On the other hand, a high transfer field ($E_T > 4\ kV/cm$) implies a poor collection efficiency due to a high de-focusing effect.

For a triple-GEM detector the intrinsic gain is an exponential function of V_{GEM}^{tot}. Together with the electric field in the various gaps, that define the total electron transparency as the product of the transparency of each foil ($\prod_k T_k$), the effective gain (G_{eff})

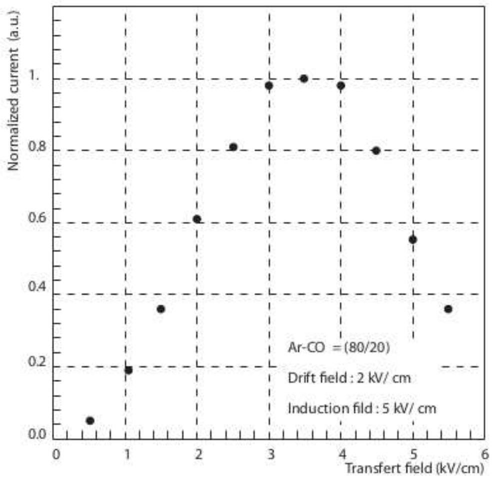

Figure 3.8: Induced current as a function of the transfer field (for equal transfer fields between the GEM foils) [33].

of the detector is defined as follows:

$$G_{eff} = G_{intr}T_{tot} = \prod_{k=0,2} e^{\langle\alpha\rangle_k \cdot V_{GEMk}} \cdot T_k = e^{\langle\alpha\rangle^{tot} \cdot V_{GEM}^{tot}} \cdot \prod_{k=0,2} \epsilon_k^{coll} f_k^{extr} \tag{3.2}$$

where $\langle\alpha\rangle$ is the average of the first Townsend coefficient of the electron path through the hole, ϵ_k^{coll} and f_k^{extr} are the collection efficiency and the extraction fraction of the k^{th} GEM foil.

Since the effective gain depends on the voltage applied to the three foils, the better way could be increase the voltage applied on the first GEM foil, reducing the one on the third foil. In this case, the charge reaching the third layer is greater, but the diffusion effect allows the electronic cloud to be distributed over a greater number of holes, reducing the probability of discharge. Several studies allow to choose the GEM configuration that minimizes the probability of discharge, like the follow [36]:

$$V_{GEM\ 0} \gg V_{GEM\ 1} \geq V_{GEM\ 2} \tag{3.3}$$

3.1.6 The electric discharge probability

A defect in the GEM foil can give rise to an electric discharge. These defects can be holes not geometrically regular, the copper film/Kapton not regular but also micro-particles (dust) inside the holes. The electric discharge will be visible as a spark on the foil. A discharge could also be obtained when a foil is in good condition and a good flow of gas but the avalanches created inside the holes reach the Raether limit (of the order of 10^7 pairs of ions) [34].

During the development of the avalanche, the gain is less than 10^6, but if the number of ion pairs further increases, for example due to the increase in the external voltage applied to the electrodes, the electric field is perturbed by excessive space charge in the gas. Therefore, when the pairs created reach a critical value close to the Raether limit, they form a concentration of charges forming the avalanches less contained, called *streamer*.

The photons that are produced during the excitation phenomena of the atoms or molecules have a fundamental role. The energetic photons are able to ionize the atoms of the electrodes, ejecting electrons. When this happens on the cathode, the ejected electrons will form secondary avalanches, which are attracted towards the positive tail of the streamer. In this way the streamer moves close to the cathode until it touches it [33]. As soon as the streamer's head touches the anode, a strip of plasma will form between the cathode and the anode, triggering a discharge, visible as a spark. Therefore, the voltage applied to the GEMs plays a fundamental role both for the formation of avalanches and for discharges on the foils.

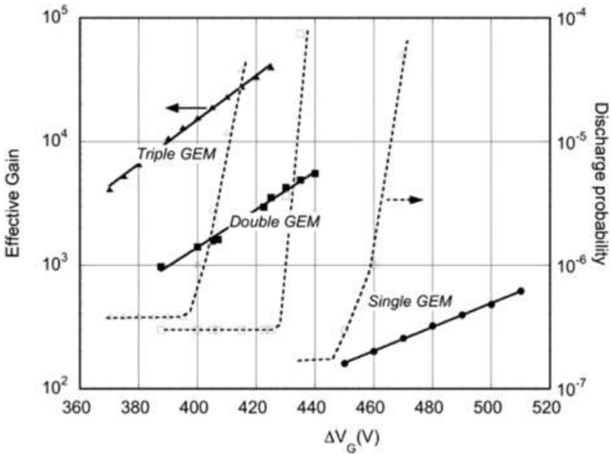

Figure 3.9: Effective gain and probability discharge as a function of voltage in multi-GEM detectors [34].

Figure 3.9 shows the gain and the probability of discharge of 3 GEM configurations as function of the voltage applied to GEM foil. From the graph we note that the effective gain of a triple GEM, compared to double, is higher with the same voltage applied. While for the single GEM, we need apply a very high voltage to obtain a gain near to 10^3, increasing significantly the probability of discharge [34]. Therefore, the use of the triple-GEM detector allows to increase the gain by keeping the voltages applied to values sufficiently low in order to reduce possible problems.

3.2 Front Tracker Geometry

The SBS program front tracker will consist of several consecutive identical GEM chambers (six for SBS and four for BigBite) with an active area of 40x150 cm^2, as shown in Figure

3.11. Each chamber is composed of three adjacent triple GEM modules (40x50 cm^2), as shown in Figure 3.10 left [12]. We allocate the front-end electronics on four backplanes around each module and one of the them is flexible and placed at 90° with respect to the chamber, between two modules nearby, as shown in the Figure 3.10 right.

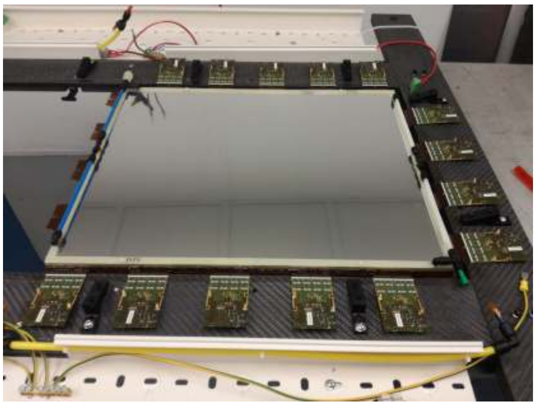

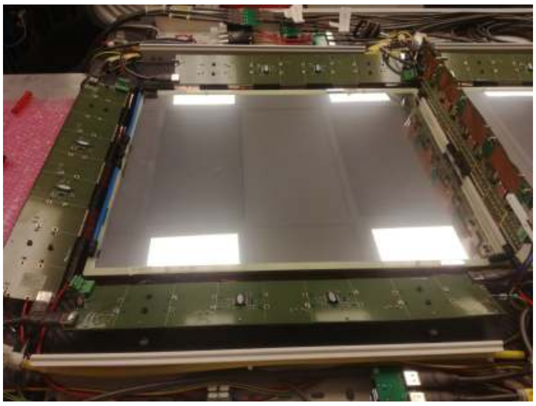

Figure 3.10: Left: GEM module 40x50 cm^2 inserted inside the carbon frame during the assembly of the chamber for SBS Front Tracker in July 2018; Right: Backplanes (green components) around the GEM module, where one of them is upright (on the right of the figure).

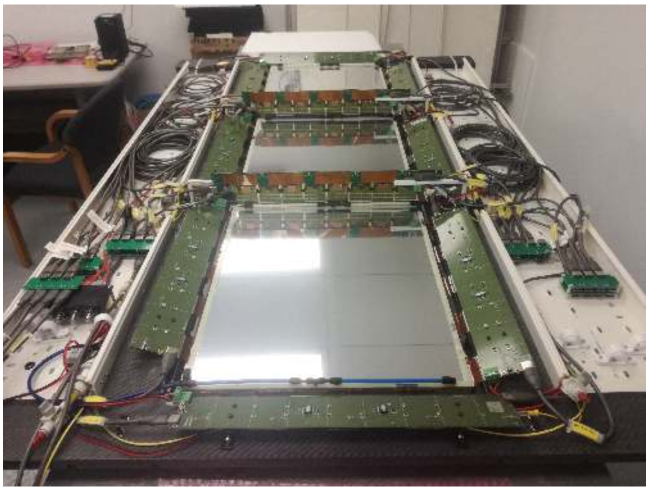

Figure 3.11: Three adjacent GEM modules assemble a GEM chamber for SBS Front Tracker (July 2018).

3.2.1 Readout plane

The structure of the readout plan can be easily adapted to the experimental needs, for example by using strips of different forms connected to the front-end electronics. The readout foil in the SBS/BB GEMs is inspired to the COMPASS 2D [37] readout strips layers. It consist by a copper-plated Kapton foil on one side, with double strips at 90°.

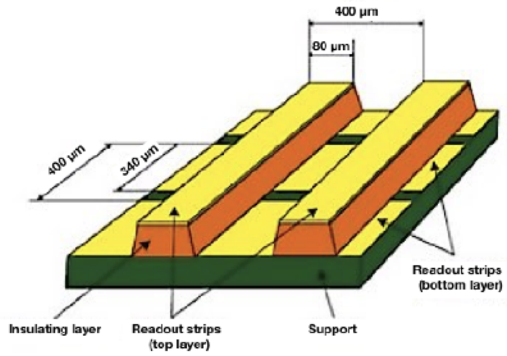

Figure 3.12: Representation of double strips at 90° in x/y coordinates on the readout plane [32].

This readout is formed by 0.5 μm thick copper strips and they are realized (due to the electrostatic field) so as to be able to collect an equal charge distribution for the x and y coordinates. In both layers, the strips have pitch of 400 μm, as shown in Figure 3.12, since they must not be wider than the transverse size of the electron cloud (about 500 μm) incident on the strip [32] [33].

Due to the high background expected for the SBS project, an implementation of readout plans in U/V (± 30°) coordinates is planned for the rear tracker, in order to reduce the tracking ambiguities.

3.2.2 Front-end electronics

The readout electronics developed for the readout SBS GEM front trackers is based on the APV25 chip (Analogue Pipeline Voltage) developed by the Imperial College for CMS silicon detectors and firstly used in a GEM detector by COMPASS [38].

The readout electronics for each GEM module consists of [38]:

- 18 front-end cards (FEC), hosting the APV25 chip, are located on backplanes around the module;
- 4 backplanes that represent a passive electronic part and at the same time the mechanical support of the front-end cards; each one hosts a voltage regulators that supply the proper voltage levels to the cards, and the lines for the distribution of the digital and analog signals going to and coming out from the cards;
- 2 VME64x/VXS module MPD (Multi Purpose Digitizer) that control the cards located on the backplanes and acquires the analog signals coming from them through HDMI cables.

The APV25 chip is an analog pipeline ASIC (Application Specific Integrated Circuit) with serial output. Each APV25 has 128 channels, each containing a preamplifier and shaper, followed by a 192 cells analog memory, into which continuously sampling the shaped signal at 40 MHz frequency. Therefore, a sample corresponds to the charge collected on the readout strips during a sampling period of 25 ns. We can acquire up to 6 samples (limited by the memory buffer) to follow the signal time evolution.

A single APV25 is hosted on a front end card which is directly connected to 128 strips by a Flexible Printed Circuit (FPC) [32], as shown in Figure 3.13 left. Both APV25 card and backplane are designed to be radiation tolerant; around 10 Mrad for the first one and 0.36 Mrad for the second one (tested under irradiation by ^{137}Cs), corresponding to more than 4 JLab-year of operation. The backplane and the MPD are connected by 2 HDMI cables, one for the digital signals and the other for the analog output coming from the cards [38].

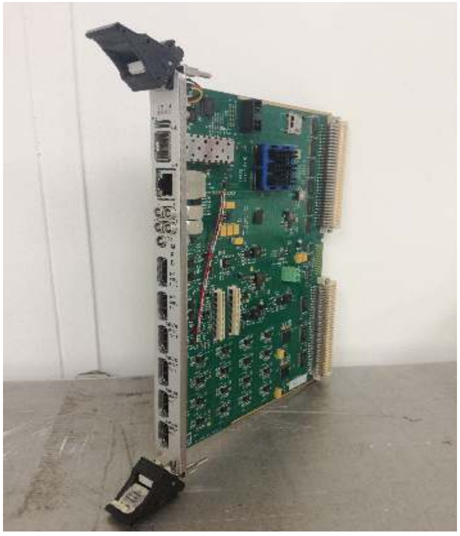

Figure 3.13: Left: Front End Card with APV25 chip (below the shielding copper plate) connected to 128 strips by the Flexible Printed Circuit on top; Right: the MPD module [32]

A single MPD (Figure 3.13 right), a custom VME-64x compliant module with a high performance optical link, controls and readouts up to 16 FEC (for 2048 channels, as a total). The VME-64x standard has been adopted to be compliant to the JLab DAQ main framework. The MPD distributes the control signals (digital line) to the FECs and reads out their analog outputs in parallel, digitizes them and transfers to the DAQ acquisition node by VME or fiber optics. The MPD module hosts an Altera ARRIA GX FPGA (Field Programmable Gate Array), which is an integrated circuit with functionalities programmable by firmware and allows the implementation of logical functions with a certain complexity [38].

3.2.3 APV25 signal

In order to study the generic time evolution of signal processed by the APV25 chip, we collect 6 samples at 25 ns period. The timing evolution of the APV25 signals can be approximated by a double-exponential (or bi-Gaussian) function [39] with four parameters, as shown in (3.4), where t_0 represents the start time of the signal; τ_1 and τ_2 the leading and trailing time constants and A the amplitude.

$$A(1 - e^{-\frac{(t-t_0)}{\tau_1}})e^{-\frac{(t-t_0)}{\tau_2}} \tag{3.4}$$

In chapter 5 we will discuss alternative, simpler, expressions that can fit the samples adequately well. Figure 3.14 shows a typical APV signal fitted by the double-exp function: the time on the x-axis and the charge values collected by the single strip in ADC [1] units on the y-axis.

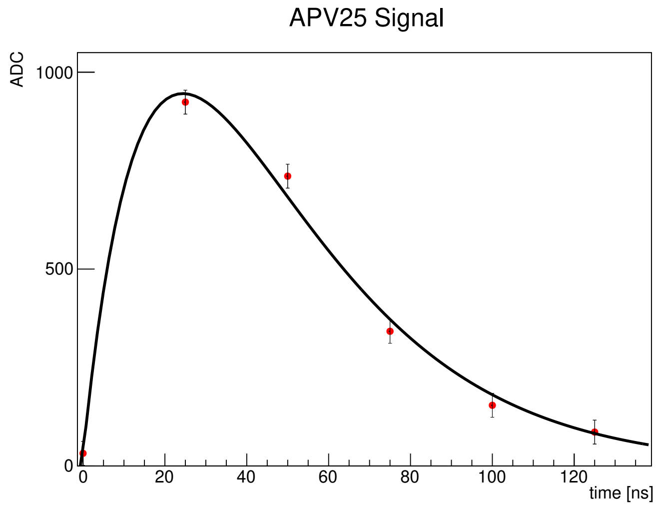

Figure 3.14: Example of time trend of a APV signal approximated by the double-exponential function (for $t > t_0$ and 0 for $t \leq t_0$). This distribution of charge has sampled every 25 ns and has been produced by X-ray beam (HV=15 KV, I=20 μA). Each point represents a sample of charge, expressed in ADC units.

The noise associated to the chamber and electronics can be estimated, as typically done, by the RMS of the pedestal. Noise level is sensitive to the different environmental conditions, to the intrinsic noise of electronics and to the length of the HDMI analog cables (around 1 ADC unit per meter) [38]. The typical pedestal RMS of the 128 channels of a single APV card, under recent cosmic ray test at JLab with the final electronics on front tracker GEM module, is shown in Figure 3.15. The few noisy channels in the tail are related to the unavoidable mismatch in the analog HDMI cable which can be mitigated by off-line filtering.

In section 5.2.2 we will discuss in detail the temporal performances of the function mentioned above and introduce an approach for noise/background reduction in the collected data, at firmware level.

[1] Analog to Digital Converter and it corresponds about to 150-200 electrons.

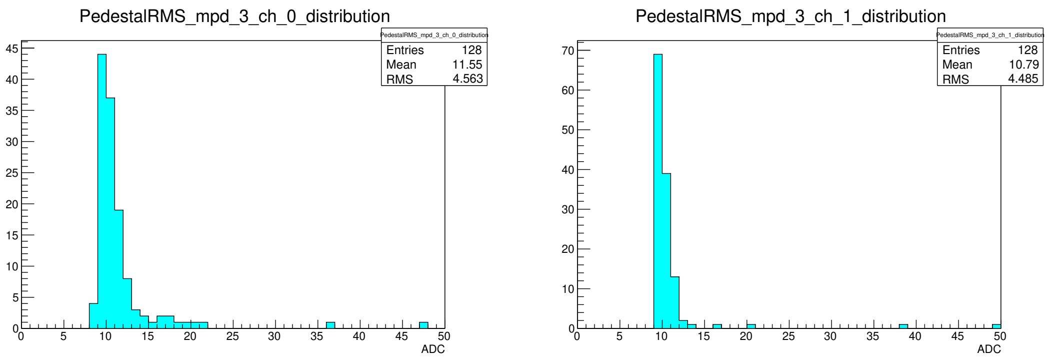

Figure 3.15: Front end card pedestal during a cosmic ray tests (JLab 2019), where the charge distribution in ADC unit for two APV cards (128 channels each one) are shown. As can be seen, they bring an average value of about 11 ADC units.

Chapter 4

GEM tracker: from construction to commissioning

The process of GEM construction and then integration into the SBS consist of different steps from critical components quality checks to GEM chamber commissioning, as described in the next sections. We briefly illustrate each single phase and process.

4.1 Foil Quality Check

Before using a GEM foil into a detector (or module in our case), we need to check its quality to highlight the possible anomalies on the foil, both electrical and manufacturing.

The adopted quality control procedures take into account discussions with the GEM foil producers at CERN, the LHCb INFN-LNF, and UVa (University of Virginia) groups, as well as experience from CMS [40] and ALICE TPC [41].

The purpose of the quality test is to verify the leakage current through the Kapton layer, when we apply a voltage, up to about twice the working voltage at JLab (~ 550 V), on the two copper layers for a sufficiently long time to stabilize the electrostatic field around and within the GEM foil. An abnormal behavior during the test may indicate the presence of foil defects. These anomalies can be caused by manufacturing defects (for example holes not geometrically regular), by micro-particles that remain blocked in the GEM holes and influence the behavior of the foil or by burned (carbonized) material and micro-defects of the kapton layer which may collapse when HV is applied. Sometimes this unusual behavior can be solved by flushing nitrogen and/or rolling the electrostatic roller on the foil, clearing the holes from impurities.

We perform the tests, inside the clean room of the INFN Sezione di Catania, of each GEM foil using a CAEN N1471 [42] power supply to apply the required voltage on the foil, and a *Keitley* 6517B electrometer [43] to measure the leakage current with an accuracy of about 0.1 nA, both HV power supply and electrometer are controlled and monitored by *LabVIEW* that reads and records the voltage and current every second for off-line analysis.

We arrange the GEM foil inside a plexiglass box, where Nitrogen is flushed to reduce the humidity level (on average under 10%) and to provide a stable and reproducible environment, as shown in Figure 4.1 right.

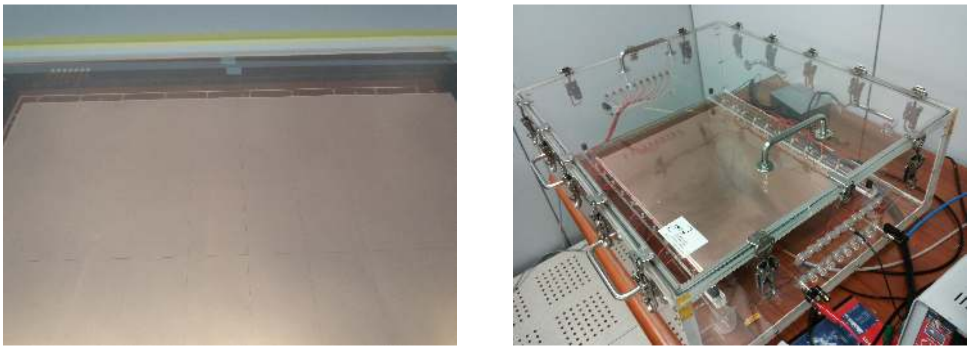

Figure 4.1: Left: detail of a GEM foil where its subdivision in 20 sectors is possible to observe (2 rows of 10 sectors). Right: box filled with Nitrogen and GEM foil inserted ready for quality checking.

The active area of the foil is divided into 20 sectors, 2 rows of 10 sectors, as shown in Figure 4.1 left. We accomplish the electrical test, sector by sector. The electrical connection on the foil is ensured by copper points mounted on PVC rods, clamped on bakelite supports which ensure the distribution of the weights in a uniform way.

We bring the voltage quickly up to a value of 550 V (1-500 V/s ramp-up) and check the leakage current. If the sector responds positively to electrical stress, no relevant current should be recorded but we should observe something ≤ 1 nA. We keep constant this voltage for 180 seconds in order to check the stability of the foil and to eliminate impurities adhering to the foil, which can be burned by the tension and evacuated by the gas flow. After 180 seconds, we bring down the voltage up to 450 V and keep it constant for another 180 seconds. The current should not change from that previously recorded value, or in any case remain under 1 nA. We repeat this procedure (or test), also called *"cleaning cycle"*, from a minimum of 3 times until the sector shows a stable current below 1 nA. As an example, we show in Figure 4.2 left column the full procedure on a single sector of a GEM foil (including additional cycles due to a small peak of current in the first part of the second cycle).

If during the test the leakage current constantly increases, there is a risk of electrical discharge conditions and damage, even irreversible, of the GEM foil, as shown in Figure 4.2 right column. In these cases the software is set for a safety operation which instantly interrupts the voltage supplied, switching off the electronic device, in order to safeguard the foil. If the current stay below 1 nA for the whole time at HV (180 s), the foil pass the quality check. Otherwise the test is repeated if there is a trend toward improvement. Vice versa we need to attempt a recovery of the bad sector (doing other cycles of check) or, in the worst cases, send back the foil to the manufacturer for repair.

So far we examined 85 GEM foils (1700 sectors) and the quality of the foils has proved to be high enough, in fact, only 6 foils (or better to say 8 bad sectors, 2 of which on the same foil) did not pass the quality test, therefore they have been excluded. For the

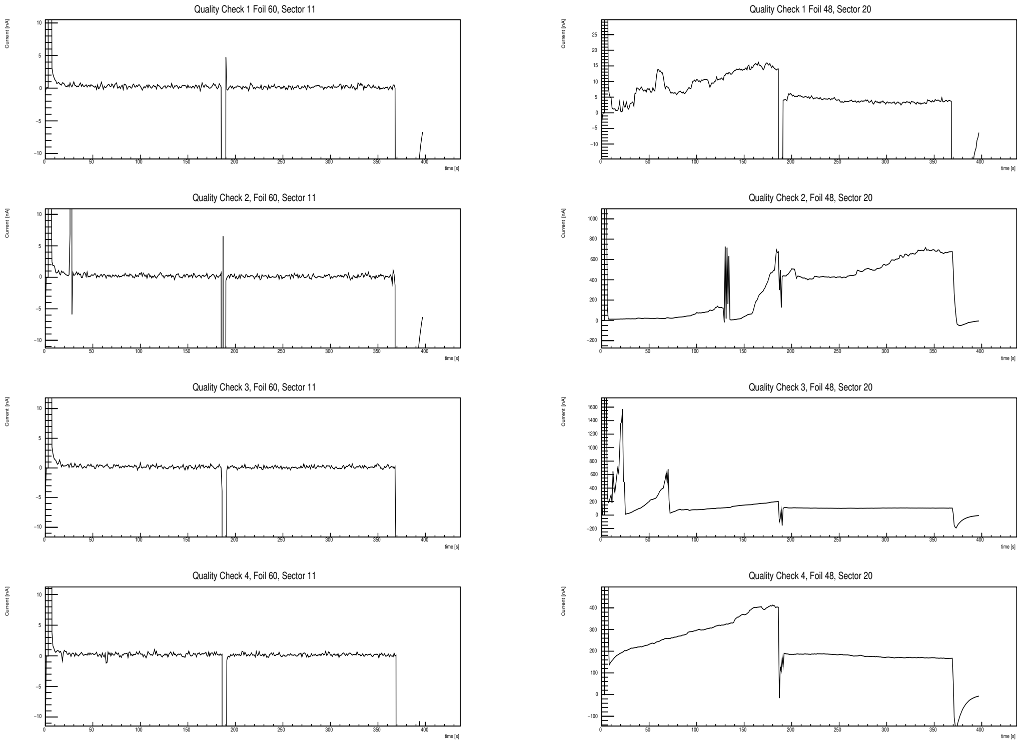

Figure 4.2: Left column: results of the quality check of a GEM foil performed in the clean room of the INFN Sezione di Catania. The graphs show the trend of the leakage current (nA) as a function of time (s). As an example, we show only the sector 11 of the foil n.60 where we can observe the current leakage on four cycle. We can note as the second check shows a current peak, around to 30 seconds, (probably caused by micro-particles burning blocked in the GEM holes). Doing supplementary checks (third and fourth cycle), according to protocol, the sector results cleaned. The voltage is brought down from 550 to 450 V after 180 seconds, as shown from negative variation of the current which is restored around zero in few seconds. Right column: Typical example of a quality check in a malfunctioning sector, where an excessive leakage current was recorded. The sector, even after several cleaning cycles, remained with a very high current leakage, and therefore the foil did not pass the electrical test.

remaining foils, i.e. 1580 sectors, the tests were performed regularly with current leakage recorded below 1 nA on average (unless small fluctuations due to measurement accuracy and environmental noise), as required by the protocol and shown in Figure 4.3.

4.2 Assembling and characterization of the GEM module

Once the electrical test has been successfully carried out, the foils are ready for assembling into a new GEM module.

The single GEM module, as previously written, consists of a stack of 3 foils generally separated by 2 mm of gas. This distance must be maintained within a few percent in order to keep the electrostatic fields sufficiently uniform and constant, avoiding spatial unevenness of the collected signal and naturally preventing the contact between the foils

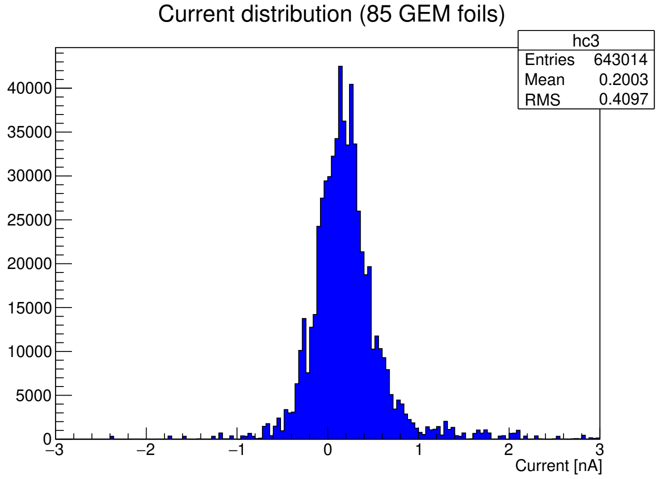

Figure 4.3: Leakage current distribution of the last cleaning cycles for each one of 1692 analyzed sectors (8 out of 1700 sectors showed irregularities, therefore excluded) under quality check test. Each entry represents a current measurement per second (± 380 seconds for each sector of 85 GEM foils). Plot shows an average distribution with peak below 1 nA, as required by protocol. The negative fluctuations are due to measurement resolution and environmental noise.

for prevent a short circuit. Therefore, in order to fulfill these requests, a mechanical "Stretcher" (*"Tendi-GEM"*) was designed and realized, inspired by the GEM modules construction for the muon station at LHCb [44].

The tendi-GEM (Figure 4.4 left) is based on force sensors (or *load cells*) that guarantee a correct traction on the different sides of the foil. Once correctly stretched out, the foils are stacked one over the other and isolated by 2 mm thick stesalite frames which include 300 μm thin spacers. The foils and frames are glued by non-conductive glue. Every operation for the assembling of a triple-GEM is accomplished step by step on the tendi-GEM, as shown in Figure 4.4 right (more info about the assembling of the GEM module in reference [33]).

Figure 4.4: Left: mechanical structure of the tendi-GEM inside the clean room of the INFN Sezione di Catania. Right: triple-GEM module assembled in its entirety, just removed from the tendi-GEM.

Once the assembly is completed at the INFN Catania, the GEM modules are sent to the Istituto Superiore di Sanità (ISS) in Rome for:

- gluing the external gas connectors,
- check gas tightness,
- installation and soldering of the HV divider,
- train HV,
- complete characterization using the X-ray irradiation facility (Figure 4.5).

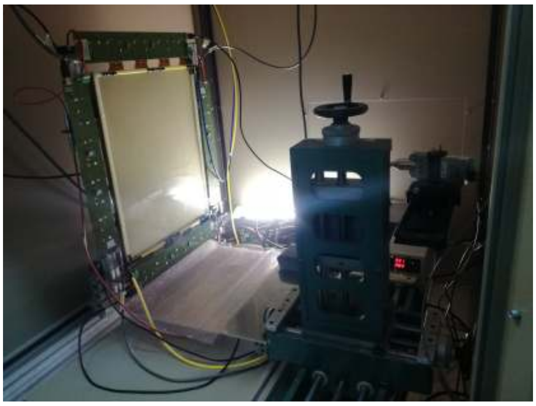

Figure 4.5: GEM module (left) within the X-ray chamber ready to test with source (right), at the Istituto Superiore di Sanità in Rome. Each module is irradiated by varying the distance of the source, the solid angle, the intensity and the HV of the X-rays.

A preliminary resistive control of the modules is performed (through an ohmmeter) to verify any short due to the assembly phase or shipping. Subsequently, once the external gas connectors and piping are installed, the module is connected to the gas line, initially Nitrogen, to check its gas tightness. The Nitrogen entering the detector comes out by a line that subsequently passes through a bubbler, containing paraffin oil, in order to verify the continuity of the flow. We test the gas tightness through measurements of pressure entering and exiting the module as a function of the Nitrogen flow supplied and rate of the bubbler observed. According to measurements on the first modules, after careful check of significant gas loss by a gas sniffer, the estimated bubbling rate for an acceptable module is around 1 Hz when the gas flow is 70 $\pm$ 30 $ccpm$ and the pressure is 0.07 $\pm$ 0.03 $mbar$, as shown in Figure 4.6. If the beginning of the bubbling is observed for pressure and gas flow measurements much higher than the reference range, then the module probably shows any gas leak, and therefore must be checked further.

Once the gas tightness has been verified and the HV divider has been connected and soldered to the HV foils terminals, the HV training is carried out in Nitrogen gas, in order to check the stability of the currents and eliminate/burn any impurities still present inside the modules. The voltage is applied gradually with a ramp-up of 100 V/s up to the

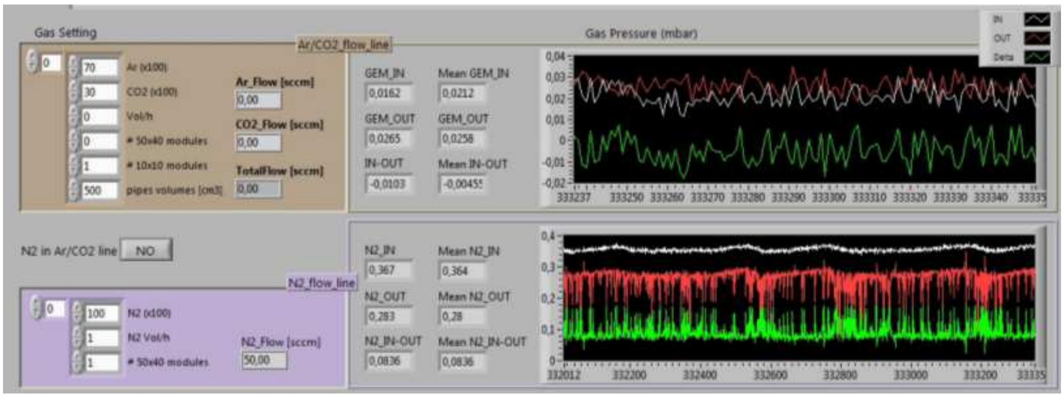

Figure 4.6: Monitoring of the pressure and flow of gas supplied to the GEM module. The upper side is dedicated to monitoring the Ar/CO_2 mixture, while the lower side is for Nitrogen. In this case, the Nitrogen monitoring is shown during the gas tightness control phase, where the white, green and red line represents the IN pressure, the OUT pressure and the pressure difference (IN-OUT) respectively. The figure shows a fairly jagged output pressure due to continuous bubbling, with 50 $ccpm$ of gas flow and 0.08 $mbar$ of pressure variation.

value of 4200 V, with step of 1000 V. In a stable module, the current recorded on the HV divider must remain constant (within $< 2\ \mu A$ respect to the baseline) over time according to the applied voltage; for each HV setting to current shall have a corresponding value, within few μA (variation is mainly related to the HV divider resistors), as shown in Table 4.1.

Voltage $[V]$	Max Current $\pm$ 500 $[nA]$
1000	25000
2000	51000
3000	77000
4000	103000
4200	107000

Table 4.1: The table shows the correspondence of the nominal current recorded on the HV divider as a function of the high voltage applied to the GEM chambers (reference currents scale). The current shown in the table is the maximum current to be observed but it may vary up to $\pm$ 500 nA depending on the divider used.

Should a leakage current occur beyond the tolerance of reference scale, the system goes in a safety condition and turn off the high voltage on the GEM chambers, so as to preserve the detectors. If the check is not successful, due to excessive leakage of current and therefore possible short-circuit problems, we need to identify the problematic area of the module, in other words to identify the corresponding sector and isolate it. The sector is isolated by removing the resistor placed outside the module, as shown in the Figure 4.7 right. The shorted sector is identified by thermo-camera, looking at the corresponding protective resistor that heats up when the two sides of the GEM foil are biased by few tens of volts, becoming visible on the display as a small spot, as shown in the Figure 4.7 left. Therefore, we can easily identify the sector to be isolated.

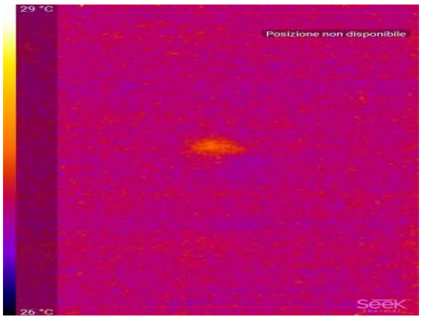

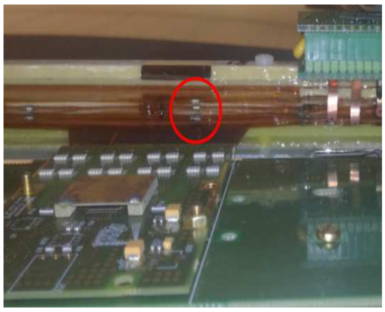

Figure 4.7: Left: visualization through a thermo-camera of a heated electric resistor (3 mm), when the corresponding sector is shorted with the opposite site of the GEM foil. Right: protection resistors (red circle) in the HV line of corresponding sector.

Once the gas tightness and currents stability checks have been completed, we switched the Nitrogen with the Ar/CO_2 mixture (70/30%), in order to perform the X-ray test. The X-ray facility consists of a portable collimated X-ray tube [45] mounted on a movable support that can span the entire GEM module active area, from a distance of few mm to about 1 m and any incidence polar angle. The GEMs under test and the X-ray tube are contained inside a box of Pb walls for radiological protection. The characterization is performed by varying the X-ray source distance from the module (can determine the number of incident X-ray photons), its intensity (tuning the current from 5 up to 30 μA), its high voltage which define the energy distribution of the X-ray (in the range of 5 to 20 KeV) and finally the angular opening of the beam. The variation of the solid angle allows us to probe both the entire active area but also relatively small parts of the module (by inserting a collimator with different size), such as observing the behavior of a single sector or the edge effects.

We used a small full DAQ system (MPDs and front-end cards on modules) with a random trigger and a voltage applied to detectors of 3800 V when irradiated by X-ray.

To analyze the test data, we implemented a relatively simple 1D and 2D clustering analysis: on each axis we search for contiguous strips with signal above the noise level (measured as RMS of the pedestal, as shown in Figure 4.8 for example); such contiguous strips form a 1D cluster. 1D-x and 1D-y clusters, having the same charge (± 30%), form a 2D cluster.

Figure 4.9 shows the typical charge distribution on 1D clusters and charge sharing (*"Charge Correlation"*) between x and y 1D clusters. Since the x and y strips collect about the same amount of electrons coming from the avalanche, then we expect a charge correlation represented by a distribution lying on the main diagonal. Similarly, the *"Relative Difference"* or *"Charge Asymmetry"* of the charge on the axes must show a value around 0. In fact, for all the characterized modules with X-rays, the results obtained on average show the trends sought, as shown in Figure 4.11 left.

Figure 4.10 shows the distributions of the number of strips inside a cluster at 3800

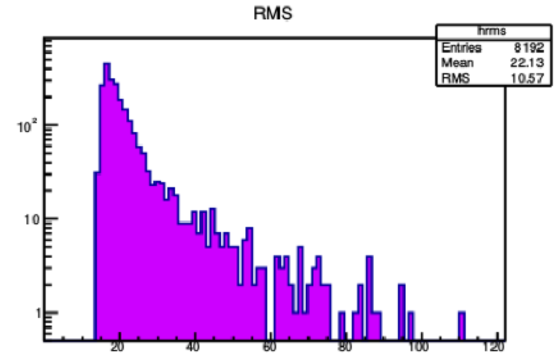

Figure 4.8: Example of a distribution of pedestal charge of a X-ray test at ISS of Rome. An average charge of around 22 ADC units.

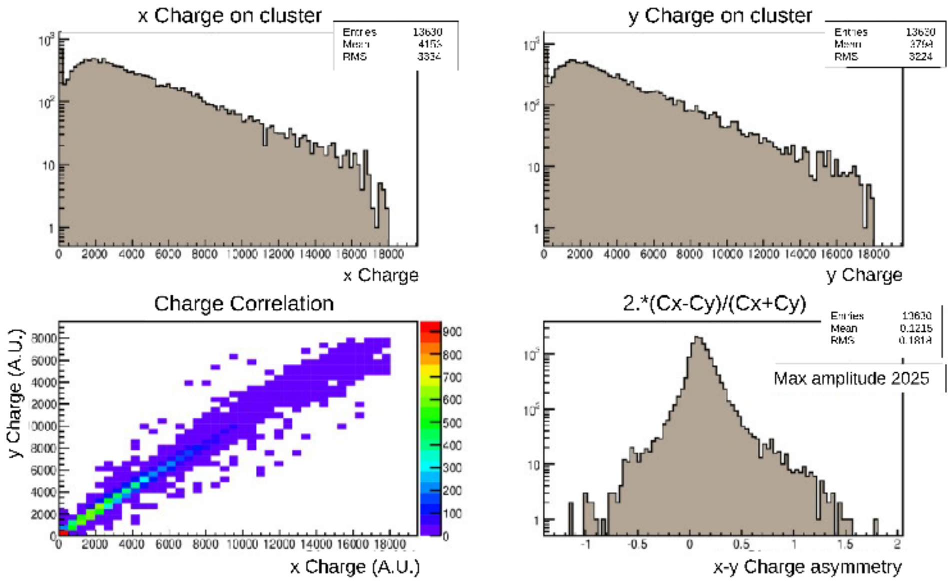

Figure 4.9: Top left and right: charge collection for each cluster (no cuts) at 3800 V, on axes, x and y respectively. Bottom left and right the correlation scatter plot and relative difference between the charge collected on axes, x and y respectively. If the distribution of the charges on the axes is almost the same, then the scatter plot must show the distribution along the bisector, while charge asymmetry must show a peak around 0 [32].

V, called *"Strips in Cluster"*, both on x and y axis. Considering the electron cloud that arrives on the read-out plane has the transverse size about 500 μm, while the read-out strips are 400 μm wide, we expect that a cluster is formed by one or two strips for single axis, on average. In fact, from the Figure 4.10, we can note that the distribution of the strips underline an average value around 1.4 and 1.6 on x and y axis, respectively. This type of result was recorded, on average, for all the modules analyzed, as shown in Figure 4.11 right. Actually, the number of strips involved could increase (three or four strips on average) as a function of the ionizing particle energy.

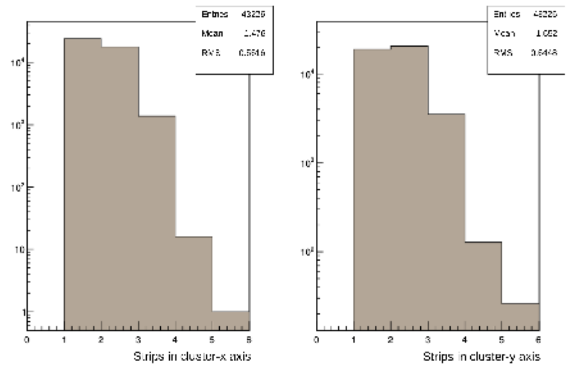

Figure 4.10: Number of strips inside a 1D cluster at 3800 V both on x and y axis. On average, the number of involved strips is between 1 and 2 [32].

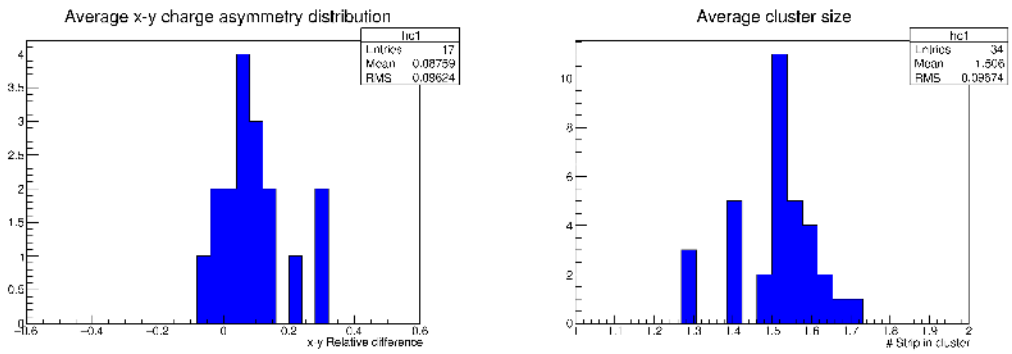

Figure 4.11: Left: average relative difference distribution (or average x-y charge asymmetry distribution) for the modules tested with X-rays at 3800 V. Since the charge collected on the x and y strips are about the same, then the distribution must show a peak around the value 0. Right: average distribution of the x-y strips within a cluster for the modules tested with X-rays at 3800 V. Considering the electron cloud that arrives on the read-out plane, a cluster is formed on average by one or two strips for single axis. The number of strips involved could increase as function of the voltage applied.

Finally, the Figure 4.12 shows the position of the clusters within the active area of the GEM module; this analysis, called *"Cluster Position"* or *"Hit Map"*, is of fundamental importance as it allows us to observe if there are inefficient sectors when the X-ray beam hits the module, if there are high-voltage lines interrupted or if there are damaged/broken strips (visible as a white strip inside the Hit Map plot, as shown in Figure 4.12 right). When a sector is in permanent short-circuit, we are forced, in order to keep the other sectors at the desired voltage, to isolate it through the removal of the resistor, as mentioned above 4.2. Therefore, the sector appears as a white rectangle inside the Cluster Position, since, obviously, no cluster is formed, as shown in Figure 4.12 right. From the Figure 4.12 left we can see how the sectors respond correctly to the passage of

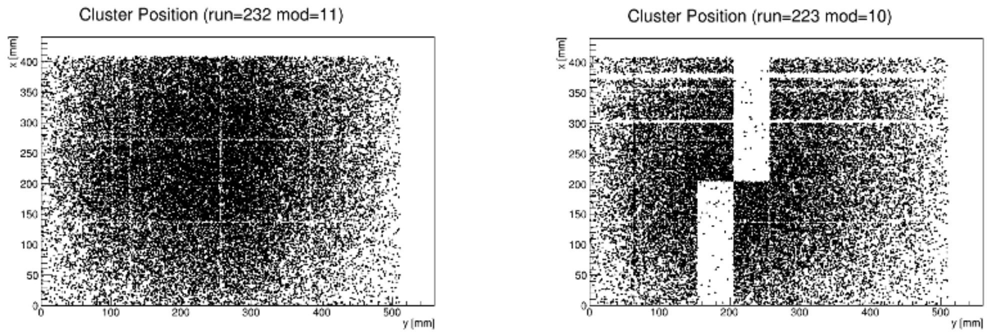

Figure 4.12: Left: the plot shows the position of clusters within the active area of the single triple-GEM module, where all sectors respond correctly [32]. Right: cluster position of a module with 2 bad sectors, visible as white rectangles. In addition, some inoperative strips (horizontal white strips) are visible in the upper side of the module. A module with these characteristics is still within the approval limits or otherwise considered as a spare module.

the particles (the clusters are visible on the entire active surface of the module). Only in the low side there is a slight inefficiency in cluster formation, but this is due exclusively to the angular opening of the beam (not perfectly centered). The spacers between the GEM foils are visible as tiny dead segments, especially in the central part of the module.

We reject or rework (whenever possible) a module if the map shows evident inefficient rectangular sectors. We tolerate up to two defective sectors out of 60 after reworking (the module is rejected with three or more bad sectors); this corresponds to a maximum hit geometrical inefficiency of 10% and an overall tracking efficiency better than 95%, with 4 over 6 fired layers [32].

The modules that pass the X-ray characterization are sent to JLab. Up to now, we assembled and tested 25 GEM detector modules; we rejected two of them for evident damage during the production process. We tested in Italy and then delivered to JLab 19 of them.

4.3 GEM chamber integration

Once the modules are at JLab, we re-checked, in an ad-hoc test station, the tested and shipped GEM modules from Italy through a low-activity ^{90}Sr [1] radioactive small source to verify that packaging and overseas transportation did not damage the modules. The test station was set up within a "reasonable" clean room at JLab. In addition to checking each single GEM module, this station allows to test and tune the front-end electronics connected to the module. Figure 4.13 shows the single test station with a GEM module inserted. The modules that pass the re-check will be assembled into the GEM chambers for the SBS/BB front tracker.

Figure 4.13: GEM module inside the single GEM station, connected to the front-end electronics and ready for re-check.

Four front tracker GEM chambers, called *J0, J1, J2* and *J3* in chronological order of assembly, have been assembled and prepared for the final characterization through cosmic rays test (the fifth chamber, $J4$, is currently in assembly phase and test). We assembled these chambers (see Figure 4.14) between July 2017 and July 2018, while the chamber $J4$ in September 2019; we expect to complete the GEM front tracker by the spring of 2020.

4.4 Cosmic rays characterization

The assembled chambers lay on the shelves of a large multi-shelf rack, in sandwich between two planes of scintillators, as shown in Figure 4.15 left. The upper scintillator plane consists of three bars (about 160 cm) that cover the entire active area of the GEM chamber, while the lower plane is formed by five long scintillators (about 190 cm), covering an area slightly larger than the upper plane; each scintillator side is coupled to one PMT. The PMT signals are discriminated and then ORs of the upper and lower PMTs are ANDed to form the cosmic trigger.

Before starting the cosmic rays test, to verify that cabling is properly connected, electronics correctly plugged and functional, two main checks are performed before ramping

[1] Strontium-90 undergoes beta decay, emitting electrons with energy 0.546 MeV with a half-life of 28.8 years.

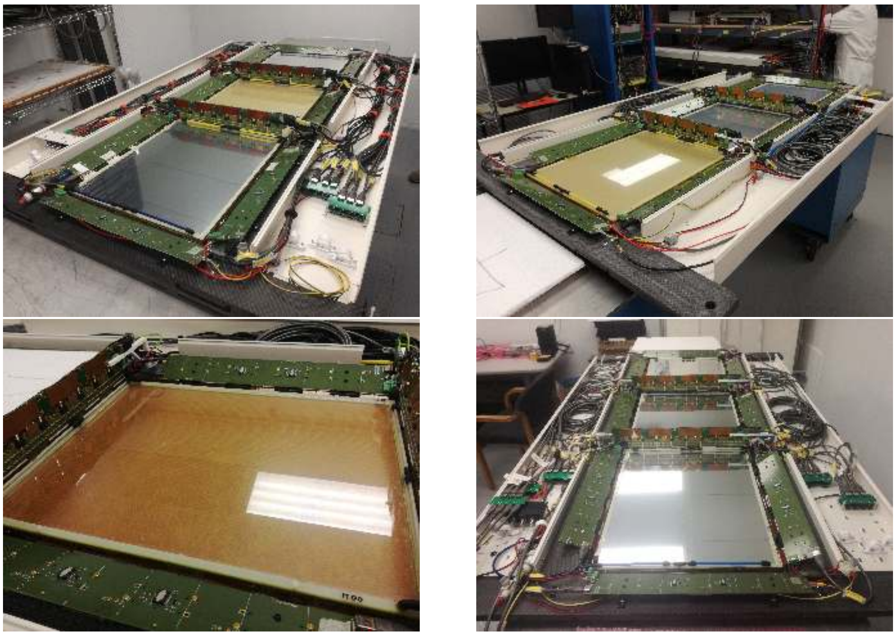

Figure 4.14: Figure shows 4 GEM chambers assembled at JLab between July 2017 and July 2018. Top left and right: GEM chamber J0 and J1, respectively. Bottom left and right: GEM chamber J2 (detail of the central module) and J3, respectively.

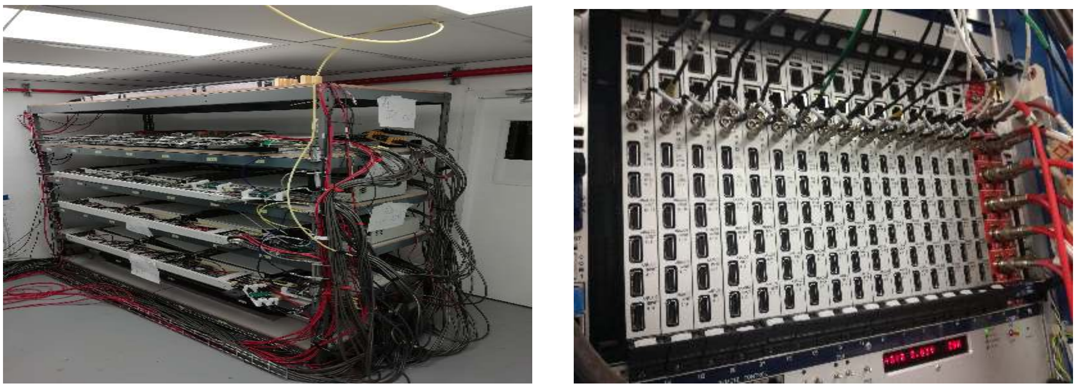

Figure 4.15: Left: cosmic test stand at JLab. Each shelf of the rack houses a GEM chamber regularly connected to the acquisition electronics. In the top and bottom side of the rack there are the scintillators that form the trigger system of the apparatus. Right: 16 MPDs (white devices) with LEMO connectors inserted for the trigger system and 2 High Voltage modules (red devices), inside of the cosmic rays data acquisition rack.

up the HV on the chamber modules:

1. Histogram test;
2. Pedestal analysis.

On histogram test 1 we check the connection of the front-end cards (except the trigger line) and the proper configuration of them through the observation of cards histograms, as shown in Figure 4.16 for example. Each histogram represents the distribution of the signal in input to the ADC (located on the MPD), where the analog signal of the APV25 card arrives, in "free running" condition (no trigger). When there is no data to read out, we observe the output of the chip at the logic 0 level (or noise), corresponding to the group of peaks below about 500 ADC units and a peak at around 3000 ADC units which corresponds to the synchronization pulse (or tick mark) that the APV sends every 35 clock cycles in 40 Mhz mode to keep the electronics synchronized, when there is no data for a considerable time [46]. When a card is disconnected, the distribution is at zero voltage at half ADC scale (around 2000 ADC units). Figure 4.16 shows the histograms of 15 cards allocated on 3 backplanes (5 cards represented by same color for each backplane). All histograms show a distribution in line with our expectations, that is according to the operation way of the APV25 chip. These results show the correct connection of 15 front-end cards to DAQ electronics.

Once the cards are correctly connected, we carry out the checks on the pedestals 2 of each single APV channel, so as to observe if there are excessively noisy cards to cause problems in the subsequent off-line analysis. In the case of noisy cards, we consider their replacement. Figure 4.17 shows the pedestals of a single GEM chamber, where 54 distributions (18 cards for 3 modules) of charge in ADC units on the 128 channels can be observed. These pedestals show satisfactory charge distribution, except for a very noisy card (ID 5.1) and a card (ID 6.1) probably unplugged on the GEM module connectors; in the first case the card was replaced, while in the second case the card was re-plugged correctly. According to these charge distribution plots, the cards show a reasonable pedestal without particular level of criticality, and therefore the control can be considered satisfying.

While testing the electronics, the GEM modules are flushed by Nitrogen to keep low the internal humidity [2] and possibly avoid contaminants from outside. The humidity can possibly be one of the cause of discharge in the GEM. Once the electronics are responding properly, and after Nitrogen gas has flushed for at least 2 days [3], we start ramping up the HV, in order to re-check the stability of the currents. The HV is applied gradually (ramp-up of 50 V/s) up to the target voltage (4100 V or so), with step of 1000 V, in a time of about 20 minutes, in order to condition the internal environment of the detectors. As already mentioned above, the current recorded must follow the same trend shown in the Table 4.1.

[2]The JLab shows a very humid external environment, where up to 95% values are reached in the summer, as shown in Newport News weather history 2019 [47].

[3]Originally we let gas flow for less than one day and this could be a possible cause of shorted sectors we experience on 4 GEM modules at JLab

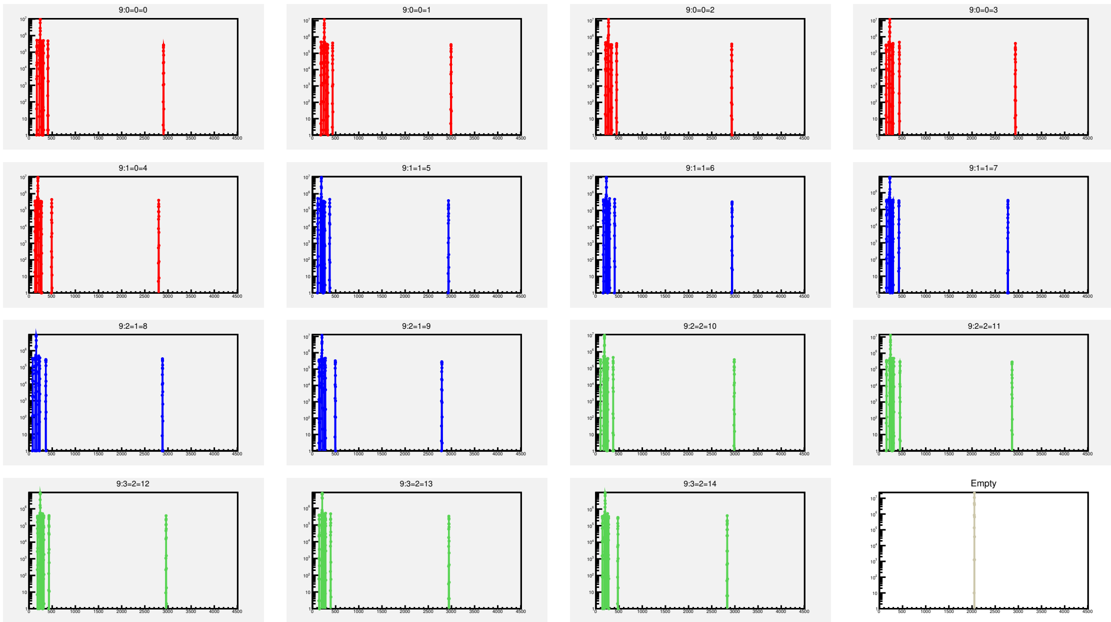

Figure 4.16: Figure shows the histograms of 15 APV cards correctly connected to DAQ electronics, in free running condition. Each histogram shows a pair of peaks; the first (below 500 ADC units) indicates the output of the chip at the logic level 0, while the second peak (around 3000 ADC units) corresponds to the tick mark to keep the electronics synchronized. Each color identifies a group of cards allocated on a single backplane, therefore the figure shows 5 cards on 3 backplanes.

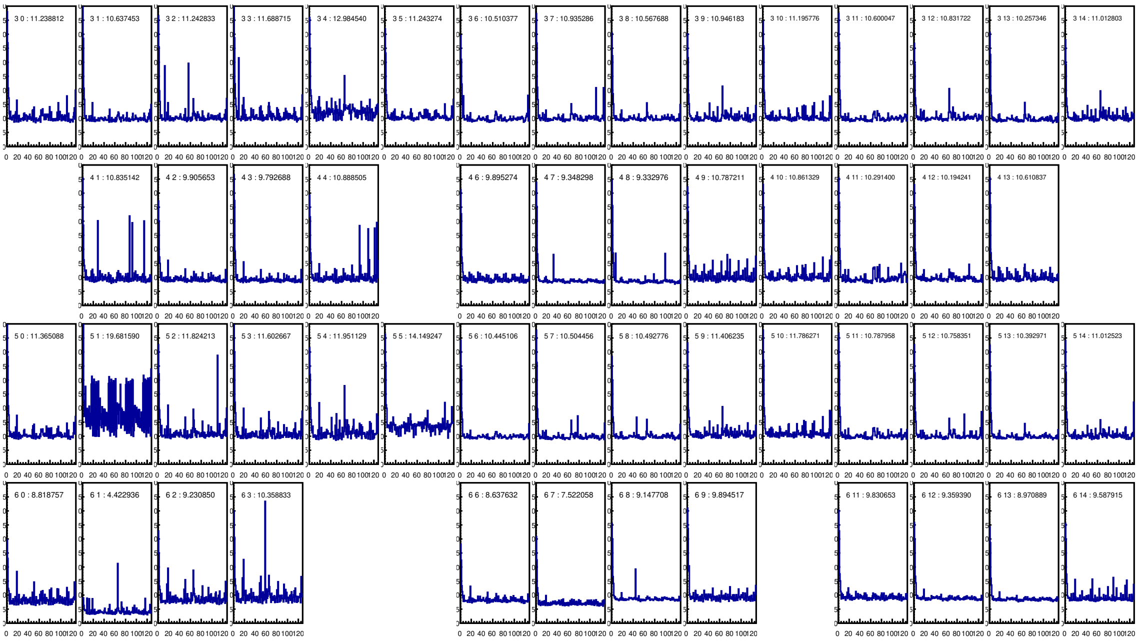

Figure 4.17: 54 pedestals of a GEM chamber. Each histogram shows the charge distribution on 128 channels of a single APV card. These results show on average a distribution with quite low charge counts, except for the ID 5.1 (very noisy) and ID 6.1 (probably badly connected).

Figure 4.18 shows the current trend (nA) as function of time (hours) of a single module; to the left the current ramp-up up to 4200 V is shown, while to the right a particular of the same current trend is shown, when the voltage is already at 4200 V, for a time of 5 hours, where we can also notice the smallest current variation on the high voltage divider. Figure 4.19 shows the currents distribution for all modules operating in the four chambers, at 4200 V over a period of 11 hours. The distributions show a peak around 106500 nA, in line with the reference scale and with our expectations. Actually, during the assembly and test phases, we observed some short-circuit problem on different GEM modules and therefore we have been forced to isolate some sectors.

As soon as the control tests completed, we performed the cosmic ray tests (April 2019) supplying different high voltages to GEM chambers (from 3800 V to 4100 V), holding constant the Ar/CO_2 gas flow ($\sim$ 1 Volume/hour for each chamber) delivered inside the modules (negligible dependence on the gas flow as regards gain or cluster formation over 0.5 V/h, more info in the reference [33]). Furthermore, we have done a course alignment of the chambers within a modest margin of error (order of cm), in such a way as to evaluate the efficiency of each GEM module and of the overall tracker-system.

Below we show the results regarding the characterization of GEM chambers through cosmic rays; first we observe the *Cluster Charge Sharing* for all the modules used, then the *Cluster Position* and the *Hit Efficiency* at 3800 V, 4000 V, 4100 V, and finally, we show a comparison between the *Tracking Efficiency* according to the three voltages used.

The *Hit Efficiency* represents the efficiency of single GEM module in detecting a hit

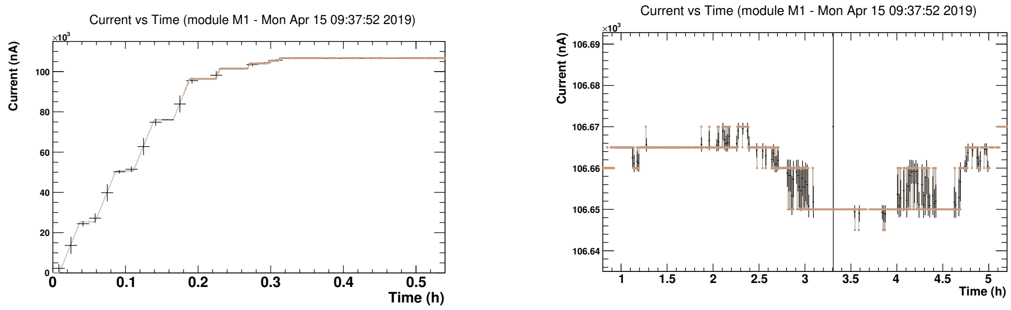

Figure 4.18: Current trend of a GEM module during HV monitoring test. Left: the ramp-up of the current up to the voltage of 4200 V. Right: current trend as a function of time at 4200 V (during a period of 5 hours).

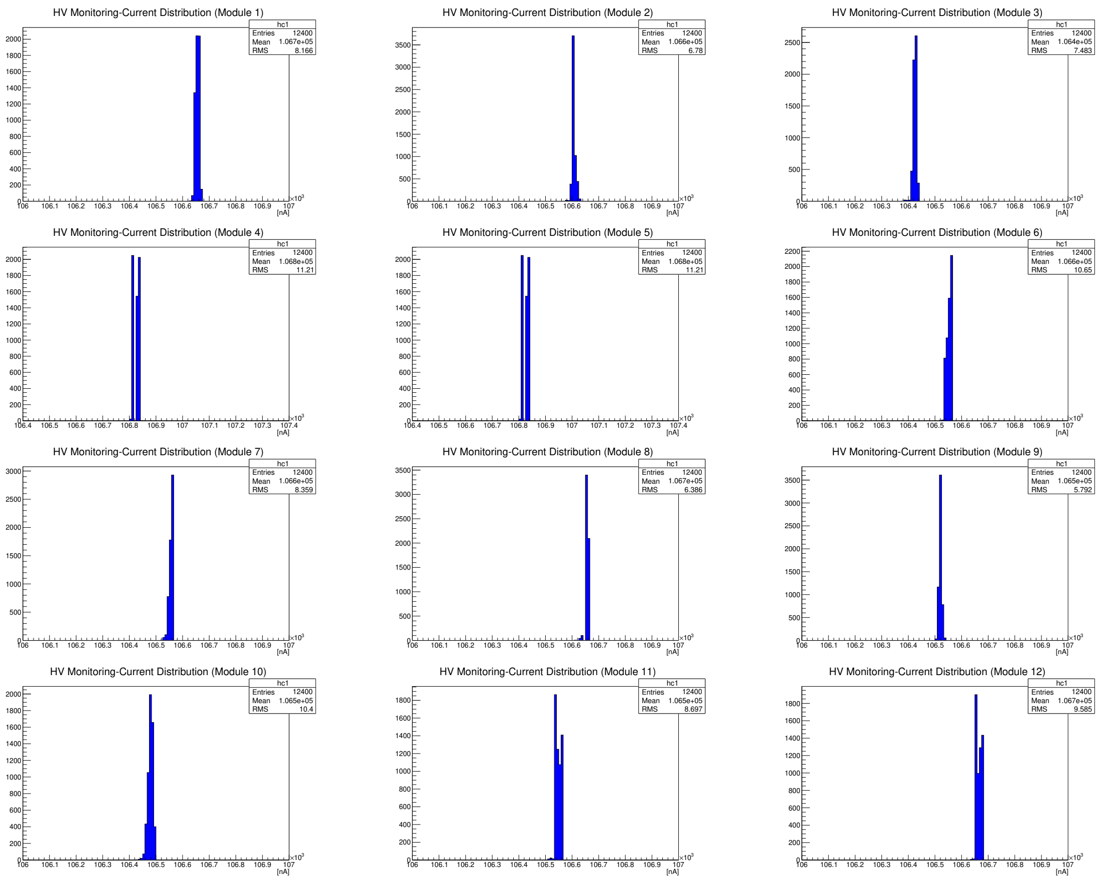

Figure 4.19: Figure shows the currents distribution for all modules operating in the tracker system, at 4200 V over a period of 11 hours. The distributions show a peak around 106500 nA, in line with the reference scale (Table 4.1).

when a cosmic ray passes through the tracking system; the hit efficiency is evaluated by the following method:

- a potential cosmic particle triggers the system and pass through the four GEM layers;
- use 3 chambers as reference and the 4^{th} to be analyzed;
- select all events that produce 1 hits on each reference;
- for each selected event: do a linear fit on the 3 points (hits) of the reference chambers; the fit represent the cosmic track;
- estimate the impact point of the above track on the 4^{th} chambers;
- count 1 if the 4^{th} chamber has an hit within 5 cm from the estimated impact point; 0 otherwise;
- the efficiency on a given region of the chamber is the counts divided by the number of selected events with impact points in the region;
- finally, we repeated this procedure for each GEM chamber.

The *Tracking Efficiency* represents the overall efficiency of the whole system in being able to reconstruct a track, taking into account the hit efficiency of the single GEM chamber. The tracking efficiency is estimated by the following procedure:

- simulate a track direction and impact point;
- estimate the crossing point on each chamber;
- for each crossing point extract a uniformly random value between 0 and 1; if smaller than the hit efficiency in the given region the point corresponds to a hit;
- if at least 3 hits have fired out of 4 chambers, assume the track can be reconstructed;
- the ratio of the reconstructed track to the total simulated track provide the tracking efficiency.

The methodology for estimating GEM chambers efficiencies is currently a work in progress and quite preliminary, consequently the results will also be preliminary.

Figure 4.20 shows the x-y cluster charge sharing for each module used in the GEM chambers. The correlation observed is quite satisfactory since a distribution along the bisector of the plots is clearly visible (except for module 0, which shows a slight deviation from the bisector), therefore these results show that the charges are equally divided along the x-y strips of the readout, according to our expectations.

Figure 4.21 shows the cluster position (top) and the hit efficiency (bottom) at 3800 V of each GEM chamber. The cluster position plot shows the hit map when cosmic rays

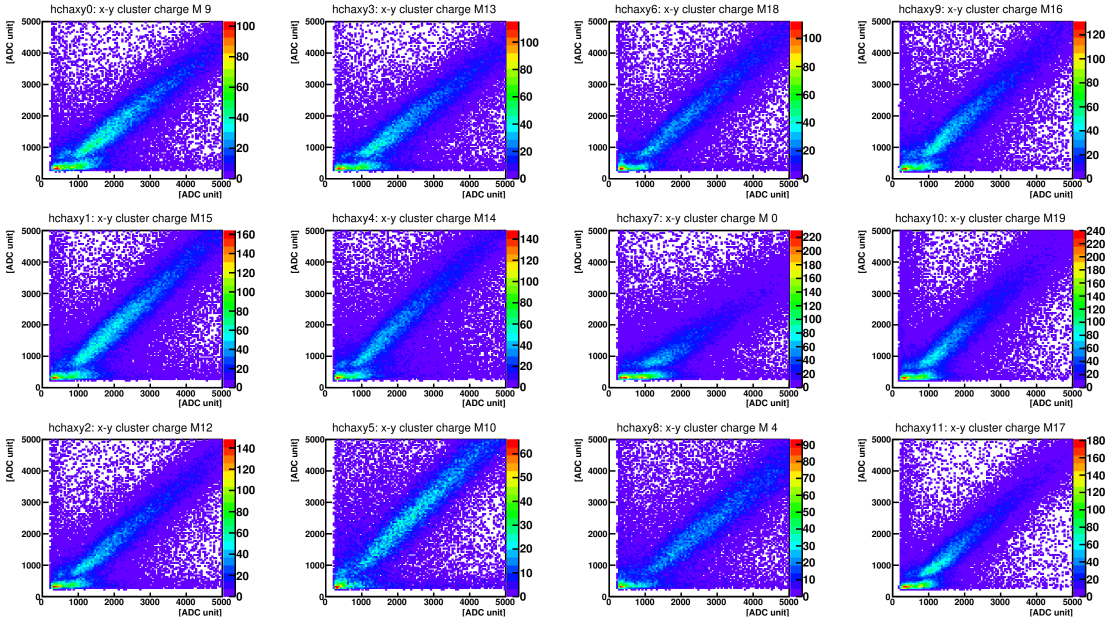

Figure 4.20: X-y cluster charge sharing for each module used in the chambers. The correlation shows a distribution along the bisector of the plots (except for module 0, slight out from the bisector).

pass through a GEM chamber, therefore each black point represents one hit identified within the active area of the detector. Thanks to this analysis we can observe the general state of each chamber and the problems related to its operation. From this mapping, we can observe some white rectangles (in addition to some inefficient strips in J1) that correspond to the shorted, deactivated sectors. Moreover, we can also note a low efficiency of the chambers due to the applied voltage not high enough to allow an optimal gain for cluster formation. The same effect is also confirmed in the local hit efficiency where we can observe a low identification percentage of the hits. These results show that the applied voltage of 3800 V is not sufficient for the formation of clusters (or hits) and consequently the hit efficiency is very low in all GEM chambers, according to our expectations. Figure 4.22 shows the cluster position (top) and the hit efficiency (bottom) at 4000 V of each GEM chamber. In this case the hit map and the hit efficiency are quite satisfying (except for a slight inefficiency in the high and low edges of the chambers due to the trigger system acceptance), since the applied voltage is sufficiently high to allow a good gain, that is a good formation of clusters, according to our expectations. The two inefficient central bands represent the separation zones of the 3 GEM modules, where the vertical backplanes are positioned (dead area of the GEM chamber).

Figure 4.23 shows the cluster position (top) and the hit efficiency (bottom) at 4100 V of each GEM chamber. In this last case, the graphs show satisfactory results both cluster position and hit efficiency (except always for the inactive sectors). The applied voltage allows the maximum performance of the detectors, without risking problems of electric discharges, according to our expectations.

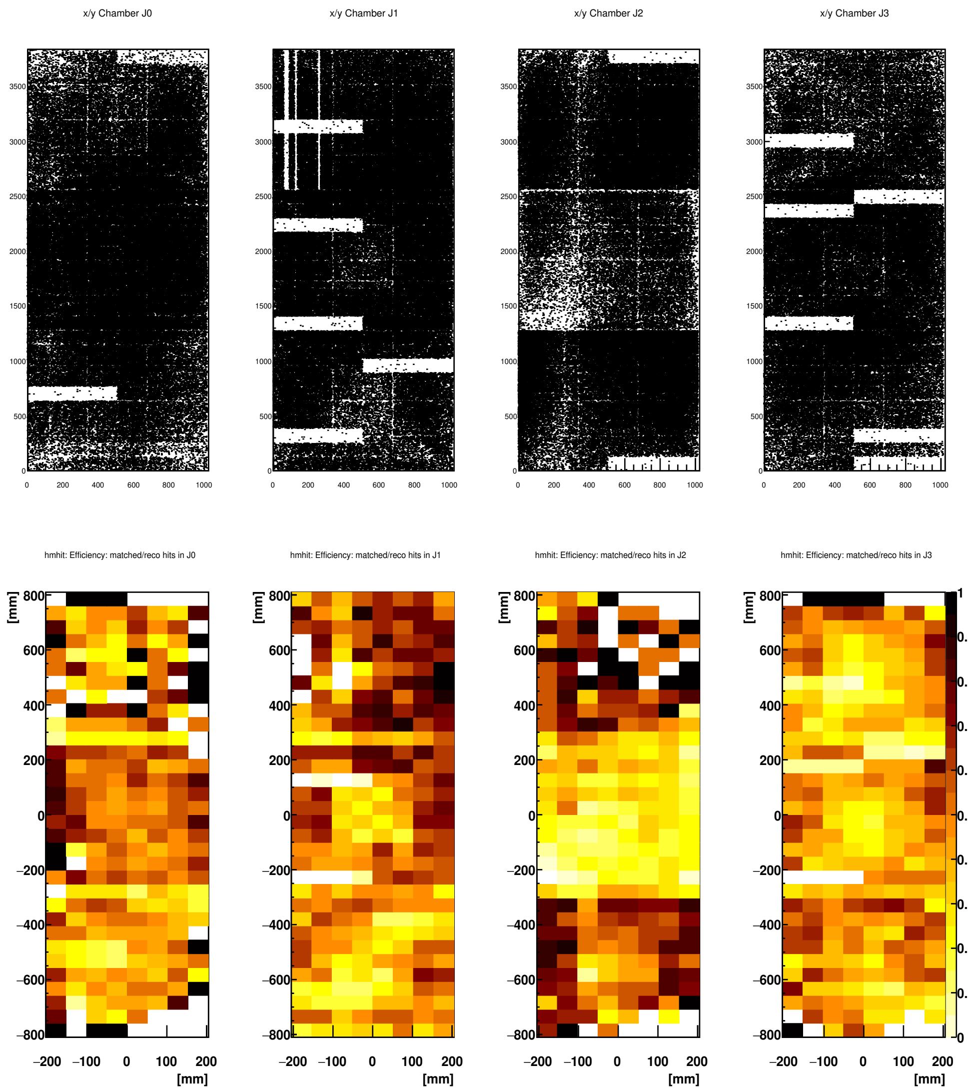

Figure 4.21: Cosmic rays test at 3800 V at JLab. Top: clusters position or hit map of the four GEM chambers. Some deactivated sectors are visible in the system, as they are in a short-circuit state. Furthermore, a overall inefficiency of the chambers is shown, due to the insufficiently high voltage for good cluster formation. Bottom: hit efficiency of the four GEM chambers. The figure shows a low efficiency, due to the high voltage applied, which is too low for the formation of the clusters.

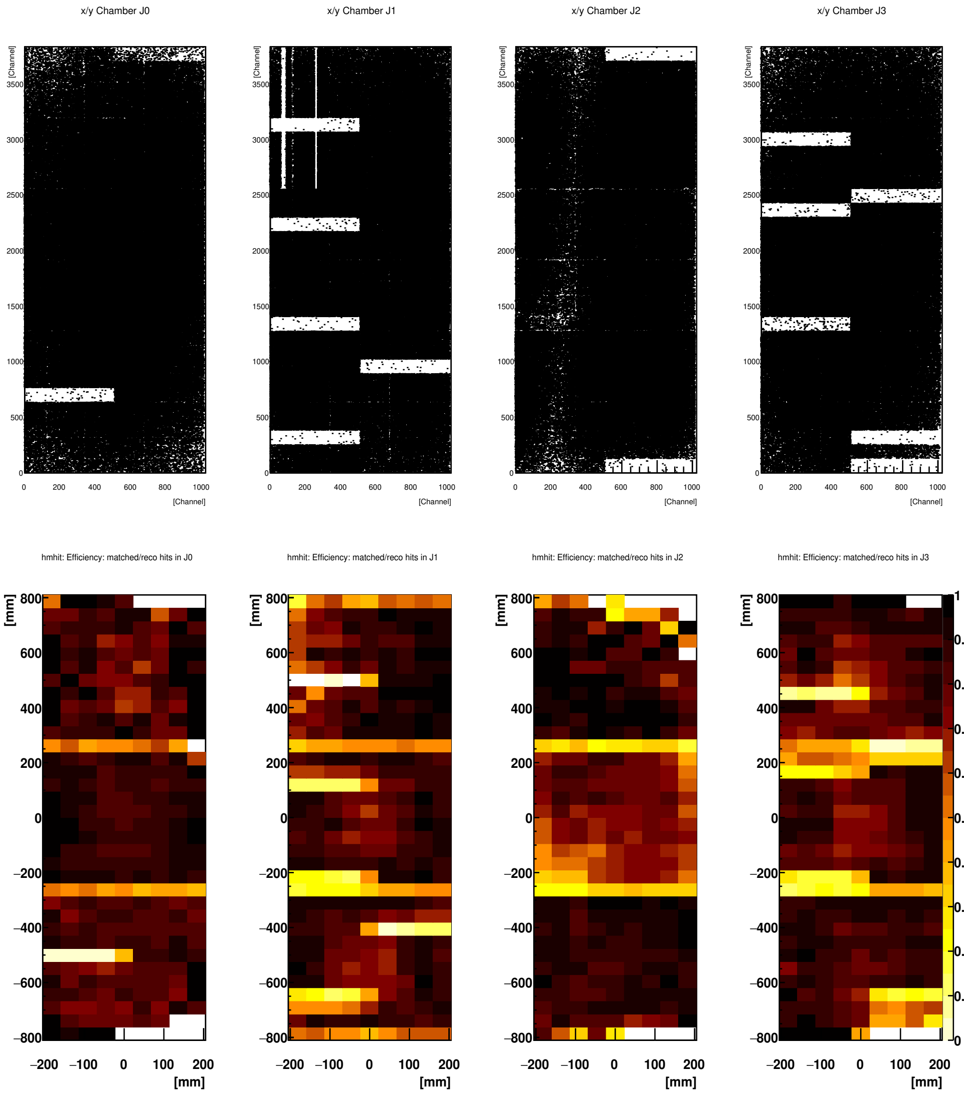

Figure 4.22: Cosmic rays test at 4000 V at JLab. Top: cluster position or hit map of the four GEM chambers. Some deactivated sectors are visible in the system, as they are in a short-circuit state. A satisfying hit map is shown since the applied voltage is sufficiently high to allow the formation of clusters. Bottom: figure shows a moderate hit efficiency since a reasonable high voltage is applied, but some inefficiency are noticed, such as the deactivated sectors and the two separation zones of the 3 GEM modules (dead area of the detector because there are the vertical backplanes positioned).

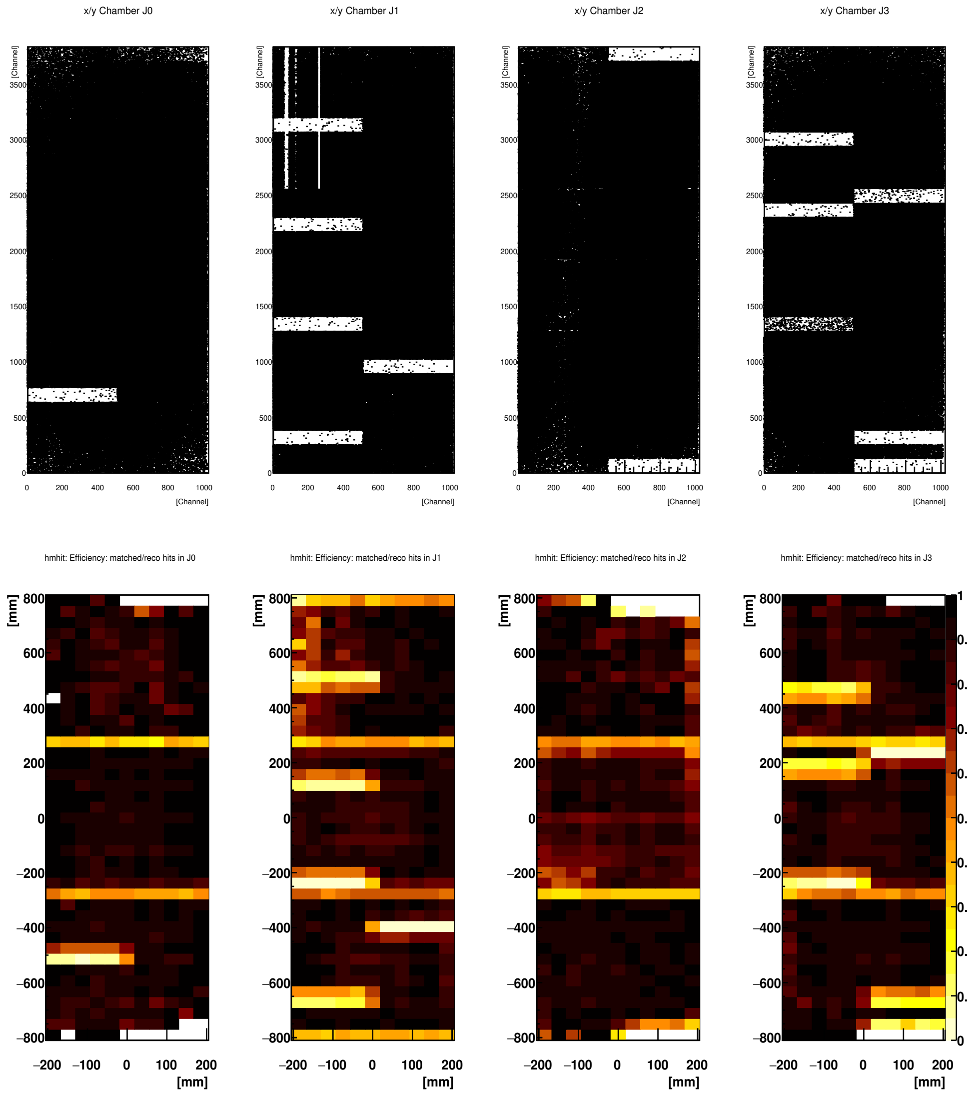

Figure 4.23: Cosmic rays test at 4100 V at JLab. Top: cluster position or hit map of the four GEM chambers. Some deactivated sectors are visible in the system, as they are in a short-circuit state. A good hit map is shown since the applied voltage is high enough to allow a more than good formation of clusters. Bottom: figure shows a good hit efficiency since a reasonable high voltage is applied, except for the inactive sectors and the dead zone of the detector (central yellow bands).

Finally, the Figure 4.24 top shows a comparison of tracking efficiencies as function of the applied voltage; The efficiency increases with increasing voltage, confirming the results of the cluster position and the hit efficiency (closely linked). Furthermore, we can observe in the Figure 4.24 bottom (Track Efficiency distribution - 4100 Volt) how the tracking efficiency of the GEM system is over 90% at 4100 V in spite of some inactive sectors. The fairly satisfactory tracking can be improved by replacing and rearranging the low efficient GEM modules.

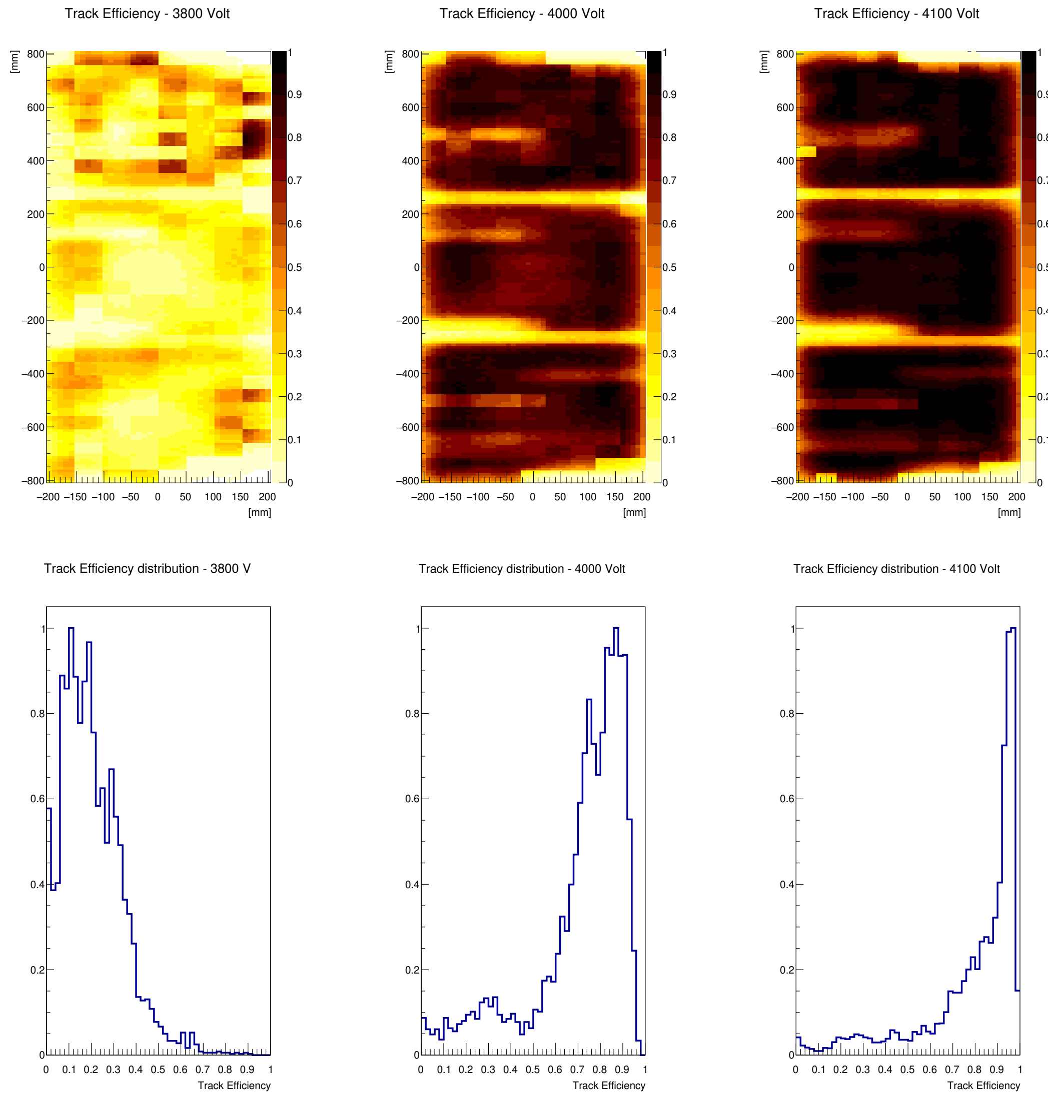

Figure 4.24: Top: comparison of tracking efficiencies as a function of the applied voltage at 3800, 4000 and 4100 V. The tracking efficiency increases with increasing voltage, confirming the results of the cluster position and the local hit efficiency. Bottom: Tracking efficiency distribution of the GEM chambers system as a function of voltage. The efficiency distribution achieve over 90% at 4100 V.

After a break of one month (GEM chambers switched off), we re-checked the four GEM detectors, but unfortunately, probably due to the humidity still present inside the modules, a couple of sectors have short-circuited even at relatively low voltage (1000 V), during the HV ramp-up, causing the isolation of the sectors. The removal of 2 other sectors has brought down the geometric efficiency under 93% (223 active sectors out of 240 as total), certainly beyond the lower limit of acceptability.

This accident clearly confirms the need of a continuous Nitrogen flushing event when the chambers are not in operation, in order to always keep the humidity level and the risk of short-circuits low. Between August and September 2019, we replaced the two worst modules (Figure 4.25) and moved, where possible, the less-efficient modules to edge of the chambers, so as to position as many inactive sectors as possible outside magnetic spectrometer acceptance [12], as shown in Figure 4.26). In this way, we improve the geometric efficiency and consequently the tracking efficiency. In fact, according to the new arrangement of the modules, the geometric efficiency increased up to 95% (228 active sectors out of 240 as total) and if we consider the magnetic spectrometer acceptance, then excluding the sectors in the high and low edges of the chambers, the geometric efficiency could rise up to around 97%. The slight inefficiency in cluster formation is due to the

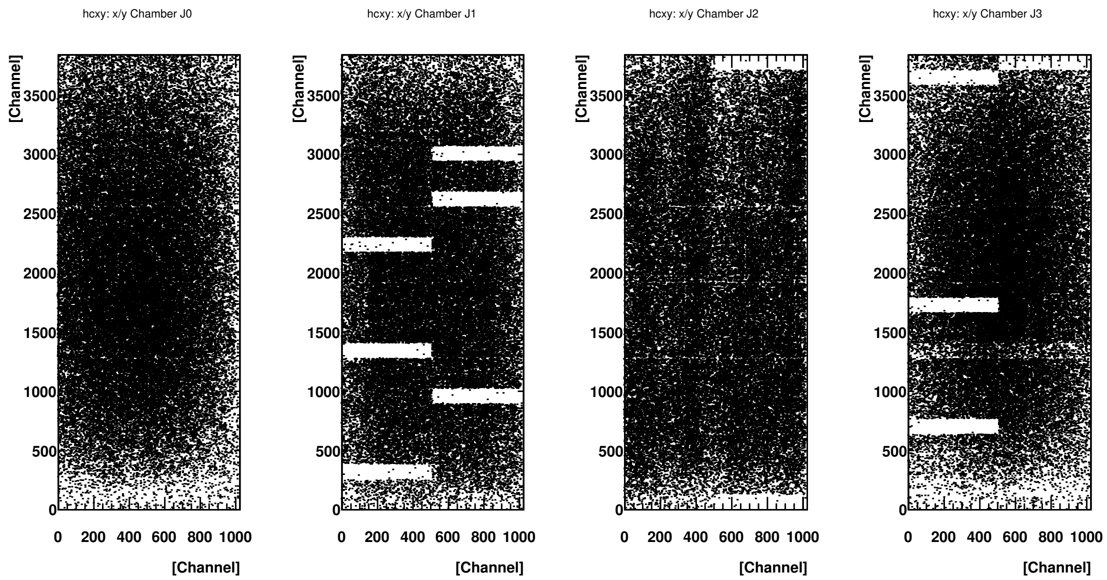

Figure 4.25: The new configuration of the GEM chambers after the replacement of the less efficient modules (August 2019). The slight inefficiency of the mapping is due to the incomplete saturation of the gas inside the GEM chambers.

incomplete saturation of the gas inside the chambers (data was taken during gas filling the chambers). A deeper test of the new configuration is underway.

The latest arrangement of the chambers provide the optimal performances in terms of geometrical efficiency that can be obtained from the available GEM modules.

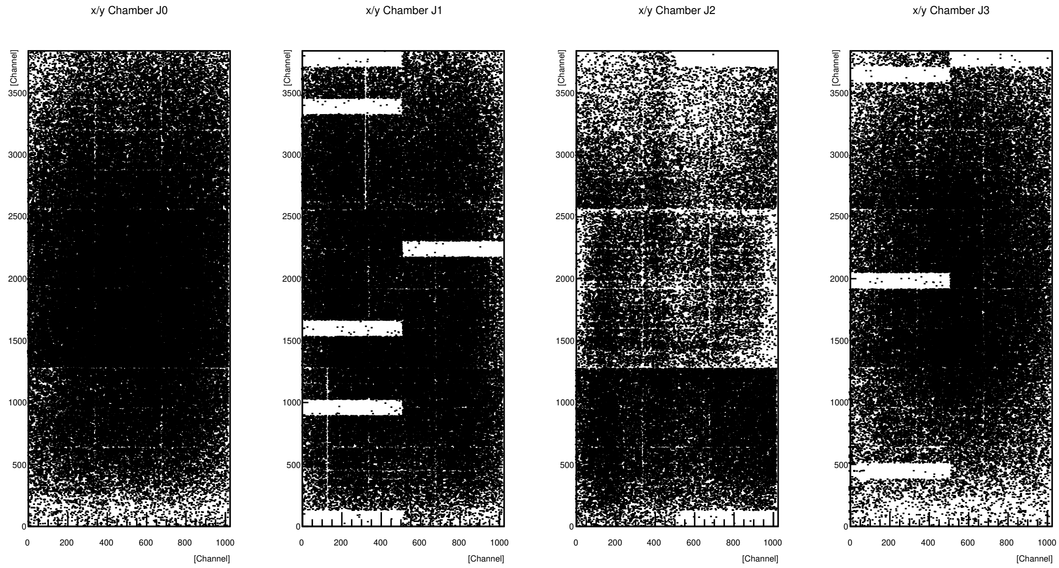

Figure 4.26: Last configuration of the GEM chambers after moving the modules (September 2019). With the new arrangement, the geometric efficiency reaches 95%. The slight inefficiency of the mapping is due to the incomplete saturation of the gas inside the GEM chambers.

Chapter 5

APV signal analysis

In recent decades, the implementation in experimental nuclear physics of sophisticated electronic front-end components with a high density of channels, together with an extensive digitalization, produces a large amount of data that impacts in a considerable way on real-time data transfer, processing and archiving. much of this transferred data represents noise and background signals that have no physical relevance and therefore must be reliably removed during real-time data transfer.

In general, the data sparsification managed by standard thresholding techniques needs dedicated designs or are not able to satisfy exhaustively the requests for noise suppression (insufficient removal of noise or removal of physical interest data). More elaborate, but effective and robust techniques based on Artificial Intelligence (AI), Machine Learning (ML) and Expert Systems (ES) and similar advanced technologies are increasingly adopted in large experiments.

The data transfer and storage, during nuclear physics experiments, performed with modern electronic systems, with the previous digitization of the analog signals and the exploitation of the entire temporal development of the signal through high-frequency sampling, are increasingly hard to organize and especially manage.

This is the context of the Super Bigbite Spectrometer. As already mentioned in the sections 1.2 and 3.1.1, SBS uses highly segmented GEM trackers to remove the high background providing a spatial resolution around 70 μm. The signals of each GEM module are sampled to obtain information on the time used to further correlate them to the trigger time.

The quantity of collected data is much larger than the available data bandwidth and its storage may become problematic (and expensive) and therefore an important data reduction preserving the useful physics information is strongly desirable.

In the present chapter we report on the exploitation of the *Brain Project* (BP) [48] [49] [50] an AI based techniques which can produce robust mathematical expressions (discriminating functions). Such functions can be implemented in firmware to efficiently yet effectively discriminate noise and background from the signals of physical interest. The BP is an highly configurable tool that permits to tune the output analytical expressions, to get the best trade-off between discrimination power and complexity.

A critical aspect of the BP, as common to other AI based techniques, is the definition and generation of consistent, extended and not biased sets of *learning* and *testing*, as discussed and detailed in the data preparation session. In the specific application, at least, the BP automatically discovered and exploited "hidden" features in the learning data sets that contributed to achieve a more discriminating yet efficient and simple criterion for data reduction that the more involved procedure used to generate the data sets: a typical positive byproduct of many AI applications. Moreover, the approach offers the advantage of the powerful AI with a minimal, negligible, investment in resource; it can be tuned to more stringent needs and extended to several other applications.

5.1 Data Acquisition

To fulfill requirements of *SBS project* (see section 1.2), the SBS design consists of a rather conventional detectors but with sophisticated sensors and electronics able to support a particle flux larger than 100 MHz/cm^2.

We remind that SBS uses two highly segmented GEM-chambers detectors for tracking charged particles. Both trackers have two layers of perpendicular strips for simultaneous bi-dimensional reading, for a total of 154112 strips; these strips are read by dedicated electronics based on the 128-channel APV25 chip.

In the section 3.2.2, we saw how the front-end electronic for data transfer from the strips of a GEM module is organized. In brief, each channel of the APV25 samples the input charge signal of a single strip and up to 6 time contiguous samples, separated by 25 ns, of all 128 channels are transmitted along a serial line to a dedicated MPD module which houses fast 12 bit ADCs that digitizes the analog samples.

The time required for the transmission of 128 channel samples, including the overhead of the transmission protocol, is $\sim 3.5\ \mu s$, which becomes $\sim 21.2\ \mu s$ for 6 samples. The MPD, which receives and distributes the trigger to the APV25, handles up to 16 APV25 in parallel and has one FPGA that performs some preprocessing, including sparse readout, before passing the digitized data to a more powerful VME64x Processor Unit (SSP) through a fast, 200 Mb/s, optical fiber point-to-point line driven by a low level Aurora protocol [13]. Each word of information shall therefore include at least the 12 bits of data and some bits (up to 7+4=11) of addressing in case of sparse readout; assuming the maximum occupancy of MPD of 15 APV25, the total amount of data that shall be transferred by the MPD for a single event (no sparse readout) become: 12 bits x 128 channels x 6 samples x 16 APV25 = 144 kbits.

Expecting a maximum of 5 kHz level 1 trigger, the data rate on the MPD-SSP optical fiber is $\sim 700\ Mb/s$ which is 7 times larger than the sustainable rate of 100 Mb/s. The SSP can collect data from up to 32 MPDs ($\sim 2.8\ GB/s$) simultaneously; it properly aggregates and processes them before transmitting to the Event builder (via a VME-2eSST bus which sustains $\sim 200\ MB/s$). Figure 5.1 shows the scheme of the GEM readout.

Therefore, according these calculations, the expected data rates are unsustainable: to reduce the rate in hardware and real time by at least a factor 10 are necessary effi-

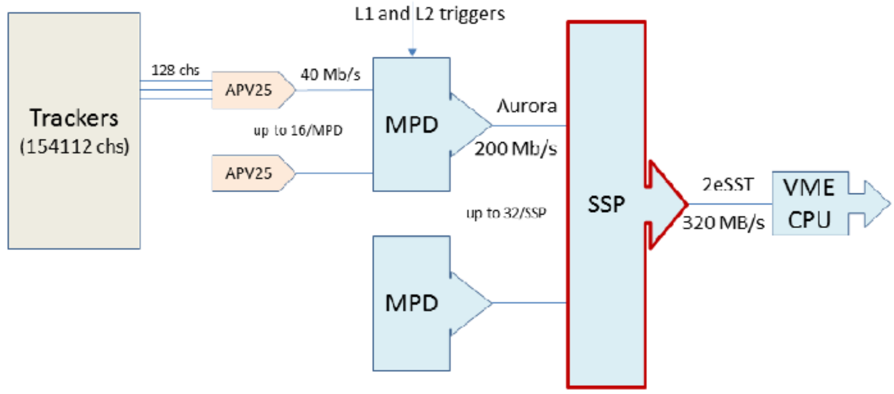

Figure 5.1: SBS tracker readout scheme

cients data sparsification, compression and lower module occupancies. As estimated in various studies, the largest fraction of the acquired pulses will be noise and background uncorrelated to the trigger system.

Noise is generally characterized by small amplitude samples or abnormal sampled shape, while background have a pulse shape statistically identical to the signal of interest but that it is time-shifted respect to the trigger correlated pulse. At the MPD level, electronic channels are considered individually, therefore data suppression is based exclusively on time and amplitude information of each pulses and on higher level external triggers. In the SSP, the topological aggregation of the channels is possible and therefore any data reduction algorithm can exploit peculiar features of the investigated physical process as well as the expected trajectories of the particles that produce the signals.

According to the data transfer electronic architecture just illustrated, we are trying for a robust mathematical function (Discriminating Functions, DFs), which can be implemented in hardware with moderate resources and can discriminate signals of physical interest from noisy or background pulses, as accurately as possible, in real time. This function implementable shall:

- use up to 6 pulse samples;
- have an identification efficiency above 90%;
- obtain a noise compression factor better than 10.

5.2 Data production

Generally, AI systems require specific datasets (learning and testing) which constitute the primary source of information to achieve the intended purpose. In our case, these data sets consist of a large collection of GEM pulses, each of them labeled as noise/background or signal of interest. For best results, datasets need to satisfy the following requirements:

R1 Completeness: each dataset must be composed of all the possible types of pulses (noise/background and signals) coming from the GEM module strips, during its normal operation;

R2 Quantitative mis-identification: the datasets must be well characterized and weighted: each pulse must be tagged with a probability of reliability or mis-identification;

R3 Frequency similarity: the fraction of signals on noise/background must correspond to the one expected during normal operation.

These datasets have generated by X-ray irradiation of the GEM modules, through the same equipment originally implemented to test and characterize the GEM modules in Rome (see section 4.2). The acquisition of the X-ray events is driven by a free running pulsed trigger which is asynchronous with respect to the X-ray hits in the GEM (a X-ray synchronous trigger can be provided by the GEM itself but this introduces biased GEM pulses). This choice was made on purpose precisely in order not to leave the selection of the pulses according to an initially preset timing, but we wanted the timing to be done according to a physical visualization of the pulses and different considerations on the development of the pulses.

5.2.1 Filters selection

In order to comply with the R1 request in 5.2 for datasets (both learning and testing) composition, we considered the use of different GEM modules and different x-ray beam configurations, covering a well defined active area of the modules (X-ray spot), and finally merged casually.

Noisy pulses are easily recognizable with respect to signal by selecting spatial area without X-ray spot or acquiring pulses when the X-ray tube is turned off (pedestal acquisition); we are quite certain that the noisy impulses selected in this way are pure noise since the only contamination that can occur is due to environmental and cosmic radiation. The probability of such contamination is lower than 0.03% (probably an underestimated value but however still negligible) assuming the typical pulse duration of 250 ns and a background rate of 0.5 $particles/s/cm^2$ on the GEM testing area.

Instead, the selection of signal pulses is the result of the combination of different off-line criteria (or *filters*). We have tried different selection criteria, using all the available techniques to obtain a correct discrimination. Actually, some of the explored criteria gave an effective response to signal/noise discrimination, others, instead, included bias effects in the pulses selection which altered the confidence level of datasets, therefore we excluded them. Finally, we have used criteria based on:

1. **Spatial correlation:** spatial cuts around the X-ray spot ("in") to obtain a high level of confidence for the signals and in the regions of the GEM modules out of spot ("out"), to select only noise data.

2. **Pulse amplitude:** thresholding of total charge on the single strip (sum of the ADC values over the 6 samples (s_i), $S_{tot} = \sum_{i=0}^{5} s_i$); threshold is set according to the RMS of the pedestal of each strip.

3. **Temporal correlation:** use of a fit function and its parameters to find the start time of the pulses and the position of the sample with the maximum amplitude value, so as to define correlated/uncorrelated pulses.

The first criteria in 5.2.1 selects, with a high level of reliability, signal (and uncorrelated background) pulses from the noise, given that we know with certainty the region of the GEM module to be investigated. Moreover, focusing the research inside the X-ray beam spot (which has sharp border thanks to the collimation of the X-ray gun) allows us to know and identify the various shape of the signals if compared with the pulses outside the beam spot, that is noisy pulses. In addition, non-overlapping areas have been defined to estimate the noise level and select the noisy data. These regions are identified by adjacent strips along the x and y axes, both in X-rays and in pedestals, and may vary depending on the position of the X-ray gun with respect to the GEM module. The spatial cut largely depends on the geometrical irradiation setup, as shown in Figure 5.2.

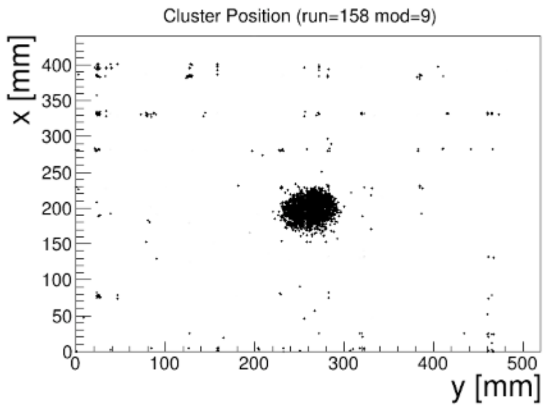

Figure 5.2: X-ray cluster position of a GEM module, used for signals temporal analysis. In this plot an X-ray spot (about 2 mm) is shown in the central region of the GEM module, where we investigated in order to identify signal pulses. While, in the outside of the spot we find exclusively (except for some random contamination) noise pulses, as shown by the slightly noisy channels (small spots arranged like a sort of grid).

The second criteria in 5.2.1, commonly adopted in noise suppression, discriminates signal pulses from noise, according to the charge amplitudes, since the noise pulses, generally, have small amplitudes with respect to signal ones, as shown in Figure 5.3. This filter is represented by the number of pedestal RMS of each strip which define the threshold level above the pedestal baseline. By threshold cuts on data set around 3σ or 4σ (avoiding exceeding 5σ as there is high risk of over-cutting signals of interest), we are able to remove much of the noise. The mathematical relation 5.1 that regulates the threshold level is the following:

$$S_{tot} \geq n_\sigma \cdot \sigma \quad with \quad n_\sigma = 0, 1, 2, 3, ... \tag{5.1}$$

where n_σ is the threshold index and $\sigma = \sqrt{\sum_{i=0}^{5} RMS_i^2} = RMS \cdot \sqrt{6}$. The $\sqrt{6}$ comes out because the RMS is supposed with excellent approximation independent from the sample. Furthermore, it allows to recognize small amplitude cluster tails from comparable pulses of noise that can present shapes and timing similar to the tails of the signal.

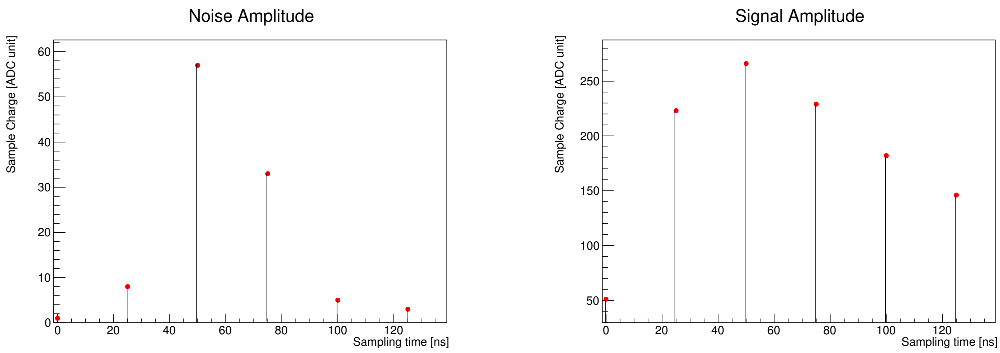

Figure 5.3: Left: noise pulse extracted from a pedestal run, in the context of the X-rays irradiation test, where we can observe a maximum pulse amplitude of about 57 ADC units (pulses could also be observed with lower amplitude). Right: signal pulse extracted from inside the X-ray spot, where we can observe a maximum signal amplitude of about 255 ADC units (signals could also be observed with higher amplitude). We can highlight how the difference between the two amplitudes is quite marked and it could provide a good information about pulses identification, in according to the threshold set by the pedestal RMS.

The third criteria in 5.2.1 introduces a trigger time correlation and therefore identifies the correlated and uncorrelated background pulses; the criteria can be configured to test different temporal correlation scenarios, like early and postponed pulses with respect to the acquisition window, as shown in Figure 5.4. All pulses that have a maximum in a given sample interval (e.g. from s_1 to s_3, with s_0 low enough in ADC unit compared to s_1) are considered signal, while the other are uncorrelated background. The choice of the trigger correlation criterion is basically determined by the trigger jitter, its latency and the length of the APV25 signals.

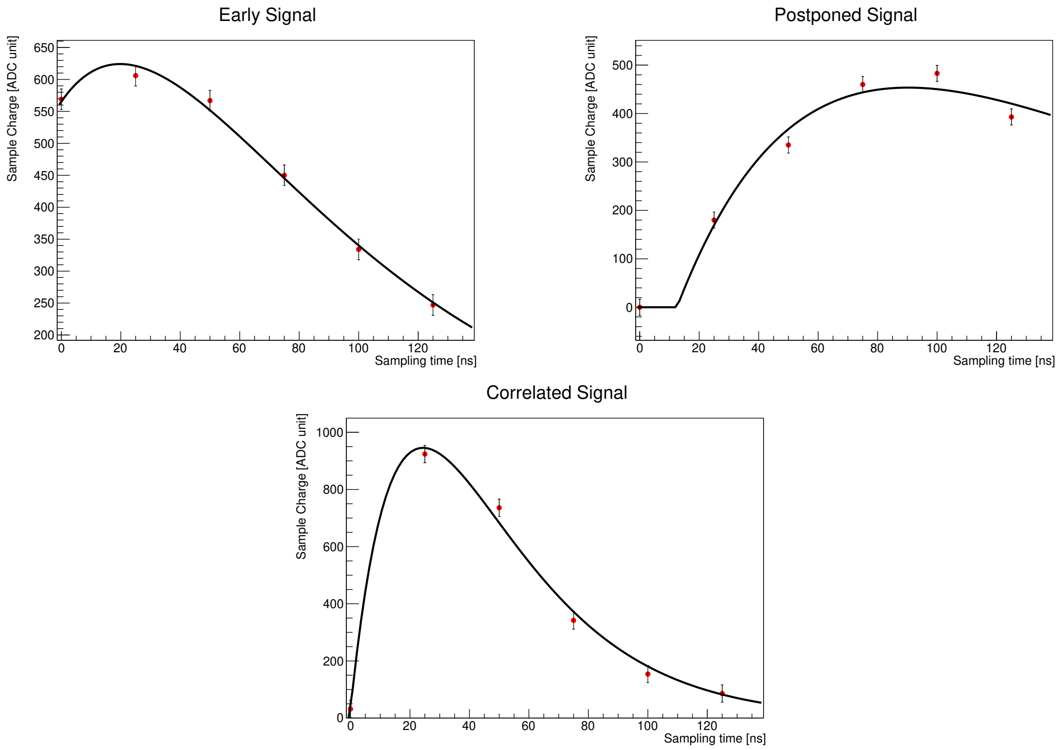

Figure 5.4: Top: early signal (left) and delayed signal (right) compared to the acquisition window, therefore they represent signals uncorrelated background pulses. Bottom: typical correlated signal.

5.2.2 Choice of fit function

In section 3.2.3 we discussed the temporal evolution of the APV25 signal, and its study through a Double-Exponential Function (*DEF*) with four parameters 3.4. Alternatively, taking a cue from the works of *Choong* [51] and *Derenzo* [52] (proceeding by analogy to the APV25 signal case), we can use a Reduced Function (*RF*), as shown by the relation 5.2, which very well represents the six samples of the pulse and allows us to satisfactorily study the time evolution of the signal, in a very similar way to the DEF, as shown in Figure 5.5 left. This function contains four parameters, where t_0 represents the start time of the signal; τ the time constant, A accounts for the amplitude and n a modulating constant.

$$A\left(\frac{t-t_0}{\tau}\right)^n e^{-\frac{t-t_0}{\tau}} \tag{5.2}$$

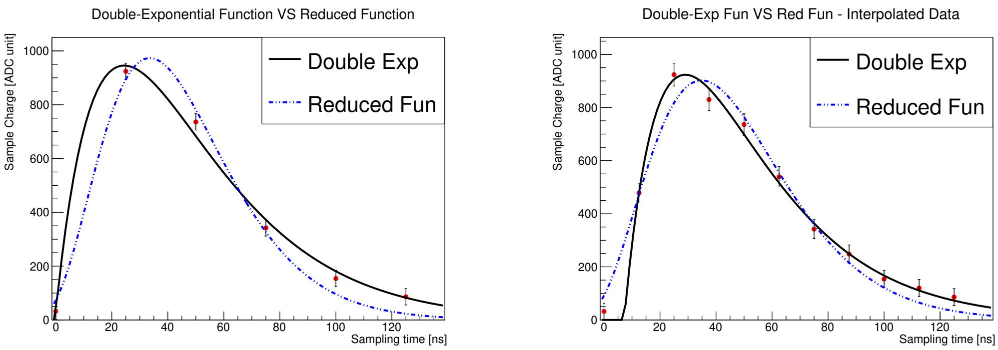

Figure 5.5: Comparison between the DEF (typically used for the temporal study of an APV25 signal) and the RF with $n = 4$. Left: the functions fit a signal with 6 standard samples. Right: the same signal with linearly interpolated samples. In case of interpolation, the differences seem to be reduced and the functions tend to converge in a similar way.

In order to satisfy the third criteria in 5.2.1, the choice of the fit function is of central importance given that the temporal correlation of the signals is established precisely by the quality of the fit parameters.

Initially we tried to exploit the DEF but we noticed a certain instability of the results with regard to the time parameters τ_1 and τ_2, since the functional shape closely reproduce the time evolution of the APV25 but the number of parameters (4) is high respect to the number of available points (6) and therefore in case of uncorrelated pulses, the fit tends to be unstable. Therefore we decided to use the RF since we have the possibility of setting the index n and so reducing the free parameters from four to three, in such a way as to obtain less uncertainty of the results.

We chosen the index n based on the stability and errors of the temporal parameters when the function applied to a data set of 100 typical APV signals. In particular, we went looking for a τ that was congruous to the sampling time of the signal, i.e. 25 ns. Therefore, for each value of n (from 1 to 5) we observed the fit parameters and those that showed a good compromise between errors and requested time constant were the parameters corresponding to n set. Furthermore, to achieve greater stability of the results, we also used linearly interpolated data. Therefore, in addition to the signals with 6 standard samples, simultaneously, we utilized the same APV signals with the interpolated data for a total of 11 samples, as shown in Figure 5.5 right. The results are shown in the Table 5.1. We performed the same analysis for the DEF, as shown in Table 5.2, and compared the results.

Table 5.1, regarding the RF, shows the results of the fit parameters as function of the index n. We observed the trends of the time constant τ, the mean Amplitude relative error and the mean t_0 absolute error. Table 5.2 shows the results of the DEF, where we observed the parameters on the leading (τ_1), the trailing (τ_2), the relative and absolute error about amplitude and start time, respectively.

Reduced Function Parameters	n	6 Samples	Linearly interpolated Samples
Time constant (τ)	1	58.92 ns	58.33 $\pm$ 0.40 ns
Mean A relative error	1	No estimate	3.4%
Mean t_0 absolute error	1	No estimate	2.41 ns
Time constant (τ)	2	36.93 $\pm$ 0.15 ns	37.66 $\pm$ 0.10 ns
Mean A relative error	2	2.3 %	1.7%
Mean t_0 absolute error	2	1.62 ns	1.29 ns
Time constant (τ)	3	28.97 $\pm$ 0.10 ns	29.31 $\pm$ 0.07 ns
Mean A relative error	3	2.3 %	1.5%
Mean t_0 absolute error	3	1.55 ns	1.04 ns
Time constant (τ)	4	24.60 $\pm$ 0.11 ns	24.91 $\pm$ 0.08 ns
Mean A relative error	4	3.0 %	2.1%
Mean t_0 absolute error	4	2.06 ns	1.53 ns
Time constant (τ)	5	21.70 $\pm$ 0.11 ns	22.00 $\pm$ 0.07 ns
Mean A relative error	5	3.6 %	1.9%
Mean t_0 absolute error	5	2.45 ns	1.35 ns

Table 5.1: Values of the fit parameters for the RF by changing the index n. The results concern both standard signals with 6 samples and the same signals with linearly interpolated data (signals with 11 points). The errors on t_0 and A are decidedly low ($A < 3.6\%$ and $t_0 < 2.5$ ns) and comparable to each other, except for $n = 1$. The time constant is close to the time interval between the various samples (25 ns) for $n = 4$. Finally, interpolation tends to stabilize the results and reduce the parameter errors.

Double-Exp Function Parameters	6 Samples	Linearly Interpolated Samples
Leading (τ_1)	79.65 ns	82.89 $\pm$ 0.61 ns
Trailing (τ_2)	80.65 ns	83.29 $\pm$ 1.30 ns
Mean A relative error	No estimate	6.2%
Mean t_0 absolute error	No estimate	5.63 ns

Table 5.2: Values of the fit parameters for the DEF. The results concern both standard signals with 6 samples and the same signals with interpolated data. Leading and trailing appear very similar to each other, which suggests a certain instability of the results since they should show a certain difference.

The results obtained by the RF lead us to the conclusion that the errors on the start time and on the amplitude are quite small, stable and certainly acceptable, except for n = 1. The interpolated data further tend to stabilize the result and reduce errors on the estimated parameters (slightly improves the fit), as we expected. Finally, only one case definitely approaches the required time constant, i.e. the case $n = 4$. Regarding the DEF, the results show errors on t_0 and A higher than the RF, and τ_1 and τ_2 values very similar to each other, leaving some doubts about the stability of the results (according to APV signal shape, the leading and the trailing values must show a certain difference).

In light of this, we have chosen to exploit the RF with $n = 4$, in order to have only three free parameters, and use pulses with the interpolated samples for a better stability of the fit results, as shown in the Figure 5.6.

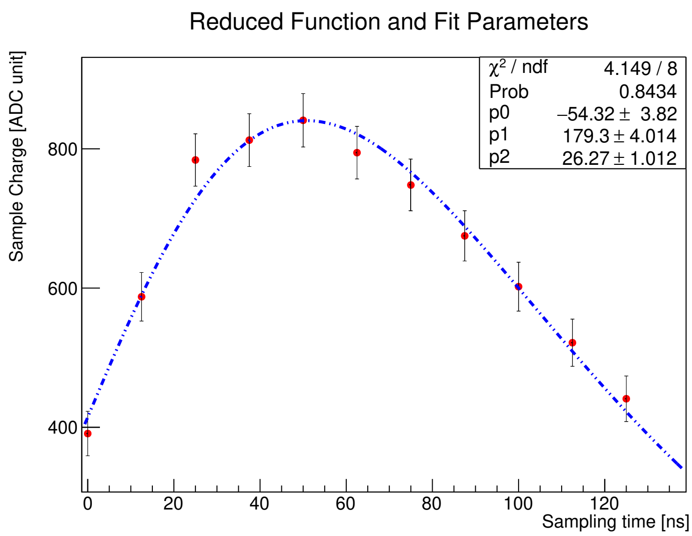

Figure 5.6: Reduced function applied to an APV signal with interpolated data, in fact the number of samples goes from 6 to 11. Interpolation introduces a certain stability on the fit parameters, where p_0 = start time t_0, $p_1 \propto$ amplitude A and p_2 = time constant τ.

5.2.3 Cross correlation analysis

In order to optimize the pulses discrimination through the filters, in particular the temporal correlation, we have tried to observe if the combination of different fit parameters, or quantities deriving from them, showed particular dependencies, not suitably visible at first glance. We performed the cross correlation combining, in addition to the fit parameters, also the first two criteria presented previously in section 5.2.1; in fact, by exploiting the latter conditions, we can study the different trends of the fit parameters when we observe potential signal pulses (inside the X-ray beam spot) and noise (outside the spot) as a function of the total charge threshold (or pulse amplitude according to n_σ in 5.1).

Many of the quantities taken into account did not add any interesting informations, therefore they will not be included in this work. Instead, those that contributed to the optimization of the filters were: threshold number (n_σ), time constant τ, maximum amplitude of the pulse, and $Xmaxf$, which is the value on the sampling time axis corresponding to the maximum value of the function.

All the correlations were carried out both inside and outside the X-ray spot. The first correlation observes the trend of τ as a function of the threshold, as shown in Figure 5.7. Actually, we also performed $Xmax$f and t_0 versus threshold, but these analyzes did not provide new informations.

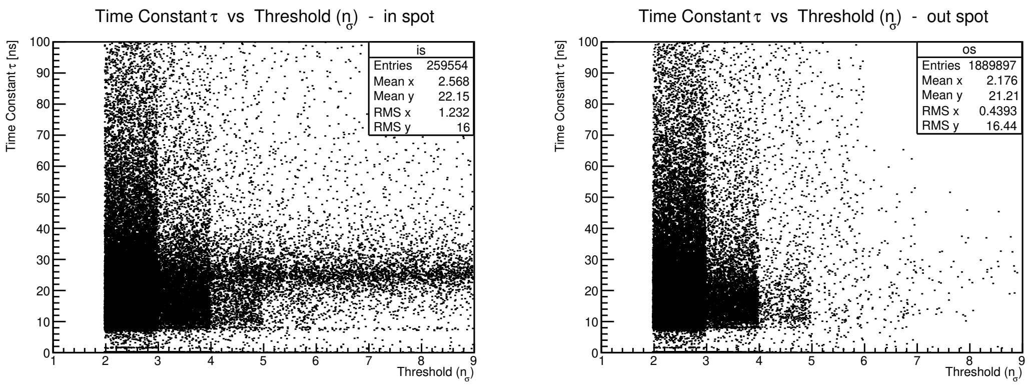

Figure 5.7: Left and right: trend of the time constant (τ) as a function of the threshold (n_σ), inside and outside the spot respectively. A clear trend around 25 ± 10 ns from 4σ onwards is observed, while outside the spot no particular trend.

The plots show interesting trends; inside the spot we cannot observe pulse peculiarities at low threshold values (between 2 and 3), since the presence of noise pulses is excessively high, but starting with $n_\sigma = 4$ (where the noise still seems to be present in a small quantity) we can identify a decidedly clear trend around to 25 ± 10 ns, confirming the results in the Table 5.1. Instead, in the regions free from X-rays, no particular trend is noted, but only a random distribution from 10 to 20 ns, well below the estimated time constant. Therefore, according to this first correlation analysis, a signal must show a τ around 25 ns with a certain dispersion.

With reference to the third selection criterion in 5.2.1, the time-correlation range should be between s_1 and s_3, therefore roughly between 25 and 75 ns. Indeed, viewing over 15000 mixed pulses inside the spot (both correlated and uncorrelated pulses), we observed that the $Xmaxf$ distribution of correlated signals (selecting about 10600 pulses in time, according to our point of view) falls in a range between 20 and 90 ns, as shown by the distribution in Figure 5.8. Therefore, pulses showing an $Xmaxf$ less than 20 ns or greater than 90 ns are considered early or delayed signals, respectively.

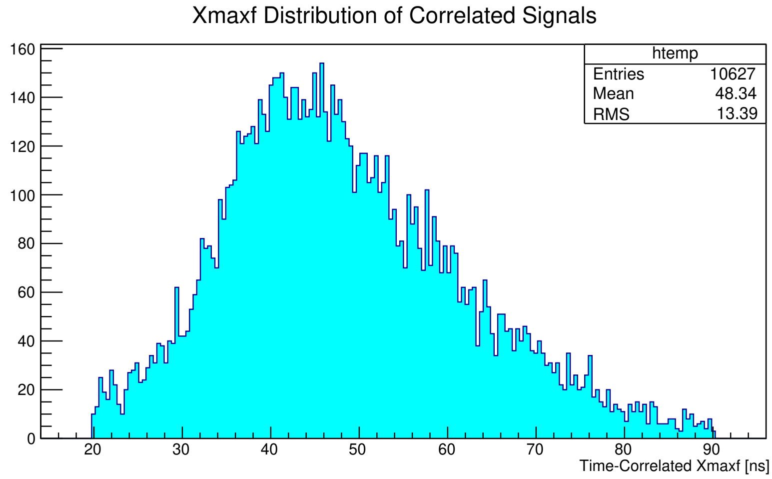

Figure 5.8: The $Xmaxf$ distribution of correlated signals; they fall in a range between 20 and 90 ns.

Until now, the most important informations concerning the discrimination of the signals are provided by the time constant (as function of the n_σ) and the distribution of $Xmaxf$ for signals in time. Therefore, we performed different cross correlations with these main parameters, all to varying of the n_σ. We have changed the threshold from 2σ up to 8σ, so as to observe the growing discriminating effect of criterion 2 in 5.2.1 and at what threshold the noise removal actually begins.

In this thesis we show only the cross correlation at 4, 5 and 6σ. At 3σ there is still an excessive presence of noise, so no great differences between inside and outside the X-ray beam spot can be noticed, while the analysis at 4σ starts to show a certain removal of the noisy pulses, highlighting the first differences, though they are still small. For 5 and 6σ, the differences are clearly marked, identifying the peculiar characteristics for a more precise discrimination. From 7σ onwards, the threshold begins to cut also signals of interest, weakening the differences between inside and outside the spot.

The cross correlation between t_0 and $Xmaxf$ gave further indications, as shown in the Figure 5.9. Under 4σ, the correlations are similar enough (only the number of entries is so different) and there is not so much possibility of noting relevant differences between inside and outside spot. The situation begins to change at 4σ; in fact the number of noisy pulses begins to reduce, highlighting the first differences between inside and outside the spot. At 5σ, the variables inside the spot are distributed more widely along the bisector (absent outside the spot), while a small common distribution to both up to 4σ, out of the bisector, begins to disappear slowly (still well present outside spot). With 6σ, the signals are clearly distributed long the bisector. The distributions outside the bisector line follow a predetermined pattern due to the edge effects of the function in correspondence with very early/delayed or noisy pulses. This distribution shows in which start time interval there is the possibility that the signals are found, so, considering the $Xmaxf$ for correlated signals (from 20 to 90 ns), the range found for t_0 is from -15 ns to -90 ns about. In fact, outside the spot, the t_0 corresponding to the $Xmaxf$ range is quite different.

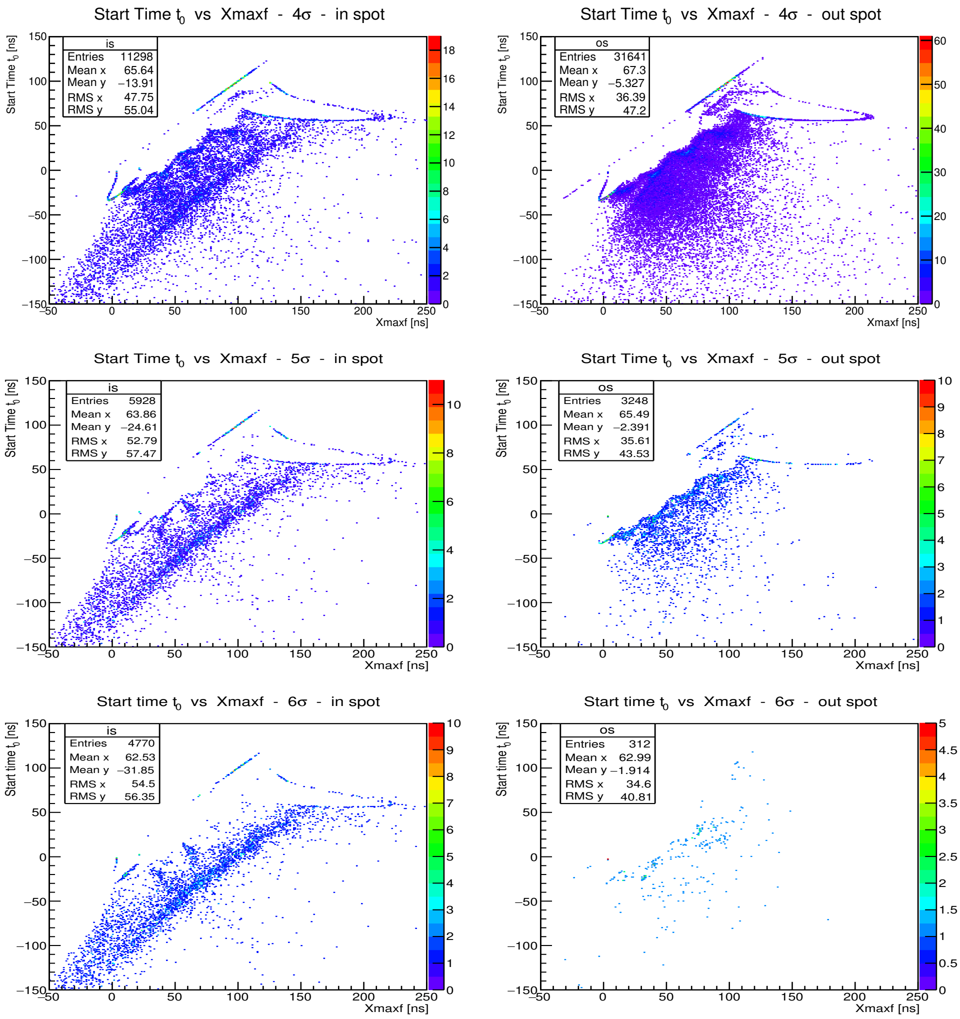

Figure 5.9: Correlation inside and outside the spot, left and right column respectively. Cross correlation between t_0 and $Xmaxf$ from 4 to 6σ (from top to bottom). Starting with $n_\sigma = 4$, the number of noisy impulses begins to reduce, highlighting the first differences between inside and outside the spot. At $n_\sigma = 6$ inside the spot, the signals distribution long the bisector is clearly observed. The distributions outside the bisector follow a specific pattern due to the edge effects of the function in correspondence of early/delayed or noisy pulses.

Similarly, we performed the correlation between τ and $Xmaxf$ to confirm their trends observed up to this point, as shown in Figure 5.10. Also in this case, we find the most informations above 4σ; the distributions, inside and outside the spot at 5σ and especially at 6σ, are diversified well and show a specific trend of the time constant. In fact, thanks to $Xmaxf$ range chosen, we found a distribution of the τ, inside the spot only, around 25 ns ($\pm$ 10 ns), as we expected.

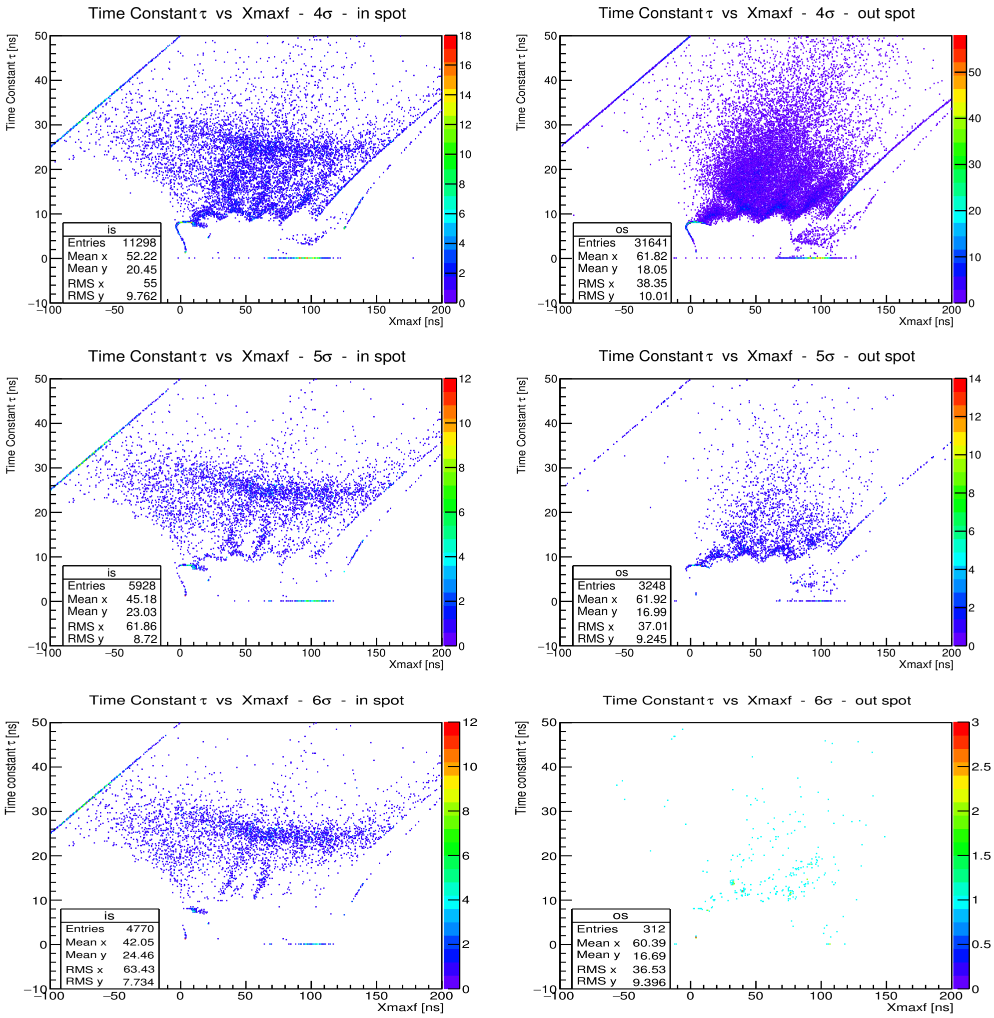

Figure 5.10: Correlation inside and outside the spot, left and right column respectively. Cross correlation between τ and $Xmaxf$ from 4 to 6σ (from top to bottom). A distribution of τ, inside the spot, around 25 ns is observed, considering the $Xmaxf$ range chosen (20-90 ns). Outside the spot, the start time distribution is uncorrelated with the 25 ns. The distributions outside the $Xmaxf$ range follow a specific pattern due to the edge effects of the function in correspondence of early/delayed pulses.

From criterion 2 we have the possibility of making a first discrimination of the pulses through the samples amplitude; in general (always according to RMS of the pedestal), pulses with medium/large amplitude are associated with signals, vice versa they are associated with noise. Therefore, we performed the correlation between τ and the Maximum Amplitude of the pulse to observe if the time constant develops differently inside and outside the X-ray spot, as shown in Figure 5.11. In this case, unlike the other correlations, the time constant develops clearly already starting from 4σ, i.e. it shows a very different trend between inside and outside the spot. The τ inside the spot, excluding the distribution below the value of 50 ADC unit (clearly noise pulses, in fact this distribution tends to disappear by increasing the n_σ), tends on average to the value 25 ns, in line with the expectations, while outside the spot, the τ shows a convergence around 10 ns. These results are strongly confirmed at 5 and 6σ.

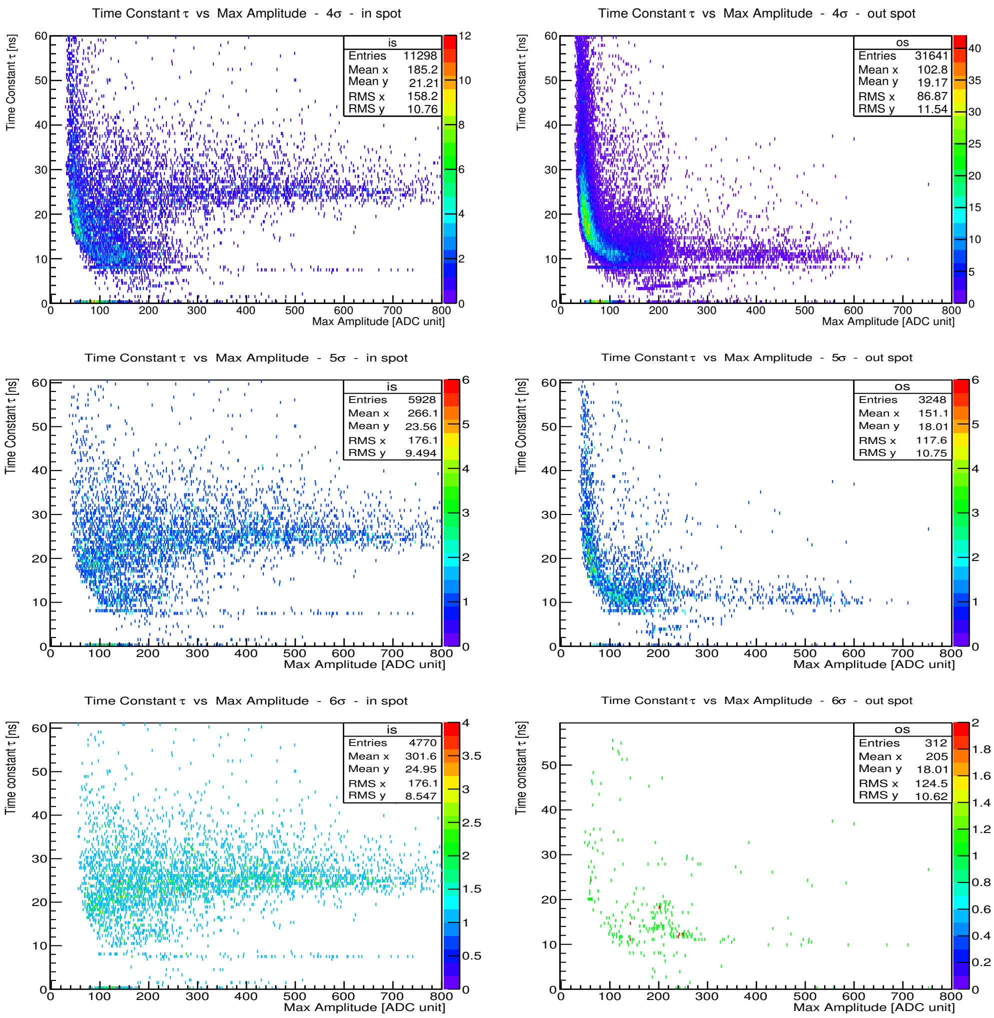

Figure 5.11: Correlation inside and outside the spot, left and right column respectively. Cross correlation between τ and the Maximum Amplitude of the pulse from 4 to 6σ (from top to bottom). The τ inside the spot tends on average to the value 25 ns ($\pm$ 10 ns), while outside the spot, the τ shows a convergence around 10 ns.

Finally, we show the trend of a main parameter when an analysis is performed through a fit function, namely the χ^2. The results obtained through the cross correlation (χ^2 vs n_σ in Figure 5.12) did not meet the expectations, in fact the differences between the inside and the outside the spot were minimal in all cases, preventing the identification of some important feature for pulses discrimination. As shown in Figure 5.12, the trends are practically identical both inside and outside the X-ray beam spot. Even increasing the number of sigma the situation does not change. Therefore, in light of this, the χ^2 parameter is not a good index for signal discrimination, and consequently it was excluded from the analysis.

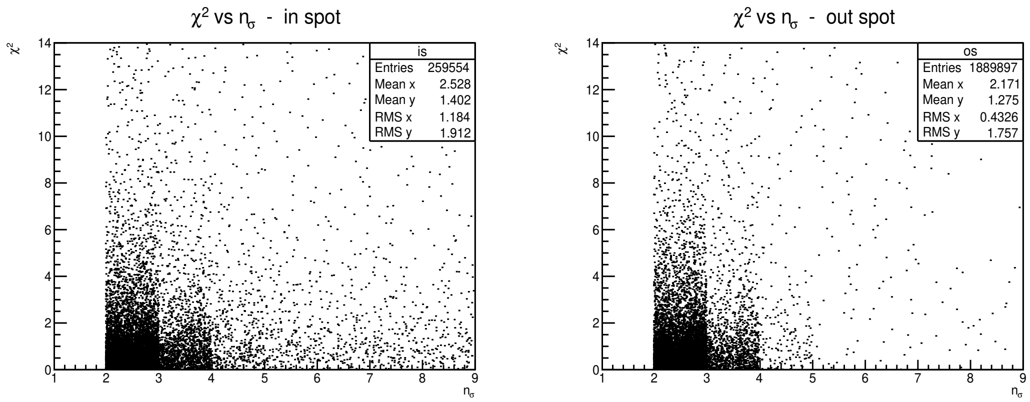

Figure 5.12: Cross correlations between χ^2 and n_σ inside and outside the spot respectively; no marked difference is observable.

From this analysis we ended up with the following signal cuts:: 20 ns < $Xmaxf$ < 90 ns, -90 ns < t_0 < -13 ns and 15 ns < τ < 35 ns.

5.2.4 Filter performance

Critical parameters of the above filters have been optimized looking at their performances on the data in terms mainly of: signal selection (efficiency) and noise contamination. These quantities have been estimated combining X-ray (signal + background + noise pulses) and pedestal (noisy pulses only + a small environmental contamination, X-ray tube off), executed and processed in the very same way.

In the following description, the number of pulses of type t ($t = s, b, n, a$) for signal, uncorrelated-background, noise and all pulses estimated after the application of the above filters to the run R ($R = X$, P for X-ray and Pedestal run respectively) are represented by $N_t^R(f_1,\ f_2,\ f_3)$, where f_1, f_2 and f_3 represent the relevant parameter(s) of the respective filter in 5.2.1. Actually, there are two other criteria, f_{4a} [1] and f_{4b} [2], which take into account the shape of the signal; the samples are compared to the expected APV25 signal output (shape bound to Figure 5.4 bottom), in order to identify the residual pulses which have the proper shape expected from the avalanche development and electronics shaping stages. The f_{4b} criterion is more restrictive than f_{4a}, since it contains more constraints on the signal shape.

We defined in 5.2.1 a region "inside" or "in" in the GEM module, in such a way to completely and safely contain the X-ray spot (see Figure 5.2); additional, not overlapping regions "out" have been defined to estimate the noise level (and select noise data). The filters are applied in both regions. All these regions are identified by adjacent strips along x and y axes, in both X-ray and pedestal runs, and may vary depending on the position of the X-ray gun relative to the GEM module. The number of signals ($N_s^X(in)$) in region "in" of an X-ray run is estimated by:

$$N_s^X(in) \equiv N_a^X(in) - N_n^X(in) = N_a^X(in) - N_n^P(in)\frac{N_n^X(out)}{N_n^P(out)} \tag{5.3}$$

All the other filters parameters or settings have to be tuned as a trade-off of preserving the maximum efficiency related to $N_s^X(in)$ and minimizing the noise contamination $N_n^P(in)/N_a^X(in)$.

The performances of the above filters have been initially estimated on pedestal data which are expected to contain noisy pulses (except for a slight contamination, as mentioned above). Two pedestal runs are taken for the different GEM setup considered: one run is used to generate the pedestals (and RMS of them) while the other is assumed to be a noisy-only run; statistics of about twenty million noise pulses were used. The filters (three different combinations of f_i) are able to reject (or identify) more than $\sim 99.8\%$ of the noisy pulses with a threshold $\geq 4\sigma$ of the pedestals, as shown in Figure 5.13: as expected, the distribution of the charge noise is not a pure Gaussian.

Once verified that the filters behave consistently on the noisy runs, they have been applied to the data acquired with X-ray on, collimated on a well defined regions of the GEM modules, as shown by the X-ray spot x/y profiles in Figure 5.14.

[1] f_{4a}: $f_1\&f_2\&f_3\&(s_0 < s_1)$.

[2] f_{4b}: $f_1\&f_2\&f_3\&(s_0 < s_1)\&(s_3 > s_4)\&(s_3 > s_5)$.

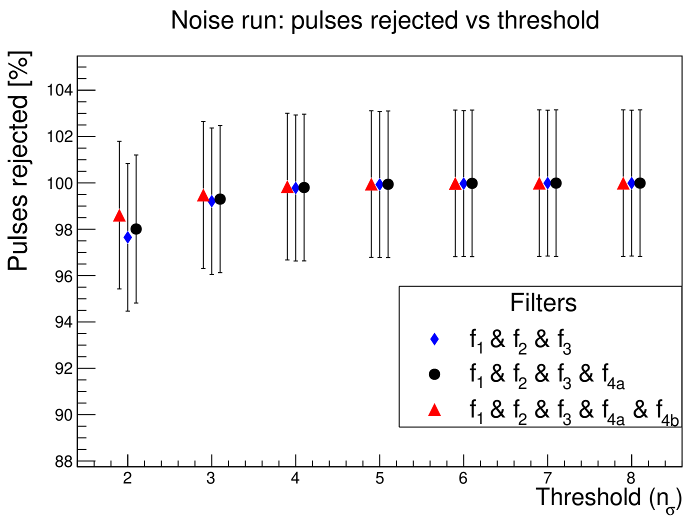

Figure 5.13: Fraction of rejected pulses for the different filters discussed in the text in a noise-only run, as a function of the filter 2 threshold; to avoid overlap, the points are slightly shifted respect to the nominal integer threshold.

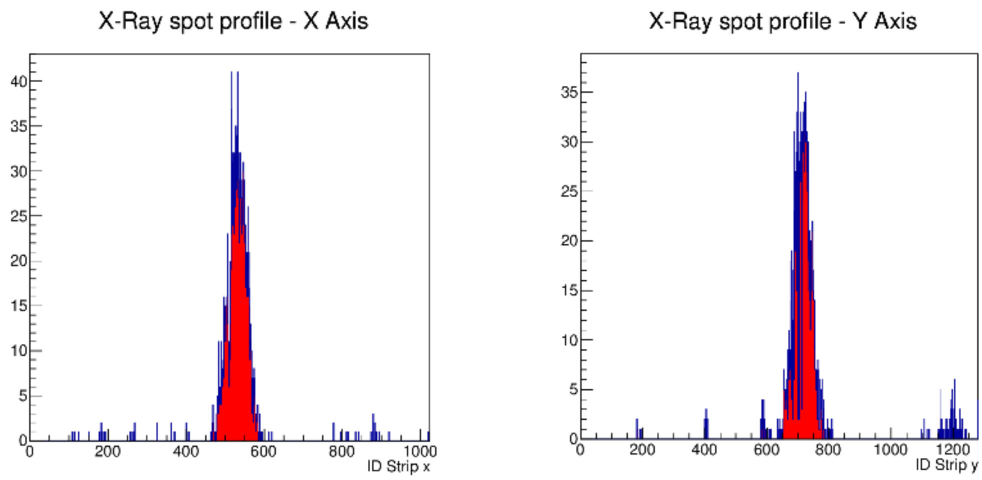

Figure 5.14: X-ray spot profile along x and y axes, left and right respectively. Spot is very sharp and its borders are well defined. Noisy strips are visible outside the spot.

The effects of the filters are summarized by Figure 5.15 where the number of signals (above equation 5.3) and noise contamination are reported as a function of the threshold (n_σ of filter 2) for the different selections.

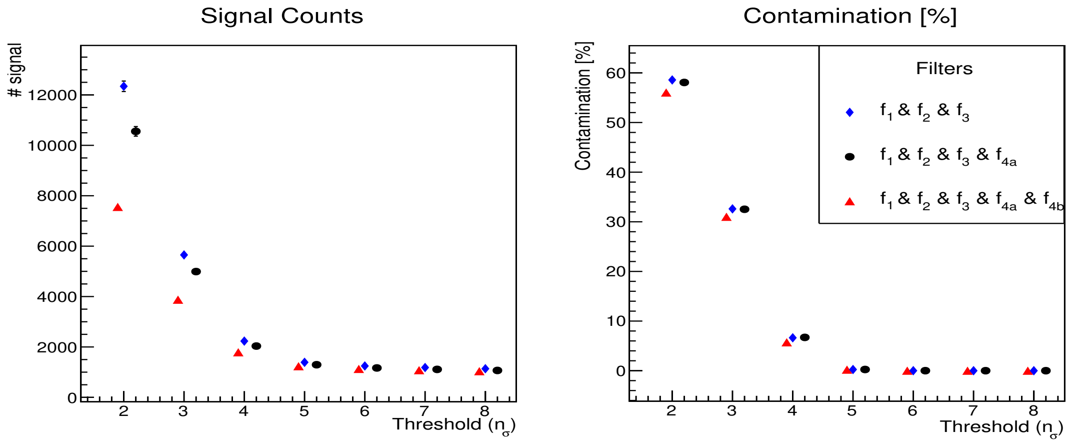

Figure 5.15: Left: the filtered signals inside the X-ray spot as a function of the threshold of filter 2. Right: the contamination as function of threshold.

Applying the filters $f_{1,2,3}$, for $n_\sigma < 3$, the estimation of the number of signals is overwhelmed by number of noisy pulses, while this quantity becomes consistent for $n_\sigma \geq 3$, and starts to decrease and then to stabilize for $n_\sigma = 5$ onwards (Figure 5.15 left). When the filters $f_{4a/b}$ are applied for $n_\sigma < 3$ the number of signals found drops, since they probably insert a bias effect in the selection of the pulses; while for $n_\sigma \geq 5$ the signal counts become constant (like $f_{1,2,3}$). Instead, the noise contamination remains more or less the same for the three filter combinations, and it also shows to be good at $n_\sigma = 4$ (about 7%) and excellent for $n_\sigma \geq 5$ (close to 0), as shown in Figure 5.15 right.

The introduction of the $f_{4a/b}$ filters do not add anything as regards the discrimination of the pulses, but, on the contrary, they probably worsen, albeit slightly, the identification of the signals, and therefore these filters have been omitted from the analysis.

5.3 Learning and testing datasets

The above analysis of filters has supported the definition of data sets and their quantitative characterizations (as for the previous requirement R2); moreover, an $n_\sigma < 5$ provides a great variety of probable signals, while an $n_\sigma \geq 5$ gives a reasonable security to include the largest fraction of signals produced in the GEM (requirement R1); finally, the relative abundance of noise, background and signal can be easily changed and suitably quantified, to reproduce different experimental conditions (requirement R3).

A supervised learning [53] is adopted when a set of data is available comprising typical input examples with corresponding outputs. In this way the tool can learn to infer the relationship that binds them. Datasets as input to the BP have been created according to the following procedure:

1. collimated X-ray (Figure 5.14) and pedestal runs are produced with different configuration and then processed;

2. each pulse extracted from the detector strips is classified by the above 3 filters:

   – Signal: pulses in the X-ray runs that passed all filters (within the spot region), are classified as physical signals.

   – Noise: pulses rejected by any filter, outside the spot region (both in the X-ray and pedestal runs), are classified as noise.

   – Background: all pulses in the X-ray runs that passed the filters, except time-correlation filter 3, within the spot region, are classified as physical uncorrelated background signals.

A typical dataset is a list over 1500000 pulses which guarantees a more than adequate statistics; each pulse is made by 6 ADC values s_i one for each sample $i = 0, 1, 2, 3, 4, 5$ and its attribute (or output): 0 for "pure" noise, 1 for "pure" signals and values in between to provide the level of confidence (weight) of the output, according to the percentage of noise contamination in Figure 5.15, when the threshold n_σ changes. The weight is calculated using the relation $[1 - (cont.\%/100)]$, and therefore we obtain 0 for minimum and 1 for maximum probability, as shown for 6 pulses in the Table 5.3, as an example.

Pulse	n_σ	Samples s_i [ADC units]	Lrn/Tst output	Weight
Signal 1	> 8	124 306 364 323 251 194	1	1
Signal 2	3.5	7 48 50 40 21 8	1	0.72
Noise 1	2.1	10 21 16 24 18 17	0	1
Noise 2	3.4	0 32 46 44 23 6	0	1
Background (early)	> 8	284 237 17 0 0 3	0	1
Background (delayed)	> 8	7 10 23 99 278 361	0	1

Table 5.3: Example of 6 pulses for the learning/testing dataset. Each pulse is represented by the 6 charge samples in ADC units, the output and its weight. We attribute the output 1 for the signal, while the value 0 for noise/background. In addition, each output has an associated weight to establish its reliability (continuous values from 0 to 1); 1 for maximum reliability, 0 for the minimum, according to the percentage of contamination as a function of n_σ. Figures 5.16, 5.17, and 5.18 show the representation of the pulses of this table.

The fraction of the number of signal/noise pulses in the dataset has been set to 5/95, which is expected to be close to the experimental conditions. Learning and testing datasets are statistically identical with randomized pulses selected according to the above procedure.

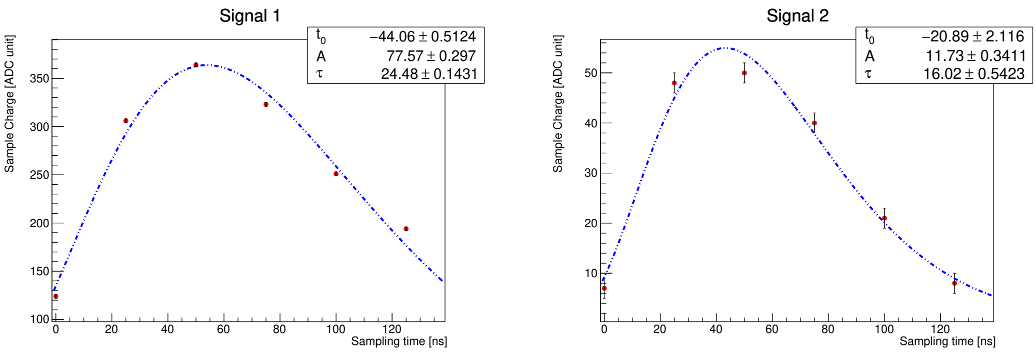

Figure 5.16: Left: pulse from the X-ray spot, at $n_\sigma > 8$; it passes all the filters, as shown by the fit parameters, and therefore it is classified as a signal (output 1) with a weight of 1 (100% reliability). Right: pulse from the X-ray spot, at $n_\sigma = 3.5$; it passes all the filters, as shown by the fit parameters, therefore it is classified as a signal (output 1) with a weight of 0.72 (72% reliability), since it is in a n_σ with a moderate contamination, as shown in Figure 5.15 right.

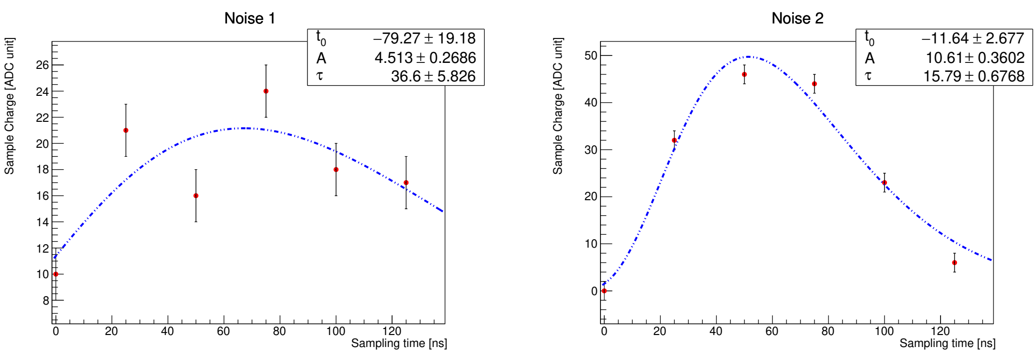

Figure 5.17: Left: pulse from the pedestal outside the X-ray spot, at $n_\sigma = 2.1$; it is classified pure noise (output 0) with a weight of 1 (100% reliability). Right: pulse from the pedestal outside the X-ray spot, at $n_\sigma = 3.4$; it is classified noise (output 0) with a weight of 1 (100% reliability), despite the great resemblance to a signal. In any case, they would not have passed the filters; constant time (Noise 1) and start time (Noise 2) out of range.

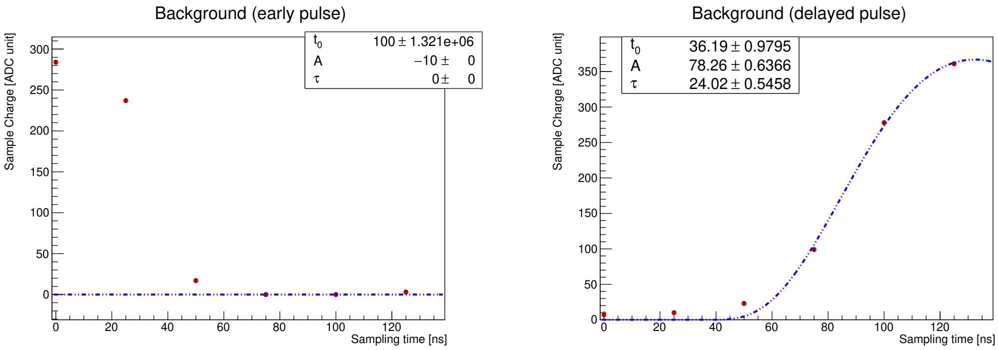

Figure 5.18: Left: pulse from the X-ray spot, at $n_\sigma > 8$; it does not pass the filters since a clear early pulse (totally nonsensical fit parameters), therefore it is classified background (output 0) with a weight of 1 (100% reliability). Right: pulse from the X-ray spot, at $n_\sigma > 8$; it does not pass the filters since a clear delayed pulse (start time out of range), therefore it is classified background (output 0) with a weight of 1 (100% reliability).

5.4 First preliminary training

A first attempt to train the BP has been already done on preliminary datasets. By simulations three different discriminating functions were generated and they showed a good propensity to distinguish signal from noise/background, in first approximation. For generating the learning and testing datasets of simulation a slightly different method was used than the one illustrated above (similar considerations but criteria and cuts non-optimized). In fact, the functions found were satisfactory under certain condition, but did not reach the target set in a general context, therefore they were not taken into consideration.

First BP simulations have been precessed with statistically equivalent learning datasets as input, but changing the complexity constraints [54] on the output functions; the three most representative output discriminating functions produced by the BP simulations are considered in the following discussion:

1. t_∞: no complexity constraints, it may represents the best solution in terms of performances (on learning and testing datasets) but its implementation in the MPD firmware is critical and the function complexity[3] is possibly influenced by specific details of the learning datasets only (memory effect) and therefore can result in reduced performance on different set of data;

2. t_7: is a simple, yet rather powerful, discrimination function as discussed later:

$$t_7 = erf[5 \cdot 10^{-5}\, s_2\, (s_0 + s_4)] \tag{5.4}$$

   the erf() function is only used to have an output domain between 0 and 1, but it is not strictly required. The scale factor in front of the samples keeps the acceptable threshold range between 0 and 1;

[3] $t_\infty \propto s_2 \cdot abs(5.7e{-}05 \cdot s_3 \cdot ((0.000534699 \cdot s_1 \cdot (s_0+s_5-s_2) \cdot (s_0-0.836429 \cdot s_2)) - s_1 + s_4) \cdot ((3.48614e{-}07 \cdot (392.713+s_4) \cdot (-43.659+s_0) \cdot (s_0+s_5-s_4) \cdot (s_5-s_3+s_0)) - s_4)) \cdot cosh(0.0229395 \cdot (s_3+s_0-1.4766 \cdot s_5)) \cdot (s_1+s_5)$

3. t_5: one of the simplest functions, that uses only two samples:

$$t_5 = erf\left[1 \cdot 10^{-4} s_4 s_2\right] \tag{5.5}$$

considerations similar to t_7 apply.

Table 5.4 reports for each function, the complexity indexes (nodes and number of samples), the errors of the BP and the level of implementability [54].

Name	Features	Nodes	Error	Implementation
t_∞	6	17	17.25%	unlikely
t_7	3	7	38.8%	easy
t_5	2	5	47.2%	easy

Table 5.4: Characteristics of each BP model. The features correspond to the number of samples entering the function expression; features and nodes numbers roughly quantify the level of complexity; error is proportionally correlates the learning error with the true variability of the output.

Symbol	**Definition**
c_0	Pulses correctly identified as noise
c_1	Pulses correctly identified as a signal
$c_t = c_0 + c_1$	Tot pulses correctly identified
w_0	Pulses wrongly identified as noise
w_1	Pulses wrongly identified as signal
$w_t = w_0 + w_1$	Pulses wrongly identified
$t_0 = c_0 + w_1$	Total noisy pulses
$t_1 = c_1 + w_0$	Total signal pulses
$t_p = t_0 + t_1$	Total pulses
Derived performance indeces	
c_1/t_1	Efficiency
w_1/t_0	Noise Suppression Factor
$w_1/(c_1 + w_1)$	Contamination
w_t/c_t	Misidentification

Table 5.5: Notation for BP outcomes analysis; fixed the total pulses t_p, the four quantities c_0, c_1, w_0 and w_1 are no longer independent.

Learning and testing consistency and performances: the performances of the above functions are quantified by the following four quantities (performance indexes), with notation defined in Table 5.5):

- *Efficiency*: the fraction of signals passed relative to the total signals examined;
- *Noise Suppression Factor*: the fraction of noisy pulses identified as signals relative to the total number of noisy pulses;
- *Contamination*: the fraction of noisy pulses wrongly assigned to signals relative to the total pulses identified as signals.
- *Misidentification*: the ratio between the pulses wrongly identified and the pulses correctly identified.

The consistency of each function is evaluated comparing the performances of the learning and testing datasets, in terms of Efficiency and Contamination (the other two quantities behaves, for our purposes similar to the Contamination) versus the discrimination threshold ranging from 0 to 1.

The three discriminating functions have then applied to a testing dataset composed by data from different runs and GEM modules in order to get the maximum statistical significance, as shown in Figure 5.19: the cardinality has raised to $1.6 \cdot 10^6$ strip pulses while the fraction os signal/noise has kept equal to 5/95 as for the above learning and companion testing datasets.

Function t_∞ looks as the best of the three functions: it discriminates correctly from 100% to 96% in a threshold range 0.1-0.5 and it also shows an impressive Noise Suppression, however its complexity is so high that its firmware implementation would require a large resources which are unavailable in the current GEM electronics. The function represents somehow the upper, optimal, discrimination limit: t_∞ achieves an efficiency close to 100% with very low contamination at the cost of larger complexity of the function.

The t_5 function shows an acceptable efficiency only for relatively low thresholds but with a considerable contamination (larger than 10%).

Eventually t_7 maintains a good efficiency ($\geq 90\%$) even at relatively large threshold values, where the contamination is well below 10%; it is close to the optimal trade-off between contamination, efficiency and implementation complexity. In the above analyses the discriminating functions have been applied to filtered data, showing excellent performances. The ultimate performances of these functions have estimated on a large set (2 millions pulses) of raw, unfiltered data. The number of signals and the contamination obtained by the discriminating functions are compared to those of the filters used to generate the learning and testing datasets. Unfortunately, the results do not reach the objective sought, i.e. efficiency and contamination obtained by the functions (f_1 & $t_{5/\infty}$) seem to have slightly lower performance than those obtained with filtered data. The unfiltered t_7 points are between the unfiltered t_5 and t_∞; they are not represented for the sake of clarity. For best results, the functions must operate on pre-filtered data (f_1 & f_3 & $t_{7/5/\infty}$), as summarized by the plot of Figure 5.20. Therefore, the functions

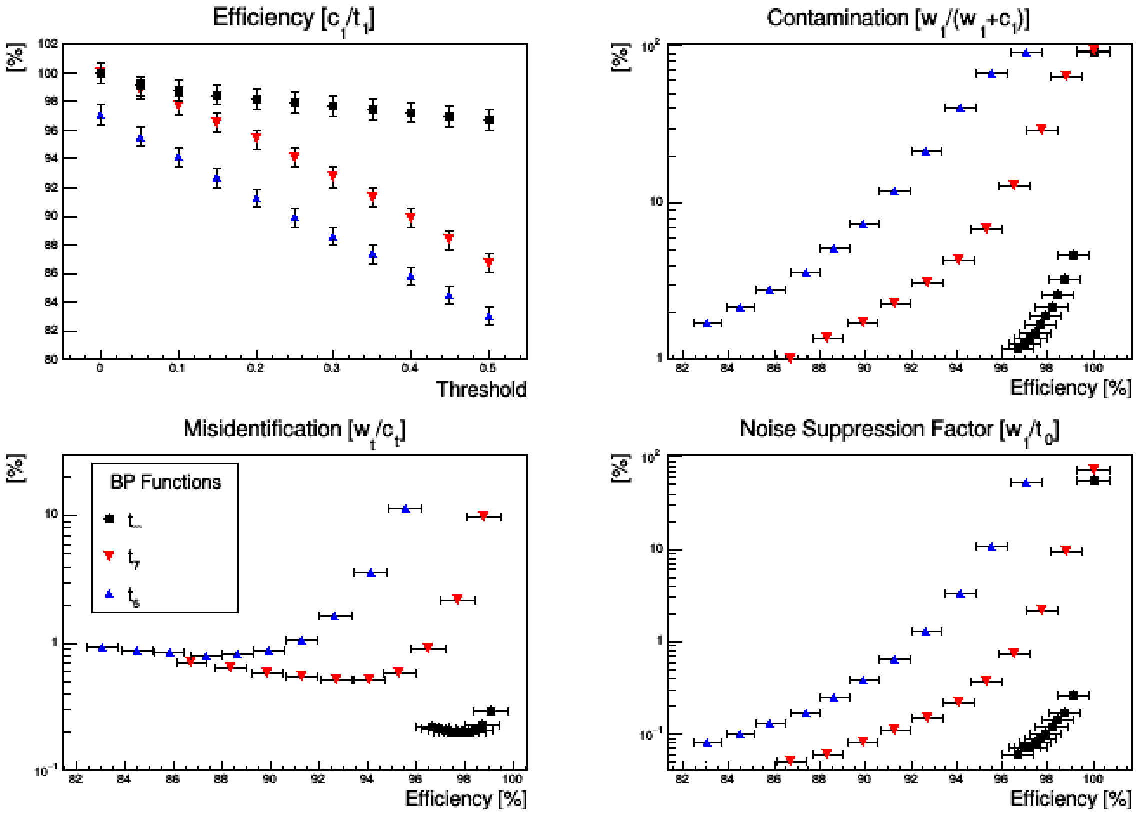

Figure 5.19: BP discriminating function performances on a large set of filtered data ($1.6 \cdot 10^6$ pulses) that are statistically independent from the learning and testing datasets. Top left: the efficiency as a function of the threshold of the discriminating functions (properly scaled). Contamination, Misidentification, and Noise Suppression Factor are reported on the other plots as a function of the efficiency. It clearly appears that function t_7 is a good compromise between the t_∞ and the t_5.

seem to be affected by a bias, due to the non-optimized filters for the generation of the learning and testing data sets. For this reason, we have raised the level of in-depth of study of the APV pulses and analyzed different aspects previously neglected. The new optimized filters and the procedure for generating the learning/testing data sets are those illustrated above sections.

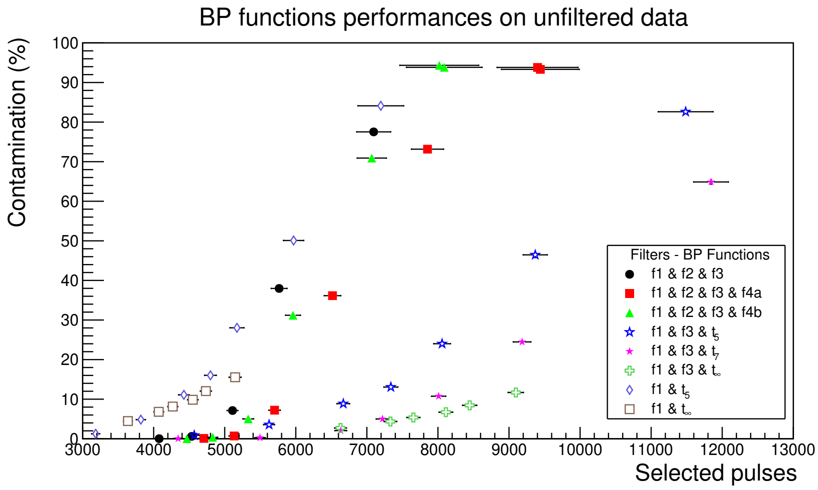

Figure 5.20: Performances (contamination versus number of signals) of the BP functions on real, filtered data; at any given contamination, the BP functions are more efficient than the filters adopted to generate the learning datasets.

Chapter 6

Conclusion

In this thesis, we discussed the characterization of a GEM detector that will be used as tracking device in the Hall A SBS/BB spectrometers at Jefferson Lab; the SBS/BB spectrometers are devoted to high luminosity experiments for the study of the nucleon structure and dynamics. We introduced the GEM technology and motivated its choice as tracker in high background conditions. We illustrated the assembly procedures of the triple GEM chambers, the mechanical components and the quality controls procedure, focusing on the preliminary checks of the GEM foils.

A central part of this work involved the first characterization of the GEM modules, after assembling: gas tightness check, HV training and X-ray source irradiation with relative analysis. Then module integration at JLab and then commissioning have been extensively discussed. The best 12 GEM modules have been integrated to form 4 layers of the tracking system and have tested through cosmic rays. The cosmic ray characterization was performed at different high voltage (from 3800 V up to 4100 V) and gas fluxes. Stability of the chambers, their charge collection properties and their efficiencies have been estimated along several months.

The charge correlation observed is quite satisfactory, the results show that the charges are equally divided along the x-y strips of the readout, according to our expectations.

The hit efficiency showed that the applied voltage of 3800 V is not sufficient for the formation of clusters and consequently the efficiency is very low in all GEM chambers. While at 4100 V of each GEM chamber showed satisfactory results. The applied voltage allows the maximum performance of the detectors according to our expectations.

Finally, the tracking efficiencies as a function of the applied voltage is shown. The results highlighted how the efficiency increases with increasing voltage, confirming the results of the hit efficiency. Furthermore, we observed how the tracking efficiency of the GEM system is over 90% at 4100 V in spite of some inactive sectors, as our expectation.

During the cosmic tests we experiences 3 modules that had GEM foils shorted, during rumping up of the high voltages after relatively long period of inactivity (with gas not flushing). The most plausible reason of these failure is probably the level of humidity inside the module, which requires continuous (or long period) gas flushing before powering the High Voltage. In the end, we replaced the worst modules and moved the less-efficient modules to edge of the chambers, in order to position as many inactive sectors as possible outside magnetic spectrometer acceptance. With the optimal configuration of modules, the geometric efficiency increased up to 95% and if we consider magnetic acceptance, the geometric efficiency could rise up to around 97%.

In the second part of the activity of this thesis, we have investigated an effective and solid method to remove background data from the real-time data stream, to get a sustainable data rate. In high luminosity experiment the amount of collected data may become problematic and therefore a data reduction preserving the useful physics information is desirable to minimize data acquisition and storage complexity and cost. In fact, much of this data represents noise/background pulses that have no physical relevance and therefore must be reliably removed during real-time transfer.

We described the possible exploitation of the Brain Project tool (BP), an AI-based technique that can produce robust mathematical expressions (discriminating functions), which can be implemented in firmware to efficiently discriminate noise and background from the signals of physical interest.

An important aspect of the BP, as common to other AI-based techniques, is the definition and generation of consistent, extended and not biased sets of learning and testing data set. Therefore, we have carried out a depth study on the APV signals (through a fit function with 3 parameters), in order to identify the characteristics of the pulses relevant for their classification as signal or noise/background. Then we have defined and implemented the procedure for the production of consistent learning and testing datasets. Finally, we attempted a preliminary application of the dataset to the BP tool to get discriminating functions which have been analyzed and characterized. The results have been used to improve the learning and testing datasets. The next step will be a second training to get more robust and effective functions, and then try their implementation in the data-acquisition firmware.

Bibliography

[1] Jefferson Science Associates, https://www.jlab.org/accelerator, Accelerator Science.

[2] C. Perdrisat and V. Punjabi, Scholarpedia **5**, 10204 (2010), revision #143981.

[3] K. de Jager, International Journal of Modern Physics E **19**, 844 (2010).

[4] C. F. Perdrisat, V. Punjabi, and M. Vanderhaeghen, Prog. Part. Nucl. Phys. **59**, 694 (2007).

[5] J. Arrington, P.G. Blunden, and W. Melnitchouk, Progress in Particle and Nuclear Physics **66**, 782 (2011).

[6] Bogdan Wojtsekhowski, International Journal of Modern Physics: Conference Series **35**, (2014).

[7] E. Cisbani, M. Jones, N. Liyanage, L. Pentchev, A. J. R. Puckett, B. Wojtsekhowski (GEp/SBS, and Hall A Collaborations), *Update on E12-07-109 to PAC 47: Large Acceptance Proton Form Factor Ratio Measurements up to 14.5 GeV*^{2} *Using Recoil-Polarization Method*.

[8] G. Cates, S. Riordan, B. Wojtsekhowski, and the Hall A collaboration, *(A New Proposal to Jefferson Lab PAC34) - Measurement of the neutron electromagnetic form factor ratio* G_E^n/G_M^n *at high* Q^2, 2009.

[9] J. Annand, R. Gilman, B. Quinn, B. Wojtsekhowski, and the Hall A collaboration, *A new proposal to the Jefferson Lab Program Advisory Committee (PAC34) - Precision Measurement of the Neutron Magnetic Form Factor up to* $Q^2 = 18.0$ *(GeV/c)*^{2} *by the Ratio Method*, 2008.

[10] G. Cates, E. Cisbani, G.B. Franklin, A. Puckett, B. Wojtsekhowski, and 12-09-018 collaboration, *A Proposal to Jefferson Lab 12 GeV - PAC38, Update toPR12-09-018, conditionally approved by PAC34 and PAC37 - Target Single-Spin Asymmetries in Semi-Inclusive Pion and Kaon Electroproduction on a Transversely Polarized* 3^He *Target using Super BigBite and BigBite in Hall A*.

[11] J. R. M. Annand, B. Wojtsekhowski, B. Sawatzky, N. Piskunov, V. Bellini, M-Kohl, , and Hall A collaboration, *A Proposal to Jefferson Lab 12 GeV - PAC38, Update*

toPR12-09-018, conditionally approved by PAC34 and PAC37 - Target Single-Spin Asymmetries in Semi-Inclusive Pion and Kaon Electroproduction on a Transversely Polarized $3^{H}e$ *Target using Super BigBite and BigBite in Hall A.*

[12] L. Pentchev, B. Wojtsekhowski, and E. Cisbani, *The Super-Bigbite Spectrometer for Jefferson Lab Hall A - Detector Counting Rates and Tracking Analyses, Chapter 2, 3, 5* (JLab, Newport news - Virginia (USA), 2010).

[13] Jonathan Carroll, Anthony Thomas, Johann Rafelski, and G. Miller, (2011).

[14] Markus Diehl, Thorsten Feldmann, and Peter Kroll, Physical Review D **77**, (2008).

[15] HAIYAN GAO, International Journal of Modern Physics E **12**, 1 (2003).

[16] R. G. Sachs, Phys. Rev. **126**, 2256 (1962).

[17] E. B. Hughes, T. A. Griffy, M. R. Yearian, and R. Hofstadter, Phys. Rev. **139**, B458 (1965).

[18] A. I. Akhiezer and Mikhail.P. Rekalo, Sov. Phys. Dokl. **13**, 572 (1968), [Dokl. Akad. Nauk Ser. Fiz.180,1081(1968)].

[19] A. I. Akhiezer and Mikhail.P. Rekalo, Sov. J. Part. Nucl. **4**, 277 (1974), [Fiz. Elem. Chast. Atom. Yadra4,662(1973)].

[20] Raymond G. Arnold, Carl E. Carlson, and Franz Gross, Phys. Rev. C **23**, 363 (1981).

[21] Punjabi, Vina and Perdrisat, Charles F., EPJ Web of Conferences **66**, 06019 (2014).

[22] Michael Kohl, Nuclear Physics A **805**, 361c (2008), iNPC 2007.

[23] M. K. Jones et al., Phys. Rev. Lett. **84**, 1398 (2000).

[24] J. O. Hansen, AIP Conf. Proc. **1441**, 162 (2012).

[25] C.F. Perdrisat for GEp(3) collaboration, *Update of Jlab experiment 01-109, submitted to PAC 26 - Measurement of* G_{Ep}/G_{Mp} *to* Q^2*=9* GeV^2 *via recoil polarization.*

[26] E. Cisbani, M. Jones, M. Khandaker, N. Liyanage, L. Pentchev, C. Perdrisat, V. Punjabi, and B. Wojtsekhowski for the GEp(5) Collaboration, *(A New Proposal to Jefferson Lab 12 GEV - PAC32) - Large Acceptance Proton Form Factor Ratio Measurements at 13 and 15* $(GeV/c)^2$ *Using Recoil Polarization Method*, 2008.

[27] G. Cates, S. Riordan, and B. Wojtsekhowski for the E12-09-016 Collaboration, *Update for E12-09-016: Measurement of the neutron electromagnetic form factor ratio* G_E^n/G_M^n *at high* Q^2.

[28] W. Bertozzi for the Hall A collaboration, *Jefferson Lab PAC32 Proposal - Precision Measurement of the Proton Elastic Cross Section at High* Q^2, 2008.

[29] F. DE PERSIO, S. KIPRICH, F. MEDDI, and G. M. URCIUOLI, in *Proceedings, 14th ICATPP Conference on Astroparticle, Particle, Space Physics and Detectors for Physics Applications (ICATPP 2013): Como, Italy, September 23-27, 2013* (PUBLISHER, ADDRESS, 2014), pp. 457–462.

[30] V. Brio, V. Bellini, C. Petta, L. Re, C. M. Sutera, F. Tortorici, B. Wojtsekhowski, J. C. Cornejo, G. Franklin, and B. Quinn, Radiation Effects and Defects in Solids **173**, 857 (2018).

[31] T. Averett, B. Wojtsekhowski, A. Amidouch, S. Danagoulian, G. Niculescu, I. Niculescu, and Jefferson Lab SBS Collaboration Collaboration, in *APS Meeting Abstracts* (PUBLISHER, ADDRESS, 2017), p. E12.007.

[32] L. Re, V. Bellini, V. Brio, E. Cisbani, S. Colilli, F. Giuliani, A. Grimaldi, F. Librizzi, M. Lucentini, F. Mammoliti, P. Musico, F. Noto, R. Perrino, C. Petta, M. Russo, M. Salemi, F. Santavenere, G. Sava, D. Sciliberto, A. Spurio, M.C. Sutera, and F. Tortorici, Radiation Effects and Defects in Solids **173**, 818 (2018).

[33] Re Leonard, Master's thesis, University of Catania, 2015.

[34] Fabio Sauli, Nuclear Instruments and Methods in Physics Research Section A: Accelerators, Spectrometers, Detectors and Associated Equipment **805**, 2 (2016), special Issue in memory of Glenn F. Knoll.

[35] J. Benlloch, A. Bressan, M. Capeans, M. Gruwe, M. Hoch, J. C. Labbe, A. Placci, L. Ropelewski, and F. Sauli, Nucl. Instrum. Meth. **A419**, 410 (1998).

[36] Marco Poli Lener, Ph.D. thesis, University of Roma - "Tor Vergata", 2005.

[37] B Ketzer, Nuclear Instruments and Methods in Physics Research Section A: Accelerators, Spectrometers, Detectors and Associated Equipment **494**, 142 (2002), proceedings of the 8th International Conference on Instrumentatio n for Colliding Beam Physics.

[38] E. Cisbani and P. Musico, *APV-25 based readout electronics for the SBS front GEM Tracker, Version 1.0*, 2014.

[39] M. Friedl, C. Irmler, and M. Pernicka, Nuclear Instruments and Methods in Physics Research Section A: Accelerators, Spectrometers, Detectors and Associated Equipment **572**, 385 (2007), frontier Detectors for Frontier Physics.

[40] D Abbaneo, Masooma Abbas, Marcello Abbrescia, Ahmed Abdelalim, M Abi Akl, Waqar Ahmed, Palma Altieri, Reham Aly, C Armaingaud, C Asawatangtrakuldee, A Ashfaq, P Aspell, Yasser Assran, I Awan, S Bally, Yunqi Ban, Subhashish Banerjee, Patrizia Barria, Luigi Benussi, and A Zhang, Journal of Instrumentation **10**, C03039 (2015).

[41] Brücken, Erik and Hildén, Timo, EPJ Web Conf. **174**, 03004 (2018).

[42] CAEN-Tools for Discovery, N1471 Power Supply.

[43] Tektronix Company, *Model 6517B Electrometer - Reference Manual.*

[44] Melissa Alfonsi, Giovanni Bencivenni, Walter Bonivento, Alessandro Cardini, P de Simone, Fabrizio Murtas, Davide Pinci, Marco Poli Lener, Davide Raspino, and B Saitta, in *The triple-GEM detector for the M1R1 muon station at LHCb* (PUBLISHER, ADDRESS, 2005), pp. 811 – 815.

[45] Amptek, *Miniature X-Ray Source (Mini X2).*

[46] Lawrence Jones, *APV25-S1 User Guide Version 2.2*, 2.2 ed., RAL Microelectronics Design Group, 2001.

[47] Weather Underground, Newport News/Williamsburg International Airport, VA; https://www.wunderground.com/history/monthly/us/va/newport-news/KPHF/date/2019-9.

[48] Marco Russo, in *ICHIT (1)*, Vol. 7425 of *Lecture Notes in Computer Science*, edited by Geuk Lee, Daniel Howard, Jeong Jin Kang, and Dominik Slezak (Springer, ADDRESS, 2012), pp. 195–202.

[49] M. Russo, Swarm and Evolutionary Computation **27**, 145 (2016).

[50] M.Russo, G.Leotta, P.M.Pugliatti and G.Gigliucci, Solar Energy **105**, 264 (2014).

[51] Woon-Seng Choong, Physics in Medicine and Biology **54**, 6495 (2009).

[52] Stephen Derenzo, Woon-Seng Choong, and William W Moses, Physics in Medicine and Biology **59**, 3261 (2014).

[53] C. Bishop, *Neural Network for Pattern Recognition* (Clarendon Press - Oxford, ADDRESS, 1995).

[54] M.Russo, Genetic Fuzzy Learning, IEEE Transactions on Evolutionary Computation **4**, 259 (2000).